Modelling tidal flow for assessment of hydro-kinetic energy and bathing water quality in coastal waters

Sandeep Bomminayuni

THIS THESIS IS SUBMITTED IN PARTIAL FULFILMENT OF THE REQUIREMENTS FOR THE DEGREE OF
DOCTOR OF PHILOSOPHY (PhD)

Cardiff School of Engineering
Cardiff, Wales, UK

January 2015

Abstract

In this study, a hydro-environmental numerical model is utilised to further demonstrate the applicability of computer models to predict tidal flow in coastal waters. In particular, high resolution model simulations are performed at two selected sites: the Ogeechee Estuary, USA to assess the hydro-kinetic energy potential near Rose Dhu Island, a small island in the estuary; and at Swansea Bay, UK to assess faecal coliform pollution levels in the bay. Model results from the Ogeechee Estuary simulations revealed that better representation of branching smaller creeks located inshore enhanced the magnitude of tidal currents by approximately 30% near Rose Dhu Island. Evaluation of spatial and temporal distribution of currents revealed that local hot-spots of hydro-kinetic energy exist within the estuary and a maximum annual power of 4.75MW is available from the tidal streams surrounding the island. Investigation of the sensitivity of model parameters related to intertidal storage and bottom friction showed that ebb tide dominance in the estuary is reduced by lowering wetland elevation and by increasing bottom friction in the channel. Increasing the marsh friction to represent the resistance offered by marsh vegetation decreased the influence of intertidal storage on tidal distortion as ebb-dominance is reduced. Model results from the Swansea Bay simulations showed that three distinct flow patterns exist in the bay including re-circulating eddy like patterns, due to the presence of a headland located towards to the south-west end of the bay. The model-predicted distribution of Faecal Indicator Organisms (FIO) helped identify major pollution sources that negatively influence the rating of the Swansea Bay bathing water site. Investigation of the spatial distribution of FIO concentrations at the Designated Sampling Point (DSP) revealed that that the samples collected at DSP for compliance monitoring would correctly represent the pollution levels in the surrounding areas, however, at locations further off-shore significant spatial variability by up to five times was observed. As expected, intermittent peaks in FIO concentrations were noticeable following rainfall events, however, a strong temporal variability within a day was also observed at the DSP with concentration values varying by up to ten times in magnitude.

Acknowledgements

Firstly I would like to thank my supervisors, Professor Thorsten Stoesser and Professor Roger Falconer for the guidance and support they have provided me throughout my PhD. I believe I have immensely benefitted from their knowledge and experience which thoroughly inspired me to reach my full potential. I would also like to thank Dr. Reza Ahmadian for his guidance and help over the past two years.

Part of my research has been funded through “Smart Coasts= Sustainable Communities” project for which I thank Professor David Kay and his group from Aberystwyth University. I am extremely grateful to them for providing field data and necessary support without which this work wouldn’t have been possible.

I would like to thank my examiners Dr. Stephen Nash and Dr. Shunqi Pan for reviewing this work and providing valuable insights and comments which I believe has helped improve the quality of this thesis.

I would like to thank Dr. Kevin Haas and Brittany Bruder from Georgia Institute of Technology for their collaboration during my PhD. I have had a great time being part of the Rose Dhu project and thank you for your help.

I would like to thank members of the Hydro-environmental Research Centre, particularly my CFD group colleagues, who have made my stay at Cardiff University extremely enjoyable.

Finally, I would like to thank my parents and family members for their love and support without which I wouldn’t have accomplished my PhD. Particularly, I would like to thank my two elder brothers who have always guided me and inspired me to achieve my goals.

Table of Contents

Abstract iii

Acknowledgements iv

Table of Contents v

List of Figures viii

List of Tables xviii

Chapter 1 Introduction 1

1.1 Background 1

1.2 Introduction to tidal stream energy resource assessment 4

1.3 Introduction to bathing water quality assessment 7

1.4 Aims and Objectives of research 9

1.5 Outline of thesis 11

Chapter 2 Literature Review 12

2.1 Review of hydro-kinetic energy assessment studies 12

2.2 Review of bathing water quality assessment studies 18

2.3 Summary of studies reviewed with respect to the research objectives 24

Chapter 3 Model Description 26

3.1 Overview of the existing numerical models 26

3.2 Finite Volume Coastal Ocean Model 30

Chapter 4 Hydro-kinetic energy assessment for Rose Dhu Island, GA, USA 34

4.1 Introduction 34

4.2 Field Measurements 36

4.3 Numerical Model Setup 40

4.3.1 Computational Domain 40

4.3.2 Numerical Grid 43

4.3.3 Bathymetry 43

4.3.4 Boundary Conditions 44

4.3.5 FVCOM Model Parameters 46

4.4 Results and Discussion 47

4.4.1 Model Validation 49

4.4.2 Tidal Energy Assessment 58

4.5 Investigation of tidal asymmetry in the Ogeechee Estuary 64

4.5.1 Modifications to computational setup 65

4.5.2 Hydrodynamics: Model-predicted vs. measured comparisons 67

4.6 Summary 79

Chapter 5 Bathing water quality assessment for Swansea Bay, UK 81

5.1 Introduction 81

5.2 Field Measurements 84

5.2.1 Flow measurements 85

5.2.2 Faecal Indicator Organism Concentration Measurements 89

5.3 Numerical modelling details 90

5.3.1 Computational Domain 90

5.3.2 Numerical Grid 91

5.3.3 Bathymetry 93

5.3.4 Boundary conditions 94

5.3.5 FVCOM model parameters 95

5.4 Swansea Bay hydrodynamics 98

5.4.1 Hydrodynamics validation 101

5.4.2 Simulated vs. Measured drogue tracks 116

5.5 FIO Modelling ... 126

5.5.1 FIO distribution at Swansea Bay ... 126

5.5.2 FIO validation ... 130

5.5.3 Spatial-temporal variability of FIO ... 141

5.6 Summary ... 152

Chapter 6 Summary and Conclusions ... 155

6.1 Recommendations for future work ... 158

References ... 160

List of Figures

Figure 1.1: Pictures showing water surface during high tide (top panel) and low tide (bottom panel) in the Bay of Fundy on the Atlantic coast of North America. Source: http://www.bayoffundy.com/about/highest-tides/ 2

Figure 4.1: Map of Ogeechee Estuary. Orange highlighted area marks Rose Dhu Island. Yellow and pink highlighted areas mark, as referred to this study, west and east channels respectively. Red Star indicates location of GPS base station. Inset image: Map of Southeastern United States for geographic reference. 35

Figure 4.2: Depth-averaged velocity contours obtained from field measurements on two separate days in 2010; A, B and C are three transects along which measurements were carried out in 2011 39

Figure 4.3: Map of the Ogeechee Estuary obtained from the US National Oceanic and Atmospheric Administration coastline extractor (http://www.ngdc.noaa.gov/mgg/coast/) 41

Figure 4.4: Map of the wetlands obtained from the National Wetlands Inventory of the US Fish and Wildlife Services 42

Figure 4.5: Computational domain of the present study 42

Figure 4.6: Numerical grid employed in the present study. Numbers in yellow indicate the anti-clockwise numbering (1 to 33) used for the 33 grid nodes along the open boundary. 43

Figure 4.7: Contours of the bathymetry in the computational domain 44

Figure 4.8: Contours of the depth-averaged current magnitude in the entire Ogeechee Estuary for a flood tide 47

Figure 4.9: Contours of the depth-averaged current magnitude in the entire Ogeechee Estuary for an ebb tide 48

Figure 4.10: Zoomed in contours of the depth-averaged current magnitude (cm/s) close to the Rose Dhu Island for a flood tide, left from the model, right from measurements 49

Figure 4.11: Zoomed in contours of the depth-averaged current magnitude (cm/s) close to the Rose Dhu Island for an ebb tide, left from the model, right from measurements 49

Figure 4.12: Comparison of computed water levels represented by red line against field measurements from four different days represented by blue symbols 51

Figure 4.13: Locations of three points (1-3) selected for kinetic power density calculations and transects (A-C) from field measurements in 2011, the shaded region is Rose Dhu Island. Depth-averaged current magnitudes from the three transects for the model and measurements for different times. Positive and negative currents are flood and ebb tide, respectively 53

Figure 4.14: Time series of the volume flux for the three transects for the measurements (top), model (middle) and modified model (bottom). Positive and negative fluxes are for flood and ebb tide, respectively 55

Figure 4.15: The kinetic energy flux as a function of the volume flux for transect A. Positive and negative fluxes are for flood and ebb tide, respectively........................... 57

Figure 4.16: Histograms of depth averaged current velocity magnitudes and power density at points 1, 2, and 3 computed using harmonic analysis of the modified model data.. 60

Figure 4.17: Time series of (top) the predicted power for point 2 and (bottom) total kinetic power in Transect A 62

Figure 4.18: Modified computational domain. The area enclosed in black dotted lines shows the boundary extension made to better represent the smaller creeks upstream of the Little Ogeechee River.. 65

Figure 4.19: Comparisons between field measurements, Simulation A1, and Simulation B1, for water levels (top row) and volume fluxes (bottom row) for transect. Surface heights are all in MTL.. 68

Figure 4.20: Tidal stage diagram for simulation A1 at the transect. Dashed lines represent marsh elevation z_{mA1}. All surface heights in MTL. Positive Q represents flood volume fluxes while negative Q represents ebb. Period represented: Entire duration of model simulation November 16 -December 29, 2011 69

Figure 4.21: Hydrodynamic effects of change in marsh elevation: time series for Simulations A1 and B1. a) Relative surface heights in MTL, b) Relative surface height, or pressure gradient proxy, between the open ocean and transect surface heights and c) Transect volume flux for both simulations. Positive Q represents flood volume fluxes while negative Q represents ebb. Date represented: December 22, 2011. Timestamps, t_n, are reference points. 71

Figure 4.22: Hydrodynamic effects of change in marsh elevation: tidal stage diagrams for Simulations A1 and B1. Dashed lines represent marsh elevation for simulation. All surface heights in MTL. Positive Q represents flood volume fluxes while negative Q represents ebb. First tidal cycle of December 22, 2011 with labelled points corresponding to timestamps in Figure 4.21. 72

Figure 4.23: Hydrodynamic effects of change in overall friction: time series for Simulations A2, B3, and B2. Line colours are darker with increasing friction. a) Relative surface heights in MTL, b) Relative surface height, or pressure gradient proxy, between the open ocean and transect surface heights and c) Transect volume flux for both simulations. Positive Q represents flood volume fluxes while negative Q represents ebb. Date represented: December 22, 2011. Timestamps, t_n , are reference points. 75

Figure 4.24: Hydrodynamic effects of change in overall friction: tidal stage diagrams for Simulations A2, B3, and B2. Line colours are darker with increasing friction. Positive Q

represents flood volume fluxes while negative Q represents ebb. First tidal cycle of December 22, 2011 with labelled points corresponding to timestamps in Figure 4.23.. 76

Figure 4.25: Hydrodynamic effects of change in marsh friction: tidal stage diagrams for Simulations A2, A1, and A3. Line colours are darker with increasing marsh friction. Positive Q represents flood volume fluxes while negative Q represents ebb. First tidal cycle of December 22, 2011 with labelled points corresponding to timestamps in Figure 4.23............ 77

Figure 4.26: Binary map of differences in surface heights between simulations A2 and A3 at time t_2. Dark grey represents areas where water levels are higher for A2 and light grey represents areas where water levels are higher for A3............ 78

Figure 5.1: Satellite image of Swansea Bay showing prominent locations along the bay 82

Figure 5.2: Top panel - Release of a drogue as a part of field measurements, Bottom panel – ADP deployment in the field............ 85

Figure 5.3: Summary of the release locations and drogue movements observed in Swansea bay. Yellow and Green symbols correspond to drogues released at a vertical depth of 1m below the water surface, Pink and Orange symbols correspond to drogues released at a vertical depth of 2m below the water surface............ 86

Figure 5.4: Five locations where model data is compared against field data from ADP deployments............ 87

Figure 5.5: Top panel- time-series of water levels obtained from measurements, Bottom panel- contours of current profiles obtained from measurements. 88

Figure 5.6: Red and black dots show locations of major pollution sources in Swansea Bay. Sites 1 to 3 are the locations where field data of FIO concentrations is available for model validation. 89

Figure 5.7: Computational domain of the present study............ 90

Figure 5.8: Top panel- computational domain before modifications to coastline geometry at Swansea Bay, Bottom panel- computational domain after modifications to coastline geometry at Swansea Bay. 91

Figure 5.9: The numerical grid employed in this study. 92

Figure 5.10: a) Numerical grid with average grid spacing of 50m in Swansea Bay, and b) Numerical grid with average grid spacing of 25m in Swansea Bay. 93

Figure 5.11: The contours of mean water depth in the entire computational domain. ... 93

Figure 5.12: Example of water level time-series that is specified at the seaward boundary. 94

Figure 5.13: Contours and vectors of depth-averaged current speeds at approximately three hours after low tide for the entire computational domain. 98

Figure 5.14: Contours and vectors of depth-averaged current speeds at approximately three hours after high tide for the entire computational domain. 99

Figure 5.15: Contours and vectors of depth-averaged current speeds at approximately three hours after low tide at Swansea Bay. 100

Figure 5.16: Contours and vectors of depth-averaged current speeds at approximately three hours after high tide at Swansea Bay. 100

Figure 5.17: Comparison of simulated vs. measured water levels at Location 1. Time stamps t1, t2, t3, t4 refer to four selected points in time at which current comparisons in the vertical direction are performed. 101

Figure 5.18: Comparison of simulated vs. measured water levels at Location 2. 101

Figure 5.19: Comparison of simulated vs. measured water levels at Location 3. 102

Figure 5.20: Comparison of simulated vs. measured water levels at Location 4. 102

Figure 5.21: Comparison of simulated vs. measured water levels at Location 5. 103

Figure 5.22: Comparison of simulated vs. measured depth-averaged current speeds at Location 1. 104

Figure 5.23: Comparison of simulated vs. measured depth-averaged current speeds at Location 2. 105

Figure 5.24: Comparison of simulated vs. measured depth-averaged current speeds at Location 3. 105

Figure 5.25: Comparison of simulated vs. measured depth-averaged current speeds at Location 4. 106

Figure 5.26: Comparison of simulated vs. measured depth-averaged current speeds at Location 5. 106

Figure 5.27: Comparison of simulated vs. measured depth-averaged current directions at Location 1. 107

Figure 5.28: Comparison of simulated vs. measured depth-averaged current directions at Location 2. 108

Figure 5.29: Comparison of simulated vs. measured depth-averaged current directions at Location 3. 108

Figure 5.30: Comparison of simulated vs. measured depth-averaged current directions at Location 4. 109

Figure 5.31: Comparison of simulated vs. measured depth-averaged current directions at Location 5. 109

Figure 5.32: Simulated vs. measured profiles of current speeds at Location 1. 111

Figure 5.33: Simulated vs. measured profiles of current speeds at Location 2. 112

Figure 5.34: Simulated vs. measured profiles of current speeds at Location 3. 113

Figure 5.35: Simulated vs. measured profiles of current speeds at Location 4. 114

Figure 5.36: Simulated vs. measured profiles of current speeds at Location 5. 115

Figure 5.37: Observed (symbols) vs. simulated (lines) drogue movements at an offshore location corresponding to releases on 04/07/2011. 1m drogues are represented by red and blue symbols/lines, whereas 2m drogues are represented by black and green

symbols/lines. Time of drogue release is indicated by blue symbol in the tide curve plotted as inset. 117

Figure 5.38: Observed (symbols) vs. simulated (lines) drogue movements near the River Neath on 09/06/2011. 1m drogues are represented by red and blue symbols/lines, whereas 2m drogues are represented by black and green symbols/lines. Time of drogue release is indicated by blue symbol in the tide curve plotted as inset. 118

Figure 5.39: Observed (symbols) vs. simulated (lines) drogue movements near the River Tawe on 27/06/2011. 1m drogues are represented by red and blue symbols/lines, whereas 2m drogues are represented by black and green symbols/lines. Time of drogue release is indicated by blue symbol in the tide curve plotted as inset. 119

Figure 5.40: Observed (symbols) vs. simulated (lines) drogue movements near the River Tawe on 28/06/2011. 1m drogues are represented by red and blue symbols/lines, whereas 2m drogues are represented by black and green symbols/lines. Time of drogue release is indicated by blue symbol in the tide curve plotted as inset. 119

Figure 5.41: Observed (symbols) vs. simulated (lines) drogue movements near the River Tawe on 27/06/2011 for modified computational domain shown in red. 1m drogues are represented by red and blue symbols/lines, whereas 2m drogues are represented by black and green symbols/lines. Time of drogue release is indicated by blue symbol in the tide curve plotted as inset. 120

Figure 5.42: Observed (symbols) vs. simulated (lines) drogue movements at Mumbles Head on 29/06/2011. 1m drogues are represented by red and blue symbols/lines, whereas 2m drogues are represented by black and green symbols/lines. Time of drogue release is indicated by blue symbol in the tide curve plotted as inset. 121

Figure 5.43: a) Original computational domain, b) Hypothetical case with extremely smooth geometrical features at Mumbles Head, and c) Hypothetical case with slightly sharp geometrical features at Mumbles Head. 122

Figure 5.44: Observed (symbols) vs. simulated (lines) drogue movements at Mumbles Head on 29/06/2011 for a) Hypothetical case with extremely smooth geometrical features at Mumbles Head, and b) Hypothetical case with slightly sharp geometrical features at Mumbles Head. Time of drogue release is indicated by blue symbol in the tide curve plotted as inset. 123

Figure 5.45: Top panel- Mumbles Head as one land mass during low tide (http://www.panoramio.com/photo/731975), Bottom panel- Mumbles Head comprising of two disjointed land masses during the major portion of the tidal cycle (http://www.geograph.org.uk/photo/3213222). 124

Figure 5.46: Comparison of model-predicted flow patterns against simplified flow sketches from the work of Ferentinos and Collins (1979). 125

Figure 5.47: Contours of FIO concentrations in Swansea Bay at a time instant when water enters the bay during a flood tide. 127

Figure 5.48: Contours of FIO concentrations in Swansea Bay a time instant close to high water. 127

Figure 5.49: Contours of FIO concentrations in Swansea Bay at a time instant when the flood tide recedes and a transition to ebb tide begins. 128

Figure 5.50: Contours of FIO concentrations in Swansea Bay at a time instant when water drains from the bay during an ebb tide. 128

Figure 5.51: Contours of FIO concentrations in Swansea Bay at a time instant close to low water. 129

Figure 5.52: Simulated vs. measured comparisons of FIO concentration showing model sensitivity to T_{90} values at Site 1. 132

Figure 5.53: Simulated vs. measured comparisons of FIO concentration showing model sensitivity to T_{90} values at Site 2. 132

Figure 5.54: Simulated vs. measured comparisons of FIO concentration showing model sensitivity to T_{90} values at Site 3. 132
Figure 5.55: Simulated vs. measured comparisons of FIO concentration showing model sensitivity to T_{90} values at Site 1. 133
Figure 5.56: Simulated vs. measured comparisons of FIO concentration showing model sensitivity to T_{90} values at Site 2. 133
Figure 5.57: Simulated vs. measured comparisons of FIO concentration showing model sensitivity to T_{90} values at Site 3. 134
Figure 5.58: Simulated vs. measured FIO concentrations at Site 1. 135
Figure 5.59: Contours of FIO concentration at approximately half an hour after high water at Swansea Bay 136
Figure 5.60: Contours of FIO concentration at approximately one hour after low water at Swansea Bay.. 136
Figure 5.61: Simulated vs. measured FIO concentrations at Site 2. 138
Figure 5.62: Contours of FIO concentration at approximately two and half hours after high water at Swansea Bay.. 139
Figure 5.63: Simulated vs. measured FIO concentrations at Site 3. 140
Figure 5.64: Location of the five transects near DSP along which model data is extracted for investigation of spatial-temporal variability of FIO concentrations. 142
Figure 5.65: Red lines correspond to simulated FIO concentration values obtained from all points along Transect 3; Black dots correspond to measured temporal geometric mean of FIO concentrations at the DSP. 143
Figure 5.66: Time series of water levels, discharge values in River Clyne and Brynmill Stream at Swansea Bay for the simulation period. 144
Figure 5.67: Lighter lines correspond to simulated temporal geometric mean of FIO concentration values obtained from all points along Transect 3; Red line corresponds to

arithmetic average of all the lighter lines; Black dots correspond to measured temporal geometric mean of FIO concentrations at the DSP. 145

Figure 5.68: Simulated FIO concentration values at four locations on transect 3 corresponding to 19/07/11.. 146

Figure 5.69: Simulated FIO concentration values at four locations on transect 3 corresponding to 02/09/11.. 146

Figure 5.70: Simulated FIO concentrations at four locations (c1, c3, c5, c7) along all transects (T1 to T5) corresponding to 19/07/2011. 149

Figure 5.71: Simulated FIO concentrations at four locations (c1, c3, c5, c7) along all transects (T1 to T5) corresponding to 02/09/2011. 150

List of Tables

Table 2.1: Summary of tidal energy resource assessment studies................................ 15

Table 4.1: Amplitude (A, cm) and phase (ϕ, degrees) values of six tidal constituents specified as boundary conditions in the model... 45

Table 4.2: Ogeechee Estuary Model Parameters... 46

Table 4.3: Harmonic analysis results derived from 31 day record of water surface heights and depth averaged current velocities for each selected point. 59

Table 4.4: List of simulations and model parameters.. 66

Table 4.5: Root mean square error values between model-predicted and observed surface heights and volume fluxes for simulations A1 and B1 68

Table 5.1: Water level statistics from each location.. 87

Table 5.2: Depth-averaged current speed statistics from each location......................... 88

Table 5.3: Summary of discharges and FIO concentrations for all the input sources considered in this study for the time period between mid July and September 2011..... 95

Table 5.4: Swansea Bay Model Parameters... 96

Table 5.5: List of simulations conducted in this study 97

Table 5.6: Root Mean Square Error between model-predicted and measured water levels and depth-averaged currents at five locations in Swansea Bay.................................. 103

Table 5.7: Root Mean Square Error between model-predicted and measured current speed vertical profiles for four selected time instants at five locations in Swansea Bay. 116

Table 5.8: List of decay rate calibration runs and corresponding T_{90} values............... 131

Chapter 1

Introduction

1.1 Background

Tides are the rise and fall of ocean water levels caused by the gravitational forces of the Moon and Sun acting on the Earth, as well as the rotation of the Earth itself. The changes in water levels caused by the tides generate oscillating high velocity sea currents also known as tidal streams. Although these currents are of relatively small magnitude in deep offshore locations, near the shore the currents are significantly influenced by local topographical features such as headlands, inlets to bays and lagoons, leading to amplification of current magnitude and production of complex flow patterns. Moreover, the difference between high and low tides can be enormous at certain locations making it very challenging to study tidal flow in coastal waters. For example, as water level rises and falls in shallow estuarine systems with intertidal storage, flooding and draining of marshes/wetlands occurs periodically resulting in time-varying flow characteristics that are very difficult to predict. Similarly, flow features in tidal channels during the extreme ends of the tide (high water/low water) are very distinct and complex to understand. Figure 1.1 shows as an example the high and low tide in the Bay of Fundy, a bay on the Atlantic coast of North America which features the world's largest tidal range (~16m). The figure clearly shows the difference between low and high tides with channel cross-section geometry and bottom roughness significantly affecting the local flow conditions especially during the low tide.

Figure 1.1: Pictures showing water surface during high tide (top panel) and low tide (bottom panel) in the Bay of Fundy on the Atlantic coast of North America. Source: http://www.bayoffundy.com/about/highest-tides/

Tides have traditionally been monitored through gauges and tidal current stations located in coastal waters. However, the recent advancements in computing technology has seen a rapid increase in the usage of modelling tools towards understanding and predicting tides and their flow characteristics. The main advantage of using numerical models over field monitoring or measurements is that numerical simulations can provide an accurate prediction of water levels and currents at any location within the selected computational domain. This is particularly useful when tidal gauges or current monitoring stations are situated far away from the region of interest because flow conditions (especially currents) at one location are generally a poor indicator of conditions at another location. In addition, numerical simulations can provide flow information for long time-periods (days, months or years) at relatively low cost unlike boat-based measurements which are usually expensive and time consuming or measurements through equipment like buoys or current profilers which are often subjected to damage or loss.

Although there are many such advantages, modelling based studies have several limitations which make it very challenging to accurately simulate and predict tidal flow characteristics in coastal waters. For example, modelling studies often have to depend on relatively old data sources for bathymetry and coastline representation in the models due to lack of up-to-date information. Not only does it influence the overall model predictions but also result in inaccurate representation of site specific topographical features like marshes/wetlands, headlands, inlets etc., which play a major role in the flow hydrodynamics. In addition, models often have to undergo rigorous calibration of parameters, for instance bottom friction, to account for the variability in type and size of roughness elements present in the ocean bed. Due to such limitations and challenges involved, scientists and engineers complement numerical simulations with on-site field measurements.

Over the past few decades many modelling-based studies have been conducted towards understanding and predicting tidal flows. For example, numerical models have been used towards the study of flow and sediment transport processes in coastal waters because such knowledge is important to the shipping industry for the safe navigation of vessels in shallow ports and harbours. Similarly, numerical models have been utilised towards understanding tides, waves, and storm surges because communities are often exposed to coastal flooding and erosion which can cause huge damage to property and life. Furthermore, numerical models have been used to provide information on the possible changes to flow conditions or environmental impacts caused by future scenarios like construction of coastal engineering projects, rise of sea level due to climate change etc. In this context, the present study aims to further demonstrate the applicability of computer models to understand and predict tidal flow in coastal waters.

In particular, the focus of this study is towards assessment of tidal stream energy and bathing water quality in coastal waters using numerical model simulations. A brief introduction and scope for further research on tidal stream energy resource assessment and bathing water quality assessment are presented in the following sections.

1.2 Introduction to tidal stream energy resource assessment

Many locations in the world feature strong tidal currents: Pentland Firth in Scotland, Severn Estuary in the UK, the straits of Alaska in the USA, Bay of Fundy in Canada, the fjords of Norway, Italy and Philippines among others (Bryden and Melville, 2004; Charlier, 2003). Over the past few decades, several assessment studies have been conducted at these and other locations around the world towards identification of suitable sites for tidal stream energy extraction. A detailed review of some of these studies is provided in the Literature Review Chapter. Similar to wind power, the kinetic power in the tidal streams can be estimated by

$$P_{kinetic} = \frac{1}{2}\rho\, A\, V^3 \tag{1.1}$$

where ρ is the density of water (1025 kg/m^3), A is the area of cross-section of the flow and V is the current speed. With kinetic power being directly proportional to the cube of current speed, areas of high currents are often regarded as ideal locations for tidal power extraction. However, one of the major concerns for power extraction at a site is the negative impacts they can have on the surrounding environment and ecosystem. For example, presence of turbine devices can alter the flow hydrodynamics in the near and far-field and can possibly impact the intertidal ecology and habitat of endangered species. As such many previous studies have been conducted to investigate the upper limit for power extraction and it was observed that the maximum extractable power should be 15-30% of the total available power to avoid major impacts on the ecosystem that may be caused due to change in flow hydrodynamics (Bryden et al. 2004, EPRI 2006, Polagaye et al. 2008). This percentage limit of extraction, also referred to as the Significant Impact Factor (SIF), varies across different sites and does not include other economic, social and practical constraints which can also limit the amount of power extraction. Nevertheless, SIF can initially be applied to conduct a preliminary screening of potential sites prior to detailed site-specific assessment studies. Another approach commonly used in some of the previous modelling-based resource assessment studies to determine the impacts of power extraction, is to directly include turbine devices within the hydrodynamic model. For example, turbine devices can be modelled through retarding force terms in momentum equations or through high friction coefficients to mimic the process of energy extraction. As such these models can enable investigation of the impact of turbines on the flow hydrodynamics for different rates of power extraction and also provide an estimate of the maximum power that can be extracted without significantly altering the flow hydrodynamics.

Recently, the study of Neil et al. (2014) highlighted that while there are several physical, socio-economic and environmental constraints that are considered in selection of sites for tidal energy projects, an important factor that is not routinely considered despite its importance in quantifying the resource, is tidal asymmetry. Tidal asymmetry or distortion refers to the duration inequality in the rise and fall of tides, often resulting in flood or ebb dominant systems. It is usually observed in shallow inlets / estuarine systems where the change in topography, bottom friction, presence of wetlands etc. generate nonlinearities which result in tides being significantly different to the sinusoidal form observed in the deep ocean. This difference in tidal water levels between the estuary and ocean introduces additional pressure gradients which influence the magnitude and duration of tidal currents and thereby the amount of hydro-kinetic energy that is available within an estuary. With such direct implications to the available tidal stream energy it is important for resource assessment studies to accurately predict and understand the factors contributing towards tidal asymmetry.

Many previous studies (e.g. Speer and Aubrey 1985, Parker 1991) have identified bottom friction and intertidal storage as the two important causes of asymmetry in tidal channels. With majority of the modelling-based tidal resource assessment studies conducted so far being at open locations with little to no intertidal storage (such as straits, bays) perhaps little attention has been given towards investigating tidal asymmetry. This is possibly because bottom friction coefficient, a parameter often varied as part of model calibration/validation, can inherently ensure that tidal asymmetry is predicted well. However, for tidal resource assessment studies at locations with significant intertidal storage volumes such as in shallow interconnected tidal creeks with marshes/wetlands, tidal asymmetry needs to be investigated thoroughly as it is not straightforward to realistically and accurately represent the effect of marshes within numerical models. Previous studies that have modeled the effect of marshes have shown that different types of vegetation (e.g. emergent vegetation, fully submerged vegetation etc.) can exist on marshlands which offer various forms of resistance to flow of water and propagation of waves. With such direct implications to the flow hydrodynamics it is important that resource assessment studies, especially at sites that are located at sheltered places with significant intertidal storage, realistically represent the effect of marshes to accurately quantify the available energy resource. As observed in the study of Neil et al. (2014) a 30% asymmetry in velocity can translate into a 100% asymmetry in power density; therefore resource assessment studies can benefit from detailed investigation into tidal asymmetry as it can help provide an accurate quantification of the energy potential.

1.3 Introduction to bathing water quality assessment

UK's Environment Agency in 2012 has estimated that approximately 10% of designated bathing waters in England and Wales are likely to fail to comply with the EU's revised Bathing Water Directive (rBWD) standards. In accordance with the Directive, bathing waters which consistently fail to comply with the regulatory standards for faecal coliform levels are required to put up notices prohibiting their use in order to protect public health. Since this could have huge impact on the tourist economies of nearby towns and cities along with the loss of approximately 50% of UK's current 'Blue Flag' beach awards, efforts are currently underway in many places within UK towards controlling faecal coliform pollution levels at beaches and bathing water sites.

Several modelling-based studies have been conducted previously on the assessment and prediction of faecal coliform pollution levels in coastal waters. For example, numerical models have been utilised to simulate the transport of bacteria discharged into the sea by rivers, streams and drainage outlets to assess the general distribution of faecal coliforms in coastal waters and to develop strategies to enhance the accessibility/rating of bathing water sites. Similarly, numerical models have been used to study the transport of bacteria and other pollutants discharged offshore (through sewage treatment plant effluent outfalls) to understand and minimise their impacts on the faecal coliform levels at the coast. A review of such studies reveals that a variety of modelling approaches have been developed so far towards the assessment of faecal coliform pollution. The approaches depend mainly on the representation of pollution sources and the governing processes involved in the fate and transport of faecal coliforms. Pollution sources such as rivers / streams can either be represented as point sources in a coastal model or a more complex approach can be utilised wherein the entire catchment of the rivers / streams is modelled and dynamically linked to a coastal model for better representation of pollutants discharged from both point and non-point sources. While the governing processes involved in the transport of faecal coliforms such as advection and dispersion can be represented by the underlying hydrodynamic model, a more complex approach can include other processes such as the interaction of bacteria with sediments and dependency of bacteria decay rate on solar radiation intensity, background temperature, salinity etc.

Although the numerical models can provide such detailed assessment of faecal coliform pollution levels at bathing water sites, water samples collected as part of compliance monitoring programs are primarily used for measuring pollution levels and rating bathing water sites. This is because in-situ samples provide a true representation of the water quality at the site. However, previous studies based on intensive sampling and field surveys (detailed in Literature Review, Section 2.2) have indicated that sampling protocols of compliance monitoring programs are often inadequate because samples collected once per week could potentially be biased and lead to incorrect rating of bathing water sites. In particular, the studies have demonstrated that bacteria concentrations in water samples collected at bathing water sites exhibit strong within-day temporal and spatial variability that weekly samples fail to represent. As numerical models can provide information at required spatial and temporal scales and for long time periods, there is strong interest in modelling-based studies to guide sampling protocols of compliance monitoring programs. In particular, computer models can be applied for a thorough investigation of the spatial-temporal variability of bacteria concentrations at bathing water sites to identify good representative locations and ideal sampling times for accurate rating of bathing water sites.

1.4 Aims and Objectives of research

In view of the aforementioned scope for research in tidal stream energy resource assessment and bathing water quality assessment, the present study aims to: a) quantify the energy potential and investigate tidal asymmetry in an estuary with huge intertidal storage, and b) investigate the distribution and spatial-temporal variability of bacteria concentrations at a bathing water site to help guide sampling strategies of compliance monitoring programs. For this purpose, numerical model simulations are performed towards accurate prediction of tidal flow hydrodynamics at two selected sites: the Ogeechee Estuary, located on the south east coast of the United States; and Swansea Bay, located on the south Wales coast of the United Kingdom.

The model simulations for the first site, the Ogeechee Estuary, are primarily aimed at assessing the hydro-kinetic energy potential in the estuary and at identifying potential sites for tidal stream power extraction near Rose Dhu Island, a small island in the estuary. The Ogeechee estuarine system comprises of branching shallow network of tidal creeks with significant potential for energy extraction arising due to the local amplification of tidal amplitudes and currents at constricted channels. Previous studies have suggested that the extensive wetlands of the Ogeechee Estuary play a significant role in distorting tidal flow in the estuary. However, a detailed assessment of their influence, such as the role played by intertidal storage volume or friction associated with vegetation in the marshes, is not yet available to fully understand the factors contributing towards tidal asymmetry. Therefore this study aims to investigate tidal asymmetry in the estuary through several simulations by varying the model parameters associated with bottom friction and intertidal storage.

The model simulations for the second site, Swansea Bay, are primarily aimed at assessing bathing water quality in the bay affected by faecal coliform pollution and at helping the local communities sustain their touristic economy through prevention of beach closures due to non-compliance with regulatory standards. Swansea Bay is influenced by several pollution sources such as rivers, small streams, and surface water drains which empty directly into the bay. These sources are typically affected by sewage and industrial runoff from further up the catchment and contribute towards enhanced faecal coliform levels in the bay especially during periods of heavy rainfall. With many such sources of pollution contributing towards poor water quality, rating of Swansea Bay has been consistently poor with respect to the standards of rBWD and under huge risk of non-compliance. In this context, this study aims to investigate faecal coliform pollution in the bay through hydro-environmental numerical modelling as part of a major study which aims to develop a water quality prediction and communication system at Swansea Bay to advice the public of the bathing water quality in real-time. Simulations of fate and transport of Faecal Indicator Organisms (FIO) discharged into the bay by various pollution sources will be performed to assess the general distribution of faecal coliform levels in the bay and at the Swansea Bay bathing water site. Based on the model predictions quantification of the spatial-temporal variability of faecal coliform levels will be performed at the Designated Sampling Point (DSP) - a location where water samples are collected for compliance monitoring, to investigate the possible inadequacy of current sampling protocols and to help guide future sampling strategies at the Swansea Bay bathing water site.

In summary, the two main objectives and three sub-objectives of this study are:

1) Perform modelling of tidal flow in the Ogeechee Estuary, USA for the benefit of a small community on Rose Dhu Island which intends to extract hydro-kinetic energy from surrounding tidal streams. The sub-objectives of this study are:

- Characterise tidal flow in the estuary and identify hotspots of hydro-kinetic energy.

- Quantify the energy potential in the vicinity of Rose Dhu Island using validated model data.
- Investigate the influence of intertidal wetlands on tidal asymmetry in the estuary.

2) Perform 3D modelling of tidal flow and bacteria transport at Swansea Bay bathing water site for the protection of public health and maintenance of touristic economy. The sub-objectives of this study are:

- Characterise tidal flow at Swansea Bay and validate the model using field measurement data.
- Assess the impact of various pollution sources on the faecal coliform pollution levels at Swansea Bay.
- Investigate the spatial-temporal variability of FIO concentrations at Swansea Bay bathing water site.

1.5 Outline of thesis

This thesis is organised into six chapters. Firstly, the literature review with regards to tidal stream energy assessment and bathing water quality assessment is presented in Chapter 2. An overview of the existing numerical models and description of the Finite Volume Coastal Ocean Model (FVCOM) used in this study is presented in Chapter 3. Next, details of the computational modelling performed for an assessment of hydro-kinetic energy potential at Rose Dhu Island, GA, USA are presented in Chapter 4. Following this, details of a hydro-environmental modelling study performed towards an assessment of faecal coliform level pollution levels at Swansea Bay, UK are presented in Chapter 5. Finally, summary and conclusions of this research and recommendations for future work are presented in Chapter 6.

Chapter 2

Literature Review

In this chapter, literature review is presented in two parts with regards to hydro-kinetic energy assessment and bathing water quality assessment. Both parts include an extensive review of the research studies conducted so far and a discussion on the need for future studies in these two areas. Following this, a short summary of the studies reviewed with respect to the research objectives of this study is provided.

2.1 Review of hydro-kinetic energy assessment studies

In the UK, Energy Technology Support Unit (ETSU, 1993) was the first to identify suitable sites for tidal stream energy extraction. Their study took into account sites with mean spring peak tidal stream speeds greater than 2m/s and water depth greater than 20m. Based on this criterion, thirty three potential sites were identified with a total surface area of 1450 Km^2. Following this study, European Commission (1996) produced a database of tidal stream energy resources around Europe and identified forty two sites in the UK based on a criterion that peak stream speed is greater than 1.5m/s. Although both these studies presented estimates of the available power, a detailed distribution of the energy resources could not be provided because they relied on tidal stream current values taken from navigational charts, which are only applicable to discrete locations. An alternative approach based on tidal flow modelling data from Proudman Oceanographic Laboratory (POL) was utilised by Associate British Ports marine environmental research (ABPmer) to produce an atlas of energy resources for the Department of Trade and Industry (DTI, 2004). Since the numerical grid of the model used by POL had a resolution of approximately 1.8 km in the horizontal, only a coarse-scale distribution of tidal stream energy density was provided for the continental shelf. In addition to these studies, many site-specific assessments within the UK have been conducted in the recent past. For example, Blunden and Bahaj (2006) performed an assessment of energy resources at Portland Bill, Dorset, UK using TELEMAC, a 2D finite element numerical model. The simulations were performed at a grid resolution of approximately 50m and the results were validated using water levels data from tidal gauge stations and tidal currents from admiralty charts. Their model succeeded in providing estimates of kinetic power that can be extracted from a turbine located off the Portland Bill headland. Similarly, Xia et al. (2010) provided an estimate of tidal stream energy resources in the Severn Estuary, UK using the Two-dimensional Layer Integrated Velocities and Solute Transport (DIVAST) model which was validated using a combination of data from admiralty charts and on-site measurements. Their study provided kinetic power density distribution within the estuary and an estimate of the energy that could be extracted at two potential locations. Very recently, Draper et al. (2014) provided an estimate of the maximum power that can be extracted at Pentland Firth, Scotland, UK using Advanced Circulation (ADCIRC), a 2D depth-averaged numerical model which was validated using on-site field measurements. In their study, tidal stream power extraction was modelled through a depth-averaged bed roughness parameter under the assumption that tidal devices induce a force proportional the square of the depth-averaged velocity. The available energy potential in the Pentland Firth was reported for several cases along with the impact of power extraction on the hydrodynamics in the nearby channels.

In the United States, Electric Power Research Institute (EPRI) was the first to evaluate tidal energy resources in five states and two provinces of the US (EPRI, 2006). Suitable sites for energy extraction were identified based on the criterion that peak flood or ebb currents should have an averaged value of at least 1.5m/s. Recently, mapping of the tidal stream energy resources for the entire United States was performed by GTRI (2011). The study utilised 2D Regional Ocean Circulation Model (ROMS) to simulate tidal flow towards an evaluation of the tidal stream energy potential. The findings from their study were presented on a Geographical Information System (GIS) database which can be accessed on-line to visualise quantities like currents, water levels, available power density etc. along the entire US coast (Defne et al. 2011a). Defne et al. (2011b) conducted a resource assessment study for the coastal state of Georgia, USA using the 2D ROMS model. In their study, tidal stream power extraction was modelled through the inclusion of a retarding force in the governing momentum equations. The impact of power extraction from the Canoochee River, Georgia, USA on the water levels, currents and power densities in the nearby locations was reported in their study.

In addition to the sites in the UK and USA, several other locations have been evaluated for tidal stream energy potential throughout the world. Sutherland et al. (2007) utilised Tide2D numerical model to perform an assessment of tidal stream energy resources for Johnstone Strait, Vancouver, Canada. Grabbe et al. (2009) provided a theoretical resource assessment of tidal stream energy resources in Norway. Carballo et al. (2009) performed an assessment of the energy potential at the Ria de Muros coastal embayment in the Northwest of Spain using the Delft3D model.

A common feature of the above studies is that the assessment of tidal energy resources was conducted mainly at locations known to feature high tidal current magnitudes and with huge potential for tidal stream energy extraction. Table 2.1 presents a summary of the reviewed studies with current speeds at their study locations. The possible reason for focus of many studies being at such locations is that only sites with high potential could provide energy at a commercial, economically viable scale. Moreover, the turbines currently in use for energy extraction from tidal streams are predominantly horizontal-axis turbines (similar to wind energy) which have minimum current speed and water depth requirements for optimum operation. However, the advancements in turbine technology research, particularly, the development of vertical-axis turbines has opened up the possibility of exploiting tidal stream energy resources even at locations featuring current speeds as low as 1m/s. Although the available energy would be considerably lower at these locations, there is scope for nearby communities to extract renewable energy on a smaller scale.

Table 2.1: Summary of tidal energy resource assessment studies

Reference	**Location**	**Current Speed**
ETSU (1993)	UK	>2m/s
EC (1996)	Europe	>1.5m/s
DTI (2004)	UK	>2m/s
Blunden and Bahaj (2006)	Portland Bill, Dorset, UK	up to 3.6m/s
Xia et al. (2010)	Severn Estuary, UK	>2m/s
Draper et al. (2014)	Pentland Firth, UK	>5m/s
EPRI (2006)	US	>1.5m/s
GTRI (2011)	US	>2m/s
Defne et al. (2011b)	Georgia, US	up to 2m/s
Sutherland et al. (2007)	Vancouver, Canada	4-8m/s
Grabbe et al. (2009)	Norway	>4m/s
Carballo et al. (2009)	Spain	>2m/s

In summary, several resource assessment studies have been conducted previously at various locations around the world. The site investigations were initially based on observed data from current monitoring stations. Subsequently, numerical models have been utilised for resource assessment because of their ability to predict water levels and currents to a much finer detail spatially and temporally. However, the accuracy of power potential estimates provided by numerical models can be dependent on the parameters used in the model such as the bed friction coefficient. For example, Draper et al. (2014) conducted sensitivity tests on the bed friction coefficient used in their model and reported that power estimates varied by a factor of 0.78 and 1.1 when the friction coefficient was doubled and halved respectively. Such variability in power estimates can be significantly higher at sites featuring tidal asymmetry. Neil et al. (2014) in their investigation of role played by tidal asymmetry in the quantification of energy potential at Orkney Islands, UK, reported that a 30% asymmetry in velocity can translate into a 100% asymmetry in power density. With such direct implications to the available tidal stream energy it is important for resource assessment studies to accurately predict and understand the factors contributing towards tidal asymmetry.

Tidal asymmetry or distortion refers to the duration inequality in the rise and fall of tides, often resulting in flood or ebb dominant systems. In shallow estuaries, tidal asymmetry is primarily caused due to bottom friction and intertidal storage (Speer and Aubrey, 1985; Friedrichs and Aubrey, 1998; Parker 1991). Significant bottom friction is classically identified as a mechanism to induce flood dominated tides (Speer and Aubrey, 1985). With more momentum loss per unit volume at lower water levels, its effect is stronger at low tide. As a result, wave propagation slows, inducing a steepening of the wave form between the estuary and ocean, increasing of the floodward pressure gradient and resultant currents (Dronkers, 1986). Intertidal storage refers to the variable width of channel cross-sectional area with surface height, most notably with intertidal marshes or wetlands. When surface heights rise and inundate the banks of flat, expansive marshes, the surface area of the channels increase dramatically. By continuity, the rate of surface level rise decreases, increasing the floodward pressure gradient between the estuary and ocean, leading to a surge in flood currents. During ebb tide, the rate of water level decrease above the marsh banks is reduced as well, enhancing the ebb gradient and currents too. Thus, both ebb and flood currents are enhanced. The distortion is the change in the transitional periods between peak flood and ebb tides. Depending on whether the marsh elevation is lower or higher than the mean tidal level (MTL), peak flood and ebb tides either occur closer to low water and the flood to ebb transition is longer, or occur closer to high water and the ebb to flood transition is longer (Blanton et al., 2002; Dronkers, 1986). If friction and advection is also considered, it is also thought that wave propagation is slowed in the marshes due to the shallow depths and increased role of friction (Speer and Aubrey, 1985). As a result water level decreases at a slower rate in the wetlands than the channel, inducing an additional pressure gradient and inclination to drain the marshes, leading to ebb-dominant systems (Boon and Byrne, 1981; Dronkers, 1986).

Modelling the effect of intertidal wetlands/marshes on flow hydrodynamics has been performed by many researchers previously. Marshes have been typically represented in numerical models using high bottom friction coefficients in several studies (e.g. Loder et al. 2009; Zhang et al. 2012) to mimic the effect of drag associated with marsh vegetation. Some studies have utilised spatially varying bottom friction coefficients with regards to variable resistance offered by different types of vegetation (Wamsley et al. 2010). However, representing vegetation resistance through friction coefficient ignores the nonlinearities associated with the mechanics of flow through vegetation (Lapetina and Sheng, 2014). This is primarily because resistance offered by vegetation and consequently the vertical velocity structure varies with respect to the ratio of water depth to the vegetation height (Nepf and Vivoni, 2000). Therefore advanced models which account for vegetation resistance through skin friction drag terms in the governing momentum equations have been developed and utilised in some studies (e.g. Sheng et al. 2012; Lapetina and Sheng, 2014) to dynamically represent the effects of marsh vegetation. However focus of those studies has been primarily on determining the wave reduction and costal inundation protection offered by marsh vegetation during storm surges rather on investigating the impacts on tidal asymmetry. To the extent of studies reviewed by the author, so far only the 3D FVCOM modelling study of Huang et al. (2008) on tidal asymmetry in Okatee Creek, SC, USA has included the resistance offered by marsh vegetation through an enhanced friction coefficient in the marshes (10 times the friction in main channel). However the sensitivity of the model and distortion in the estuary to the marsh friction coefficient has not been performed in their study. In this regard, further research is required to fully investigate the sensitivity of marsh friction parameters in modelling tidal asymmetry, especially in shallow estuaries with extensive intertidal storage. Such studies can assist modelling-based tidal energy resource assessment studies as understanding the variability of tidal asymmetry to model parameters can provide insights into the variability of available power.

2.2 Review of bathing water quality assessment studies

Coastal waters around the world serve as a sink to many pollution sources such as: streams and rivers which bring in domestic and industrial waste, combined sewer overflows, effluent outfalls etc. With coastal waters being used for recreational purposes, compliance monitoring systems have been in place in many parts of the world for public health safety because studies have shown that faecal contamination in marine recreational waters leads to an increased risk of gastrointestinal illness (e.g. Kay et al. 1994, Wade et al. 2003). Moreover increased public usage and growing awareness on environmental impacts of pollutants has resulted in stricter regulations being imposed on the quality of water at beaches and bathing water sites. For example, the EU's rBWD mandates that bathing water sites which regularly fail to comply with the water quality standards are required to display notices prohibiting their use. Since this could have disastrous consequences to the local touristic economy, it is very important to accurately monitor and improve water quality at bathing water sites.

Compliance systems currently in place for water quality monitoring and rating of beaches and bathing water sites usually involve collection of water samples at designated times and locations. However, many studies have indicated that there is a huge spatial and temporal variability of pollutant concentration levels that the monitoring systems fail to capture reasonably. For example, the study of Kwasi et al. (1999) showed that faecal coliform concentrations at three designated bathing waters in Morecambe, UK varied temporally between samples collected during the morning and afternoon. In particular, they observed that the average faecal coliforms in the afternoon samples were 77%, 87% lower than those in the morning samples for the 1996, 1997 bathing seasons respectively due to the variations in water temperature and levels of ultra violet radiation. Moreover their study highlighted the limitations in the EU's bathing water Directive by providing evidence that the temporal variability can result in the incorrect rating of bathing waters as being either safe or unsafe. The study of Boehm (2007) also revealed the extreme temporal variability of faecal indicator bacteria concentrations in water samples collected at Huntington Beach, California. In particular, his study revealed that change in concentrations between consecutive samples (collected 1 or 10 min apart) is often greater than the single-sample microbiological standard and that the variability could even be as high as 700%. The work of Whitman and Nevers (2004), and their subsequent critical review (Nevers and Whitman, 2010) of policies and practices of beach monitoring in Great Lakes, USA has further identified factors that influence the rating of bathing waters. These factors include: depth, time, location, and frequency of sample collection, number of replicates collected and calculation of result.

The recent study of Amorim et al. (2014) consisting of intensive hourly and spatial sampling at an urban bathing area in Portugal also demonstrated the spatial and temporal variability of water quality. In particular, their study highlighted that flow hydrodynamics in the adjacent areas and sample retrieving time influenced the overall water quality and such factors should be taken into account while designing sampling protocols or bathing water profiles as required in the EU's rBWD.

Although many such studies indicate the inadequacy of compliance monitoring programmes, further supporting evidence can help assist in adopting policy changes because the observations made in these studies are usually based on limited sampling data. In particular, the collected data in these studies are either limited spatially, with only few sampling locations, or temporally, with only few hours of measurement data. In this regard water quality modelling studies can be of immense use as they can provide information at required temporal and spatial scales and for longer time periods. Moreover numerical models can adequately be supported by the field data and a comprehensive analysis of the spatial and temporal variability of faecal indicator organisms can be performed to guide bathing water sampling criteria. Although not directly related to bathing water quality, the work of Harnett et al. (2012) on eutrophication assessment in coastal waters provided an understanding of how an integrated approach involving water quality modelling and field measurements can assist monitoring programmes. In particular, their study highlighted the benefits of including modelling studies such as: a) models can provide spatial and temporal data of water quality variables and can enable the calculation of more representative averaged values instead of single-sample measurements; b) models can be used for optimisation of monitoring programmes as they enable the identification of discrete locations where collected water quality samples are more representative of the surrounding areas. Many previous modelling studies have assisted in the monitoring of FIO concentration distributions spatially and temporally in bathing waters. However, the major focus of their studies has been on the accurate understanding of the FIO transport processes at the bathing water sites rather than addressing the limitations of compliance monitoring programmes. Moreover, some of the modelling studies were aimed to investigate the effectiveness of future capital investment works in improving water quality at the bathing water sites. A review of some of these studies is presented in the following paragraphs.

Falconer and Lin (1997) provided details of a three-dimensional modelling study performed towards the evaluation of water quality in Humber Estuary, UK. In their study, simulations were conducted using TRIVAST, a 3D finite-difference numerical model, with a grid spacing of 500m in the horizontal and 8 layers in the vertical. The inputs to the model included daily discharges from 13 chemical and industrial works along the estuary, as well as domestic effluent discharges from several large towns located nearby. Their model was successfully used to predict the concentration distributions of salinity, faecal coliforms etc. in the estuary. In addition, the model was utilised to assess the environmental impact of constructing a new sewage treatment works at a nearby city. Kashefipour et al. (2002) performed a comprehensive hydro-environmental modelling study of Ribble Estuary, UK to quantify the impacts of various bacterial inputs into the estuary and the surrounding coastal waters on the bathing water quality. The numerical modelling was performed using a combined two-dimensional coastal model (DIVAST) and a cross-sectionally integrated one-dimensional river model (FASTER). The inputs to the model included direct discharges from wastewater treatment plants, several river inputs, and combined sewer overflows (CSO). After successful calibration of the model, several simulations were performed to evaluate the impact of CSO inputs and improved wastewater treatment systems on the bathing water quality. Kashefipour et al. (2006) performed modelling of the fate of faecal indicator organisms in Irvine Bay, UK in order to assess the main pollutant sources that cause the surrounding beaches to fail to comply with the European Community Bathing Water Directive. The numerical simulations were conducted using a 2D model, i.e., DIVAST at a uniform horizontal grid resolution of 300m, and results were validated using field measurements. Analysis of the results revealed the importance of variable bacteria decay rate on the prediction of concentration distributions in the bay. In addition, the model results revealed that three inputs (river Irvine, sewage, industrial effluents) among several others had a significant impact on the Irvine Bay bathing water quality.

Harris et al. (2004) presented results from three example numerical modelling studies (including a study at Swansea Bay) in their general overview of hydro-environmental issues and the related challenges faced by scientists and engineers. The focus of their study related to Swansea Bay was towards the evaluation of water quality in the bay following the releases from a waste water treatment plant (at Mumbles Head) subjected to different levels of treatment. The simulations in their study were conducted using a 3D finite difference based model at a grid resolution of 250m. Their model was successful in predicting the tidal currents, faecal coliform levels in the bay and associated risk of gastro-enteritis. Bedri et al. (2011) studied the impact of Escherichia coli (E. coli) emissions from a sewage treatment plant on the bathing water quality of Dublin Bay, Ireland through 2D and 3D numerical models. Their study revealed that the 3D model has provided an adequate representation of the hydrodynamic processes and distribution of E. coli concentrations in comparison to the 2D model particularly because of the presence of flow stratification and wind. Bougeard et al. (2011) studied the impact of E. coli loads from a watershed on the quality of water in the estuary of Daoulas area, France using a coupled catchment-coastal (2D) hydrodynamic model. Their work revealed that rainfall and agricultural practices in the catchment could result in rapid and large fluxes of E. coli (approximately 3 orders of magnitude in less than 24 hours) being discharged into the estuary. Moreover, it was observed that the time taken for estuary to recover to its original water quality is approximately 1 to 2 days depending on the duration of rainfall. Ge et al. (2012) investigated the reason behind consistently high bacterial contamination in an embayed beach in Chicago, USA through 2D numerical model simulations. Their study revealed that flow recirculation patterns in the embayment caused frequent deposition of E. coli and therefore a potential source of contamination during re-suspension of sediments.

In summary, several numerical modelling studies have been undertaken over the past few years towards the evaluation of water quality in coastal waters. These studies have provided a good understanding of the impacts of existing pollution sources and future water treatment works on the bathing water quality in marine recreational waters. However, with stricter water quality regulations being currently imposed at the bathing water sites, it is absolutely necessary to improve the accuracy of modelling studies for a better investigation of factors influencing bathing water quality. For instance, model-predicted hydrodynamics can be further improved through the application of 3D numerical models at a finer spatial grid resolution and calibration through detailed on-site field measurements. Moreover, modelling studies in conjunction with field measurements could be performed to address some of the inadequacies of compliance monitoring programmes. In particular, the vast amounts of data provided by numerical models could be utilised to guide sampling policies employed at bathing water sites because studies have shown that faecal bacteria concentrations often exhibit strong spatial-temporal variability.

2.3 Summary of studies reviewed with respect to the research objectives

Review of the hydro-kinetic energy assessment studies presented in Section 2.1 revealed that several studies have been conducted previously on quantifying energy potential from tidal streams around the world. The majority of these studies were conducted at locations with high current speeds (>2m/s) possibly because only sites with high power potential could provide energy at a commercial, economically viable scale. However, the advancements in turbine technology research, particularly, the development of vertical-axis turbines has opened up the possibility of exploiting tidal stream energy resources even at locations featuring current speeds as low as 1m/s. Although the available energy would be considerably lower at these locations, there is scope for nearby communities to extract renewable energy on a smaller scale. However, resource assessment at such locations, for example, in shallow estuaries with extensive intertidal storage, would require detailed investigation of tidal asymmetry as it plays a significant role in the quantification of energy potential. In particular, the influence of marsh vegetation in distorting tidal flow and the sensitivity of numerical model to parameters related to the intertidal storage needs to be studied thoroughly. In this regard, the present study models tidal flow in the Ogeechee Estuary, a shallow estuary characterised by tidal asymmetry due to the presence of extensive intertidal wetlands, to perform an assessment of energy potential and to understand the sensitivity of model parameters, particularly pertaining to intertidal storage, on tidal distortion.

Review of the bathing water quality assessment studies presented in Section 2.2 revealed that several studies have been conducted previously on assessing faecal coliform pollution in coastal waters. The focus of some of these studies has been on the accurate understanding of the FIO transport processes at the bathing water sites and to investigate the effectiveness of future wastewater treatment works in reducing pollution levels at the bathing water sites. Several other studies based on intensive sampling and field surveys have indicated that sampling protocols of compliance monitoring programs are often inadequate because samples collected once per week could potentially be biased and lead to incorrect rating of bathing water sites. In particular, the studies have demonstrated that bacteria concentrations in water samples collected at bathing water sites exhibit strong within-day temporal and spatial variability that weekly samples fail to represent. However, further supporting evidence is required for adopting policy changes because the observations made in these studies are usually based on limited sampling data. In particular, the collected data in these studies are either limited spatially, with only few sampling locations, or temporally, with only few hours of measurement data. As numerical models can provide information at required spatial and temporal scales and for long time periods, there is strong interest in modelling-based studies to guide sampling protocols of compliance monitoring programs. In this regard, the present study models tidal flow and faecal coliform transport at Swansea Bay bathing water site, currently at risk of non-compliance with rBWD, to assess the general distribution of faecal coliform levels in the bay and to thoroughly investigate the spatial-temporal variability of bacteria concentrations at the DSP to identify good representative locations and ideal sampling times for accurate rating of the bathing water site.

Chapter 3

Model Description

In this chapter, a description of the FVCOM model used in this study towards the modelling of tidal flow in the Ogeechee Estuary and Swansea Bay is presented. Firstly, an overview of some of the existing numerical models in the literature is given. Then, details of the governing equations, solution technique, and other capabilities of FVCOM are described.

3.1 Overview of the existing numerical models

There are several numerical models currently being used towards the simulation of coastal ocean processes. Some of these models include the Princeton Ocean Model (POM), the Estuarine and Coastal Ocean Model, Semi-Implicit version (ECOM-si) model, the ROMS model, the Three-dimensional Layer Integrated Velocities and Solute Transport (TRIVAST) model, the ADCIRC model, the Environmental Fluid Dynamics Code (EFDC) model and the TELEMAC model. A short description on each of these models is presented below.

POM was originally developed by Alan Blumberg and George Mellor (Blumberg and Mellor, 1987). The model solves the three-dimensional governing equations of fluid flow under the hydrostatic and Boussinesq assumptions using a second-order centred spatial finite differencing scheme. Leapfrog time differencing scheme is used in the model and an explicit treatment of the surface waves is also performed through a smaller time step than that used in the internal mode. The model equations are discretised on a staggered Arakawa "C" grid and a bottom following σ co-ordinate system is used for the vertical direction. The Mellor-Yamada Level 2.5

turbulence scheme is used in the model to calculate vertical mixing and horizontal mixing is parameterized using a Laplacian formulation with mixing coefficients proportional to the local grid spacing and velocity shears. Being one of the earliest coastal models to be developed this model has formed the basis for several numerical models over the years. For example, ECOM-si model developed in 1994 is a modified version of Princeton Ocean Model (Blumberg, 1994). The main differences from POM are (a) the use of a two-time-level temporal scheme rather than leapfrog, (b) the use of implicit rather than an explicit scheme for the free surface, and (c) the addition of wetting/drying capability. Although the inclusion of wetting/drying capability allows the simulation of tide and tide-induced currents, the use of structured grids in the model limits its ability to accurately represent tidal creeks, barriers and islands.

ROMS is a free-surface, primitive equations ocean model developed by researchers from Rutgers University, USA (Haidvogel et al. 2000a). The model is similar to POM in several respects, for example, use of a structured finite-difference grid in space, split-explicit time-stepping, second-order numerical approximations. However ROMS differs from POM with the inclusion of quasi-monotone advection schemes, and higher order constancy preserving time-stepping (Haidvogel et al. 2000b). Furthermore, ROMS has been designed to include explicit two-dimensional partitioning (blocking) into sub-domains that can be solved simultaneously on different processors of a computer thereby speeding up the calculation. ROMS model has nested gridding capabilities thereby allow for better resolution of tidal creeks, barriers and islands unlike the ECOM-si model.

TRIVAST is a 3D layer integrated model originally developed by Falconer et al. (1991) and refined by Lin and Falconer (1997). The governing mass and momentum conservation equations in the model are represented in an alternating direction implicit form using the finite difference technique and solved using the method of Gauss elimination and back substitution on curvilinear grids. TRIVAST model is capable of several water quality indicators and has been used in several environmental impact assessment studies.

ADCIRC is a 3D numerical model developed by researchers from University of North Carolina, USA and University of Notre Dame, USA (Luettich et al. 1992). The model was developed for the specific purpose of conducting long numerical simulations (on the order of a year) for very large computational domains (for example the entire east coast of the USA). The governing equations of the model are the same as other models; however, they are solved using a finite element method on unstructured triangular grids. The ADCIRC model includes a wetting and drying scheme to simulate tidal flow over low-lying areas and can also be used to simulate the influence of waves.

EFDC model (Hamrick, 1992) solves the three-dimensional Navier-Stokes equations on curvilinear grids with sigma coordinate transformation in the vertical direction. The momentum equations are solved using a second-order finite difference scheme and Mellor-Yamada level 2.5 turbulence closure schemes are used for the turbulence parameter transport equations. EFDC allows for wetting and drying of shallow areas using a mass conservation scheme. The model has been successfully used in several hydrodynamic and water quality studies worldwide.

TELEMAC-3D model developed by National Laboratory of Hydraulics and Environment of Electricité de France solves the Navier-Stokes equations using the finite element technique. The model uses unstructured triangular grids in the horizontal and sigma transformation for vertical discretisation. The model can be run in parallel form using the MPI or OpenMP implementations. This model has successfully been utilised in several coastal hydrodynamic and morphological studies.

A brief description of numerical models presented above has shown the general characteristics of models currently in use towards the simulation of coastal ocean processes. However, in order to accomplish the specific objectives of this study two key features have been identified as being important for the selection of the model. These include:

1) Unstructured Grids: For the purpose of tidal energy resource assessment and faecal coliform transport modelling, high grid resolution is required to accurately represent areas of interest such as locations of turbines or locations of pollution sources; however, fairly low resolution may be sufficient at regions elsewhere such as in deeper waters. Therefore the selected model should provide flexibility in meshing to allow for enhanced grid resolution at locations of interest. Unstructured grid (e.g. triangular cells) models provide such flexibility and are generally better suited than structured grid models because the degree of enhancement of grid resolution can be controlled / optimised unlike the structured grid models. In addition, unstructured grids allow for better geometric fitting in comparison to structured grids especially in areas with complex coastline geometries.

2) Multi-processing capabilities: The study areas involved in this research have fairly large computational extents (e.g. Bristol Channel & Severn Estuary computational domain has an extent of ~6000 km^2) and therefore model calculations would require high computational power to provide results in reasonable time scales. Models with multi-processing capabilities would be very suitable as they allow for simulations to be performed on high performance computing clusters.

Amongst the coastal ocean models discussed in this section ADCIRC and TELEMAC-3D models possess the above identified key features required for the accomplishment of this research. However, for carrying out faecal coliform modelling in this study both these models are not very suitable. This is because ADCIRC model does not have a built-in water quality module and whereas TELEMAC-3D model utilises an external water quality module (e.g. DELWAQ) that is not freely available.

Therefore for the purpose of this research the FVCOM model is selected, a detailed description of which is provided in the following section.

3.2 Finite Volume Coastal Ocean Model

FVCOM, originally developed by Chen et al. (2003), is based on the solution of governing fluid flow equations, namely, the mass and momentum conservation equations:

$$\frac{\partial u}{\partial x} + \frac{\partial v}{\partial y} + \frac{\partial w}{\partial z} = 0 \tag{3.1}$$

$$\frac{\partial u}{\partial t} + u\frac{\partial u}{\partial x} + v\frac{\partial u}{\partial y} + w\frac{\partial u}{\partial z} - fv = -\frac{1}{\rho}\frac{\partial P}{\partial x} + \frac{\partial}{\partial z}\left(K_m \frac{\partial u}{\partial z}\right) + F_u \tag{3.2}$$

$$\frac{\partial v}{\partial t} + u\frac{\partial v}{\partial x} + v\frac{\partial v}{\partial y} + w\frac{\partial v}{\partial z} - fu = -\frac{1}{\rho}\frac{\partial P}{\partial y} + \frac{\partial}{\partial z}\left(K_m \frac{\partial v}{\partial z}\right) + F_v \tag{3.3}$$

$$\frac{\partial P}{\partial z} = -\rho g \tag{3.4}$$

where x, y, and z are the east, north, and vertical axes in the Cartesian coordinate system; u, v, and w are the x, y, z velocity components; ρ is the density; P is the pressure; f is the Coriolis parameter; g is the acceleration due to gravity; K_m is the vertical eddy viscosity coefficient calculated using the Mellor and Yamada level 2.5 turbulence closure model (Mellor and Yamada, 1982); F_u, F_v are the horizontal momentum diffusion terms in x, y directions respectively defined as:

$$F_u = \frac{1}{D}\frac{\partial}{\partial x}\left[2A_m H \frac{\partial u}{\partial x}\right] + \frac{1}{D}\frac{\partial}{\partial y}\left[A_m H\left(\frac{\partial u}{\partial y} + \frac{\partial v}{\partial x}\right)\right] \tag{3.5}$$

$$F_v = \frac{1}{D}\frac{\partial}{\partial y}\left[2A_m H \frac{\partial v}{\partial y}\right] + \frac{1}{D}\frac{\partial}{\partial x}\left[A_m H\left(\frac{\partial u}{\partial y} + \frac{\partial v}{\partial x}\right)\right] \tag{3.6}$$

where H is the bathymetric depth, D is the total depth including the water level and A_m is the horizontal diffusion coefficient which is calculated for each model grid cell using the Smagorinsky eddy parameterization method (Smagorinsky, 1963) and is given by

$$A_m = 0.5C\Omega\sqrt{\left(\frac{\partial u}{\partial x}\right)^2 + 0.5\left(\frac{\partial v}{\partial x} + \frac{\partial u}{\partial y}\right)^2 + \left(\frac{\partial v}{\partial y}\right)^2} \quad (3.7)$$

where C is a horizontal diffusion coefficient parameter (represented as "HORCON" in FVCOM input file) that can be varied to alter the rate of diffusion and Ω is the area of model grid cell.

In order to accurately represent the irregular variable bottom topography, the governing equations are converted in FVCOM using σ co-ordinate transformation system in the vertical direction. The governing equations are solved in the integral form by computing fluxes between horizontal triangular control volumes (unstructured grid) thereby providing a better representation of the conservative laws of mass and momentum especially in coastal regions with complex geometry. This finite-volume approach used in FVCOM combines the best of finite-element methods for geometric flexibility and best of finite-difference methods for simple discrete structures and computational efficiency. For the speed-up of modelling calculations, FVCOM is parallelized using a Single Processor Multiple Data (SPMD) approach. The computational domain is decomposed using the METIS graph partitioning libraries and the inter-processor communication is explicitly defined using Message Passing Interface (MPI) calls. Therefore FVCOM is highly suitable for solving large-scale tidal flow problems in three-dimensions and at very fine grid resolutions.

FVCOM includes a wet/dry point treatment technique to simulate the flooding and draining processes over the intertidal zones in the estuary. In this technique, wet and dry points in the computational domain are distinguished through the local total water depth (D) calculated as the sum of mean water depth and surface elevation. If 'D' is greater than 'D_{min}', the thickness of the viscous layer specified at the bottom, the grid cells are treated as wet and vice-versa. A grid cell treated as dry will be assigned zero velocity with no flux entering through the boundaries to facilitate total mass conservation.

Bottom friction in the model is calculated using a drag coefficient (C_d) formulation:

$$\tau_x, \tau_y = \rho * C_d * \sqrt{u^2 + v^2} * (u, v) \tag{3.8}$$

where ρ is the density of water, and τ_x, τ_y are the bed shear stresses in x, y directions respectively. The drag coefficient C_d is determined by matching a logarithmic bottom layer at a height z_{ab} above the bottom, i.e.,

$$C_d = max\left(k^2/ln\left(\frac{z_{ab}}{z_0}\right)^2, f\right) \tag{3.9}$$

where $k = 0.4$ is the von Karman constant, z_0 is the bottom roughness parameter, and f is the input friction coefficient that can be varied. For the modelling of marshes in the Ogeechee Estuary, f is enhanced to various degrees for grid cells with mean water depth greater than zero, i.e., the intertidal zones, to represent the additional drag caused by marsh vegetation.

FVCOM includes a biological / water quality model that can be used to simulate various biological processes that affect the water quality in coastal waters such as the interaction of nutrients & phosphates with phytoplankton, zooplankton and bacteria. In addition, FVCOM includes a simple advection-dispersion model that can be used to simulate the transport of pollutants that are primarily affected by the governing hydrodynamic processes. This model solves the following transport equation to model the transport of pollutants in the computational domain:

$$\frac{\partial C}{\partial t} + u\frac{\partial C}{\partial x} + v\frac{\partial C}{\partial y} + w\frac{\partial C}{\partial z} = \frac{\partial}{\partial z}\left(K_h \frac{\partial C}{\partial z}\right) + F_c + F_d \tag{3.10}$$

where C is the concentration of the pollutant, K_h is the vertical eddy diffusion coefficient, F_c is the horizontal diffusion term, and F_d is the sink term for pollutants. For the purpose of faecal coliform modelling in Swansea Bay, sink term in the transport equation is represented by using a first order decay formulation according to Chick's Law (Chick, 1910) and given as:

$$\frac{\partial C}{\partial t} = -KC \tag{3.11}$$

where: K = first-order decay coefficient calculated as equal to $2.303/T_{90}$, with T_{90} being the time taken for decay of bacteria to 10% of its initial concentration.

In summary, FVCOM model is very suitable for this research in view of its unstructured grid approach, multi-processing capabilities, inclusion of wetting/drying scheme and faecal coliform modelling capabilities. The following two chapters present the application of FVCOM model towards assessment of hydro-kinetic energy, and assessment of bathing water quality associated with faecal coliform transport in coastal waters.

Chapter 4

Hydro-kinetic energy assessment for Rose Dhu Island, GA, USA

In this chapter details of a numerical modelling study carried out towards an assessment of available tidal stream energy at Rose Dhu Island, GA, USA are presented. Firstly a brief description of the site is provided along with the objectives and scope of this study. Next, a description of the available data from field measurements carried out as a part of the project is presented. Then, details of the computational modelling performed for energy assessment at Rose Dhu Island are provided. Following this, details of model simulations performed towards an investigation of tidal asymmetry in Ogeechee Estuary are presented. Finally, this chapter concludes with a summary of the findings from this study.

4.1 Introduction

Rose Dhu Island is a small island located in the coastal state of Georgia, USA. It is at the confluence of several rivers (Forest river, Little Ogeechee river, Vernon river and Grove river), upstream of Ossabaw Sound (location shown in Figure 4.1). The Girl Scouts of Historic Georgia have owned Rose Dhu Island since the 1950's; using it as a campground and meeting venue for Girl Scouts of all ages. They intend to create a sustainable "Eco Village" on Rose Dhu Island as well as an adjacent Science Centre where environmental science and biology will be taught. The Eco Village will promote and demonstrate the feasibility of creating the first fully sustainable microcosm model in coastal Georgia, injecting environmental responsibility to the coastal community via an educational component, sustainable design, and sustainable energy practices. To help accomplish this goal, the Eco Village will be powered by renewable energy sources.

Therefore, tidal stream flow around the island is evaluated as one of the potential clean sources of energy that can be harvested to power the eco-village and its components.

Figure 4.1: Map of Ogeechee Estuary. Orange highlighted area marks Rose Dhu Island. Yellow and pink highlighted areas mark, as referred to this study, west and east channels respectively. Red Star indicates location of GPS base station. Inset image: Map of Southeastern United States for geographic reference.

The Ogeechee Estuary shown in Figure 4.1 is a coastal plain system characterized by slow freshwater flow rates, a far reaching saline zone, and a large proportion of wetlands (Dame et al. 2000). Although it originates 245 miles from the coast in the piedmont of Georgia, the majority of its flow comes from within the coastal plain, has little freshwater input, and is considered well-mixed. Due to the sinuous networked channels with variable bathymetry, the Ogeechee boasts some of the largest tidal ranges in the Southeastern United States (Dame et al. 2000). Moreover, the presence of constricted channels amplifies tidal amplitudes and currents and thereby provides the possibility of extracting tidal power.

The extensive wetlands of the Ogeechee estuarine system provide intertidal storage during the times when tidal water levels are significantly higher than the mean channel depth. A previous field-measurement based study in the Ogeechee Estuary (Blanton et al. 2002) and other studies in the estuaries nearby (Huang et al. 2008) have suggested that the wetlands play a significant role in distorting tidal flow in the estuary. However, a detailed assessment of their influence, such as the role played by intertidal storage volume or friction associated with vegetation in the marshes, is not yet available to fully understand the factors contributing towards tidal asymmetry.

The main objective of the present study is to perform high-resolution modelling of tidal flow in Ogeechee Estuary and to evaluate the tidal stream energy potential at Rose Dhu Island. In addition, this study aims to investigate tidal asymmetry in the estuary through several simulations by varying the model parameters associated with bottom friction and intertidal storage. The scope of this study includes:

a) Conduct 3D numerical simulations of tidal flow in Ogeechee Estuary, GA using the FVCOM model.
b) Utilise data from field measurements carried out recently (see section 4.2) to compare and validate the numerical model predictions.
c) Identify hotspots of hydro-kinetic energy and perform a quantitative assessment of energy potential for Rose Dhu Island, GA.
d) Perform model simulations by varying parameters related to bottom friction and intertidal wetlands to investigate their importance in distorting tidal flow in the Ogeechee Estuary.

4.2 Field Measurements

In order to support the numerical model, field data consisting of bathymetry, water surface height and current velocity measurements near Rose Dhu Island are utilized in this study. The field campaign was executed by Georgia Institute of Technology, Savannah, GA, USA through cruises aboard a 28ft pontoon motorboat over three days (October 19, 20 and December 29) in 2010 and two days (November 27, December 22) in 2011. Measurements were obtained by a fathometer assembly with a transducer deployed through a hole near the bow of the vessel coupled with a bottom-tracking Acoustic Doppler Current Profiler (ADCP) mounted off the front of the bow. This instrument system produced simultaneous measurements of the water depth and current velocity profile of the water column underneath the bow of the moving boat. Continuous GPS positionings were recorded to track the locations of the ADCP and fathometer measurements.

The GPS system, employed to determine the x-y-z positioning of the survey vessel consisted of a boat mounted Ashtech Z-Surveyor (2010) or ProFlex 500 (2011) dual-frequency receiver along with an Ashtech Z-12 (2010) or ProFlex 500 (2011) dual-frequency receiver at a fixed base station. The base station, located at a nearby boat ramp (location indicated in Figure 4.1), was used to eliminate time-dependent position error from the roving receiver. Data, procured at 2 Hz, was logged using the Hypack Software and post-processed using GrafNav Software to apply kinematic corrections allowing for the lateral and vertical position of the boat to be measured. Alongside GPS measurements, depth measurements were made with a Bruttour Ceeducer digital fathometer using a 200 kHz, narrow beam transducer. The depths, observed at 2 Hz, were logged concurrently with the GPS using the HyPack software. The GPS and fathometer were used in tandem to measure, relative to a mean water level datum, the North American Vertical Datum of 1988 (NAVD88), the elevation of the sea floor as well as the water surface height. As the fathometer measured the depth from the transducer to the seafloor, the GPS simultaneously measured the height of the antenna mounted on the top of the vessel. Thus the elevation of the seafloor ($z_{seafloor}$) was found by

$$z_{seafloor} = z_{ant} - h_{ant} - d_{fath} \tag{4.1}$$

where z_{ant} is the vertical coordinate of the GPS antenna as measured by the GPS, h_{ant} is the fixed vertical distance from the fathometer transducer to the GPS antenna, and

d_{fath} is the depth of the seafloor as measured by the fathometer. Relative water surface heights (ξ) relative to mean water level were calculated similarly by

$$\xi = z_{ant} - h_{ant} + d_{fw} - datum \tag{4.2}$$

where $d_{fw}$is the estimated fixed distance between the fathometer transducer and the water surface as observed through the hole in the deck. "$datum$" is the conversion to the mean water level datum set from NAVD88.

Current measurements were obtained from a RD Instruments Express Sentinel Self-contained ADCP at a sampling rate of 2 Hz. Current velocities were measured along the water column with the first cell 1.27m below the surface. The water column was divided into vertical bins of 0.5m, for which the current measurements were then bin averaged and recorded by the instrument. Current velocity data collected during the boat based surveys were synchronized with the position data provided by the GPS to provide coordinates of the ADCP measurements.

Measurements on each day (October 19 and 20, 2010) included about eight hours of surveying: five hours for observing the peak ebb flow in the morning and three hours for observing the peak flood in the afternoon, limited due to lack of daylight. The surveying strategy, for both flood and ebb tides on each day, consisted of travelling up the channel and 'zig-zagging' between predetermined waypoints on either bank. The waypoints, situated approximately 500m apart, created non-nominal cross-channel transects. Once all predetermined transects were completed, additional smaller 'zig-zags' were made along channel banks for as long as time permitted, resulting in ebb having more measurements than flood. These ancillary measurements focused on the channel banks adjacent to Rose Dhu Island due to the location's logistical importance for a potential tidal turbine installation as well as to serve as important benchmarks for model validation for the complex flow near the marsh boundaries. Figure 4.2 shows a plot of the field tracks and depth-averaged velocity contours at the island as obtained from the measurements.

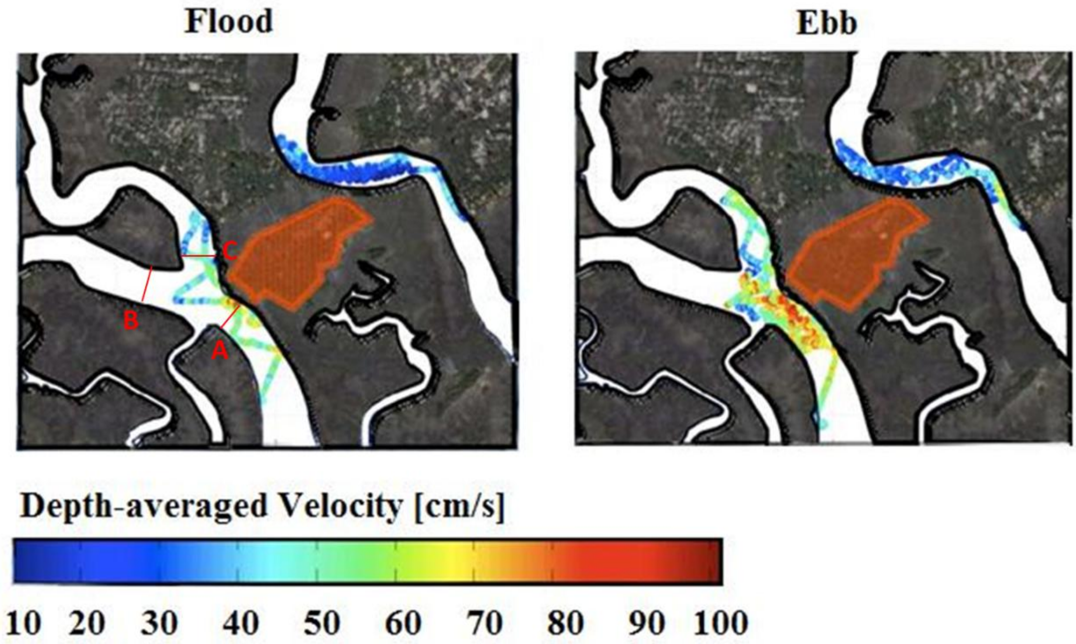

Figure 4.2: Depth-averaged velocity contours obtained from field measurements on two separate days in 2010; A, B and C are three transects along which measurements were carried out in 2011

Additional field measurements were carried out on November 27 and December 22, 2011 to gain further insight into the hydrodynamic differences between the ebb and flood tidal flows surrounding Rose Dhu. Boat based ADCP measurements, as in the previous field campaign, were taken along three predetermined transects (shown as A, B and C in Figure 4.2) multiple times. The transects were positioned to observe the most dynamic and energetic areas of the channel. Moreover, fewer transects were charted over a smaller spatial domain, allowing for individual transects to be measured at a higher temporal frequency throughout the tidal cycle to better resolve the evolution of the flow in the channel during the tidal cycle.

4.3 Numerical Model Setup

Details of the numerical model setup including the computational domain, numerical grid, bathymetry, and boundary conditions are presented below.

4.3.1 Computational Domain

The computational domain of the numerical model covers the entire Ogeechee Estuary including the main channel and inter-tidal marsh zones (wetlands). The following are the steps used in the generation of computational domain.

1) Firstly the coastline is extracted using the US National Oceanic and Atmospheric Administration (NOAA) coastline extractor tool (http://www.ngdc.noaa.gov/mgg/coast/) by specifying the approximate latitude and longitude values of the region of interest as shown in Figure 4.3.

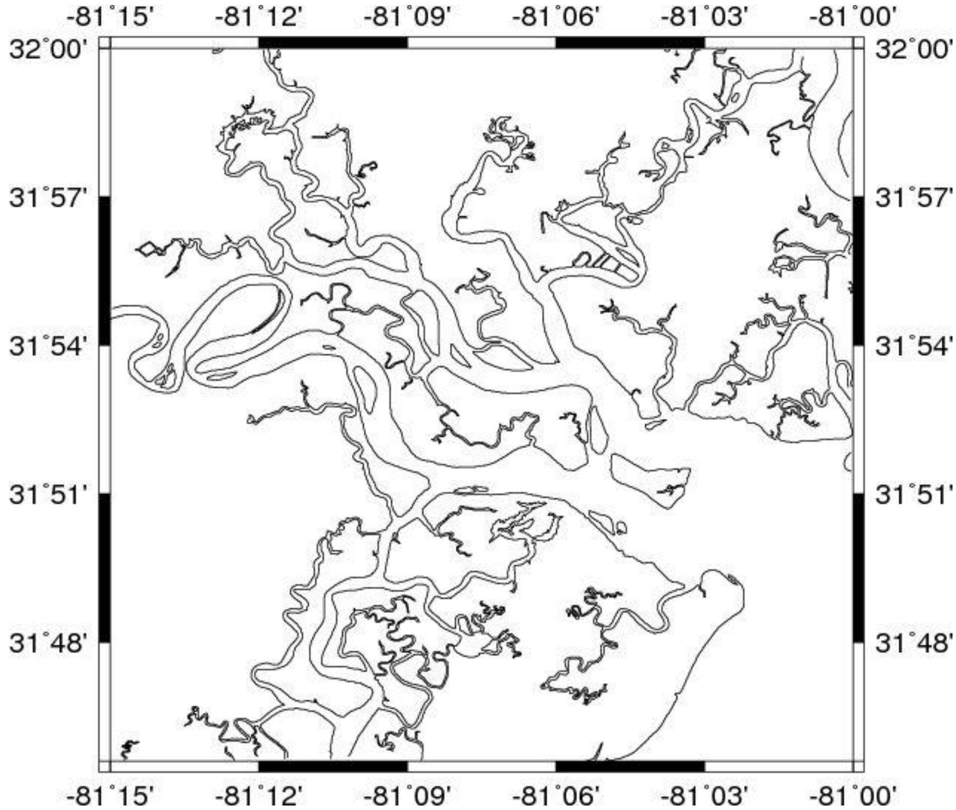

Figure 4.3: Map of the Ogeechee Estuary obtained from the US National Oceanic and Atmospheric Administration coastline extractor (http://www.ngdc.noaa.gov/mgg/coast/)

2) Next, the wetland boundaries are obtained from the National Wetlands Inventory (NWI) of the US Fish and Wildlife Services as shown in Figure 4.4.

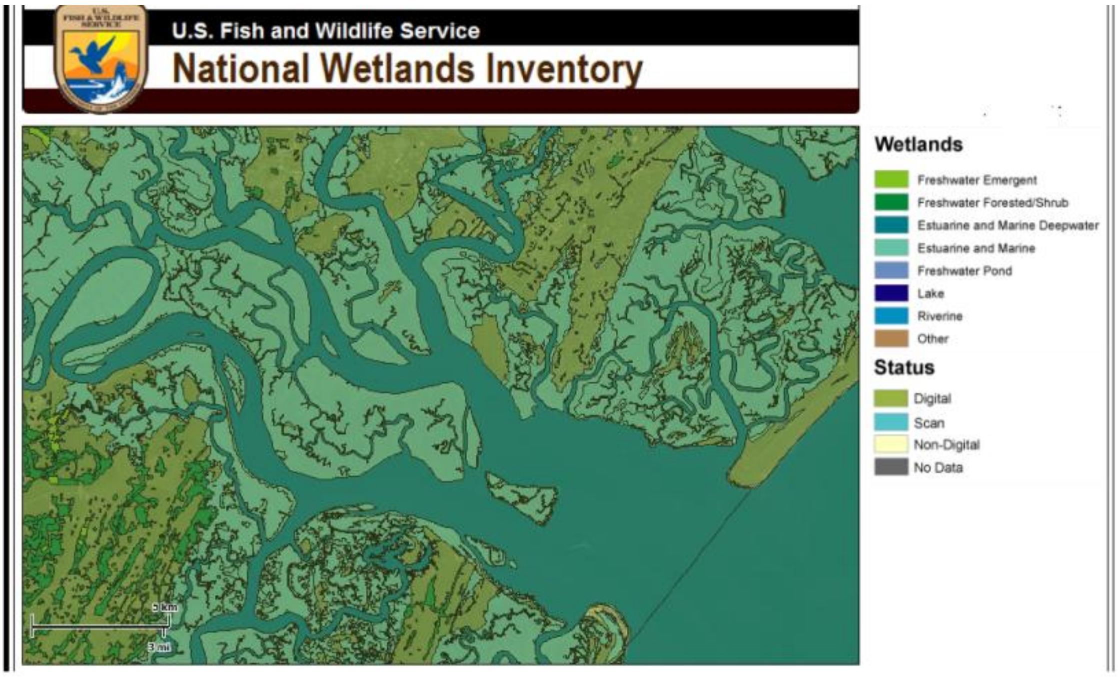

Figure 4.4: Map of the wetlands obtained from the National Wetlands Inventory of the US Fish and Wildlife Services

3) Finally, the computational domain is created by combining the two files using the Surface-water Modeling System (SMS) grid generation software (http://www.aquaveo.com/) as shown in Figure 4.5.

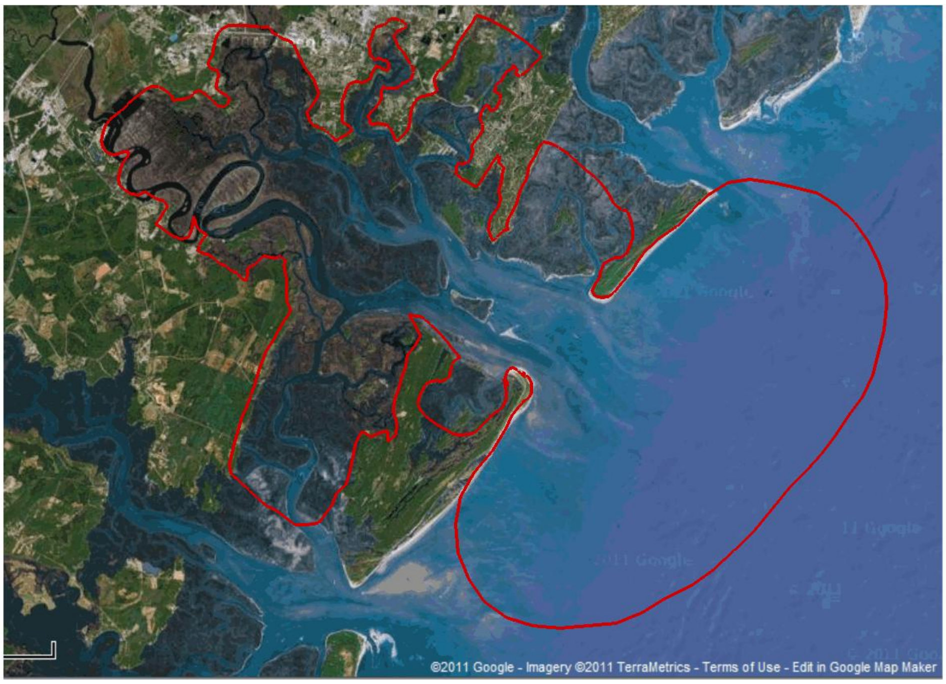

Figure 4.5: Computational domain of the present study

4.3.2 Numerical Grid

In the numerical model, unstructured triangular grids are utilized to discretise the computational domain. The numerical grid at the open boundary located in the ocean is relatively coarse with a spacing of ~300m. However, at regions close to the Rose Dhu Island, a relatively fine grid is employed with a spacing of ~50m. A total number of five layers (equal thickness) are used in the vertical direction to resolve the water column. The number of vertical layers is selected based on sensitivity testing carried out during the model build process. Figure 4.6 shows the computational grid in the horizontal direction.

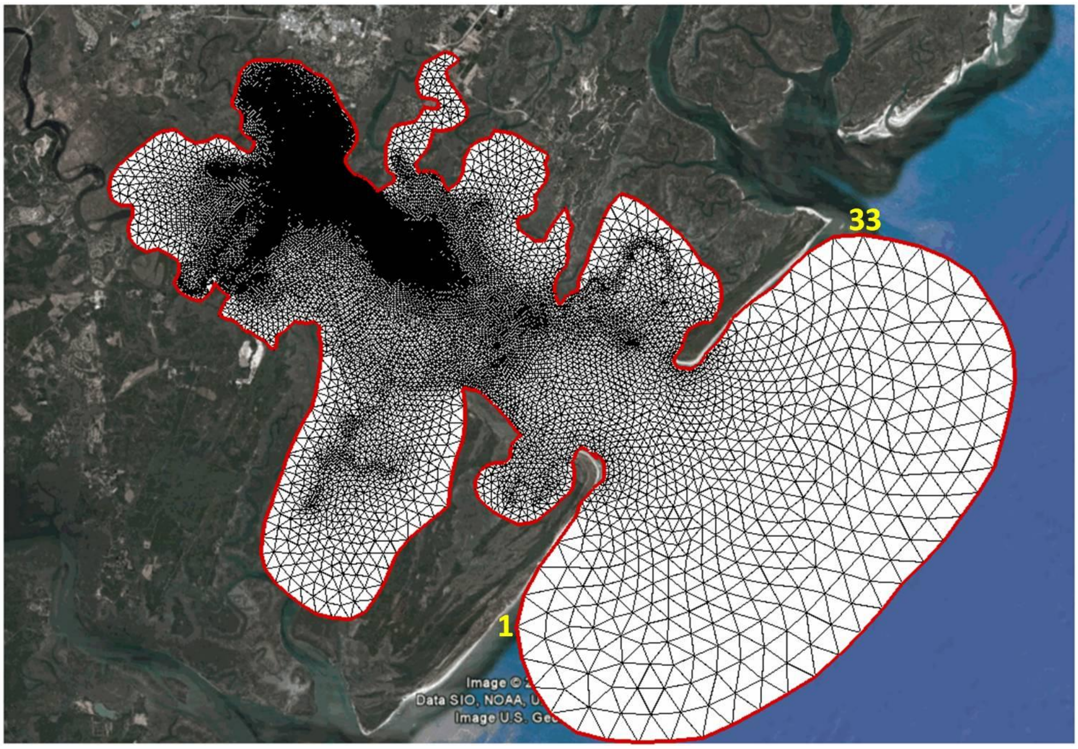

Figure 4.6: Numerical grid employed in the present study. Numbers in yellow indicate the anti-clockwise numbering (1 to 33) used for the 33 grid nodes along the open boundary.

4.3.3 Bathymetry

The mean water depth at each of the numerical grid points is calculated through an interpolation of bathymetric data consisting of field measurements close to the Rose

Dhu Island, survey data from the NOAA database, and wetlands elevation data from the United States Geological Survey (USGS). Figure 4.7 shows the contours of mean water depth obtained after interpolation of the bathymetric data. The observed variability in water depth indicates heterogeneity in channel characteristics (like the sinuosity or presence of small barrier islands) that can possibly lead to a local acceleration/deceleration of the flow.

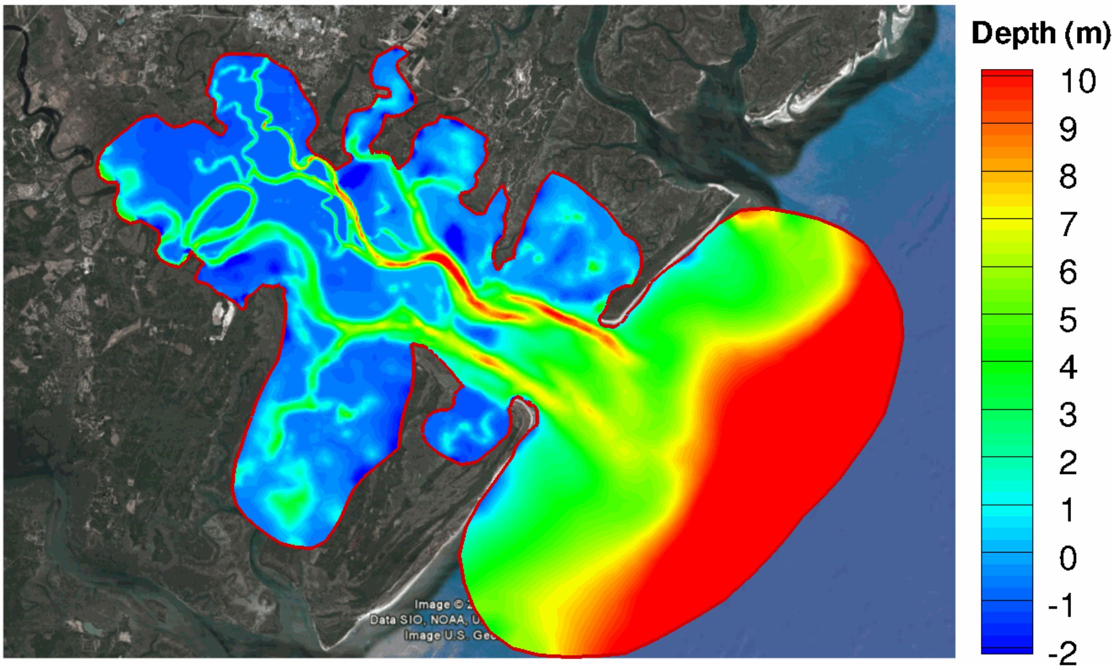

Figure 4.7: Contours of the bathymetry in the computational domain

4.3.4 Boundary Conditions

The model is driven by 6 major tidal constituents (S2, M2, N2, K2, K1, and O1) specified at the open boundary; the amplitude and phase of which are computed from the ADCIRC tidal database (http://adcirc.org/products/adcirc-tidal-databases/). The ADCIRC model used to generate the database covers the entire Western North Atlantic Ocean region and has been validated using data for tidal elevation stations with amplitude error within 10% and phase error within 20-degree (Mukai et al. 2002). Table 4.1 presents the amplitude and phase values extracted from the database at 33 grid nodes along the open boundary (id of the grid nodes is indicated in Figure 4.6). The M2 is the dominant constituent with tidal amplitude values around 90cm. The next dominant constituents are S2 and N2 with tidal amplitude values around 20cm.

Table 4.1: Amplitude (A, cm) and phase (ϕ, degrees) values of six tidal constituents specified as boundary conditions in the model

ID	S2		M2		N2		K2		K1		O1	
	A	ϕ	A	ϕ	A	ϕ	A	ϕ	A	ϕ	A	ϕ
1	16.23	21.57	91.99	-223.76	20.77	40.36	3.61	-5.74	11.20	-94.99	8.20	-92.18
2	16.24	21.86	92.08	-223.53	20.78	40.62	3.62	-5.46	11.19	-94.86	8.20	-92.07
3	16.20	21.63	91.82	-223.68	20.74	40.42	3.60	-5.67	11.19	-94.95	8.20	-92.13
4	16.15	21.46	91.57	-223.79	20.69	40.26	3.59	-5.81	11.18	-95.01	8.19	-92.18
5	16.10	21.39	91.32	-223.82	20.63	40.20	3.58	-5.86	11.17	-95.04	8.19	-92.21
6	16.03	21.11	90.93	-223.99	20.55	39.95	3.56	-6.13	11.16	-95.18	8.18	-92.31
7	15.98	20.93	90.65	-224.13	20.49	39.77	3.55	-6.30	11.15	-95.27	8.18	-92.39
8	15.94	20.80	90.47	-224.24	20.45	39.65	3.54	-6.42	11.15	-95.34	8.18	-92.45
9	15.90	20.65	90.22	-224.37	20.40	39.51	3.53	-6.57	11.14	-95.42	8.17	-92.52
10	15.86	20.55	90.01	-224.45	20.35	39.42	3.53	-6.66	11.13	-95.47	8.17	-92.56
11	15.82	20.39	89.79	-224.57	20.31	39.27	3.52	-6.80	11.12	-95.55	8.16	-92.63
12	15.79	20.19	89.61	-224.75	20.27	39.08	3.51	-7.00	11.12	-95.65	8.16	-92.72
13	15.77	20.02	89.45	-224.91	20.24	38.92	3.50	-7.17	11.11	-95.73	8.16	-92.79
14	15.75	19.84	89.33	-225.07	20.21	38.76	3.50	-7.34	11.11	-95.82	8.16	-92.86
15	15.74	19.66	89.22	-225.24	20.19	38.59	3.50	-7.53	11.11	-95.91	8.15	-92.94
16	15.71	19.51	89.08	-225.36	20.16	38.45	3.49	-7.67	11.10	-95.98	8.15	-93.01
17	15.69	19.36	88.94	-225.50	20.13	38.32	3.48	-7.82	11.10	-96.05	8.15	-93.08
18	15.67	19.23	88.82	134.40	20.11	38.20	3.48	-7.95	11.10	-96.11	8.15	-93.13
19	15.64	19.18	88.69	134.35	20.08	38.15	3.47	-8.01	11.09	-96.15	8.14	-93.17
20	15.62	19.00	88.57	134.20	20.06	37.99	3.47	-8.18	11.09	-96.22	8.14	-93.24
21	15.60	18.81	88.44	134.01	20.03	37.82	3.47	-8.38	11.08	-96.30	8.14	-93.31
22	15.59	18.67	88.34	133.89	20.01	37.68	3.46	-8.52	11.08	-96.37	8.14	-93.37
23	15.58	18.55	88.29	133.78	20.00	37.58	3.46	-8.64	11.08	-96.42	8.14	-93.42
24	15.58	18.43	88.26	133.67	20.00	37.47	3.46	-8.77	11.08	-96.47	8.14	-93.47
25	15.58	18.30	88.27	133.55	20.00	37.36	3.46	-8.90	11.08	-96.52	8.14	-93.52
26	15.60	18.18	88.32	133.44	20.01	37.25	3.46	-9.02	11.08	-96.57	8.14	-93.56
27	15.62	18.10	88.45	133.35	20.04	37.18	3.47	-9.10	11.09	-96.60	8.14	-93.59
28	15.65	18.08	88.59	133.31	20.07	37.16	3.48	-9.15	11.09	-96.60	8.14	-93.60
29	15.69	18.05	88.75	133.26	20.11	37.14	3.49	-9.18	11.10	-96.62	8.15	-93.61
30	15.73	18.03	89.00	133.23	20.16	37.12	3.50	-9.20	11.11	-96.61	8.15	-93.61
31	15.78	18.11	89.25	133.26	20.21	37.19	3.51	-9.14	11.11	-96.57	8.16	-93.59
32	15.83	18.28	89.53	133.37	20.27	37.35	3.52	-8.98	11.12	-96.50	8.16	-93.53
33	15.87	18.34	89.75	133.40	20.32	37.40	3.53	-8.94	11.13	-96.47	8.16	-93.51

Within the computational domain, the water levels and current magnitudes are zero initially and tidal forcing at the open boundary is ramped up to its actual value over two days to avoid any numerical instability. In total, the model is run over a 32 day period (September 29 to October 30, 2010) such that both spring and neap tides within a lunar month are simulated. Stream water input is not included in the model because this estuary is primarily tidally driven with a very small watershed and minimal freshwater flow. This is confirmed by comparing the measured average freshwater discharge value (approximately equal to 50m^3/s; Dame et al. 2000) to the calculated tidal volume flux at the mouth of the estuary (approximately equal to 50,000m^3/s) which is more than 1000 times higher.

4.3.5 FVCOM Model Parameters

The simulations are performed using the 3D version of the FVCOM model in baroclinic mode. Details of various model parameters including grid resolution, time step, friction coefficient, horizontal diffusion and vertical diffusion are presented in Table 4.2. All the parameters were selected through experimentation/model calibration and by referring to the guidance available in FVCOM manual.

Table 4.2: Ogeechee Estuary Model Parameters

Horizontal grid resolution	~50m at Rose Dhu Island ~300m at open boundary
Number of horizontal grid nodes	16280
Number of horizontal grid cells	32047
Number of vertical layers	5
External mode time step, DTE	0.25s
Ratio of external to internal model time step, ISPLIT	10
Internal mode time step, DTI	2.5s
Wet/Dry cell bottom thickness, MIN_DEPTH	0.05m
Bottom stress drag coefficient, BFRIC	0.0025
Bottom roughness height, Z0B	0.001
Horizontal diffusion calculation method	Smagorinsky Formulation
Smagorinsky horizontal diffusion coefficient, HORCON	0.2
Turbulence Model	Mellor Yamada level 2.5
Background mixing coefficient, UMOL	0.0001

4.4 Results and Discussion

Results from the numerical simulation are visualised in Figure 4.8 and Figure 4.9 through contours of depth-averaged current magnitudes plotted for a selected time-instance when the water enters and leaves the estuary, i.e. during the flood and ebb tides respectively. The current magnitudes are quite low close to the ocean because of the presence of relatively deep water and wide channel geometry. At some locations, especially where channel constrictions or shallow water depths are encountered, higher current magnitudes can be observed due to local flow acceleration.

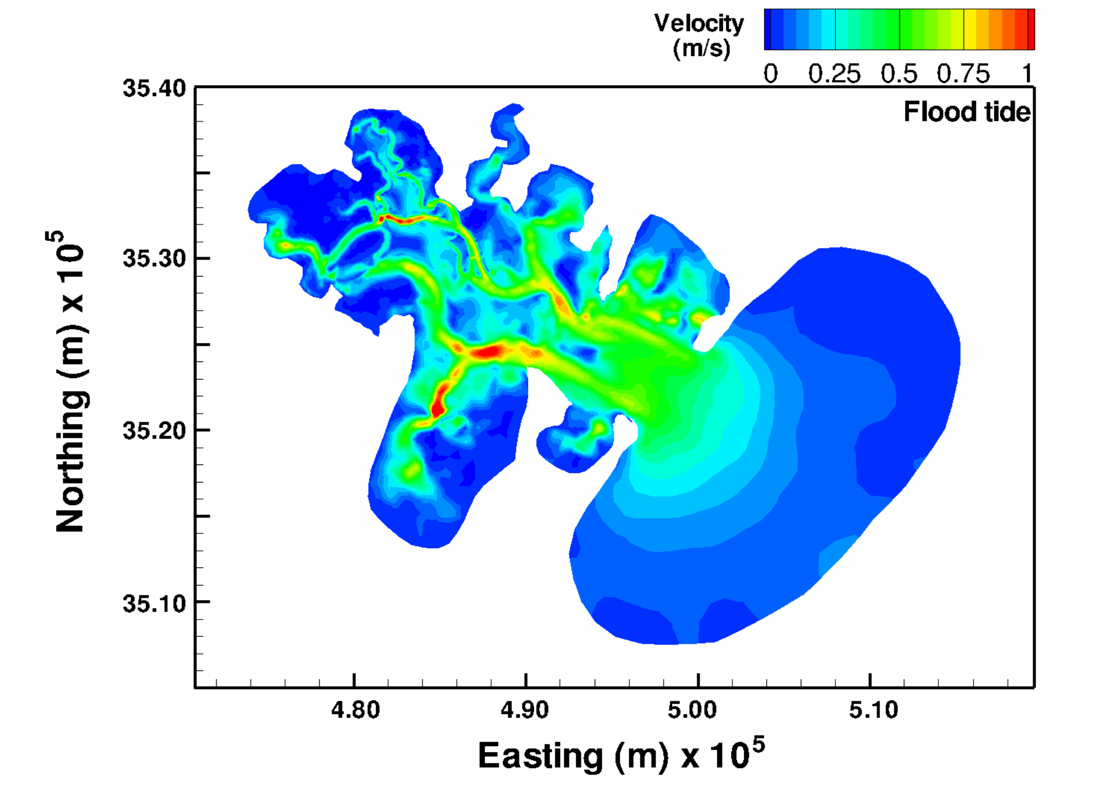

Figure 4.8: Contours of the depth-averaged current magnitude in the entire Ogeechee Estuary for a flood tide

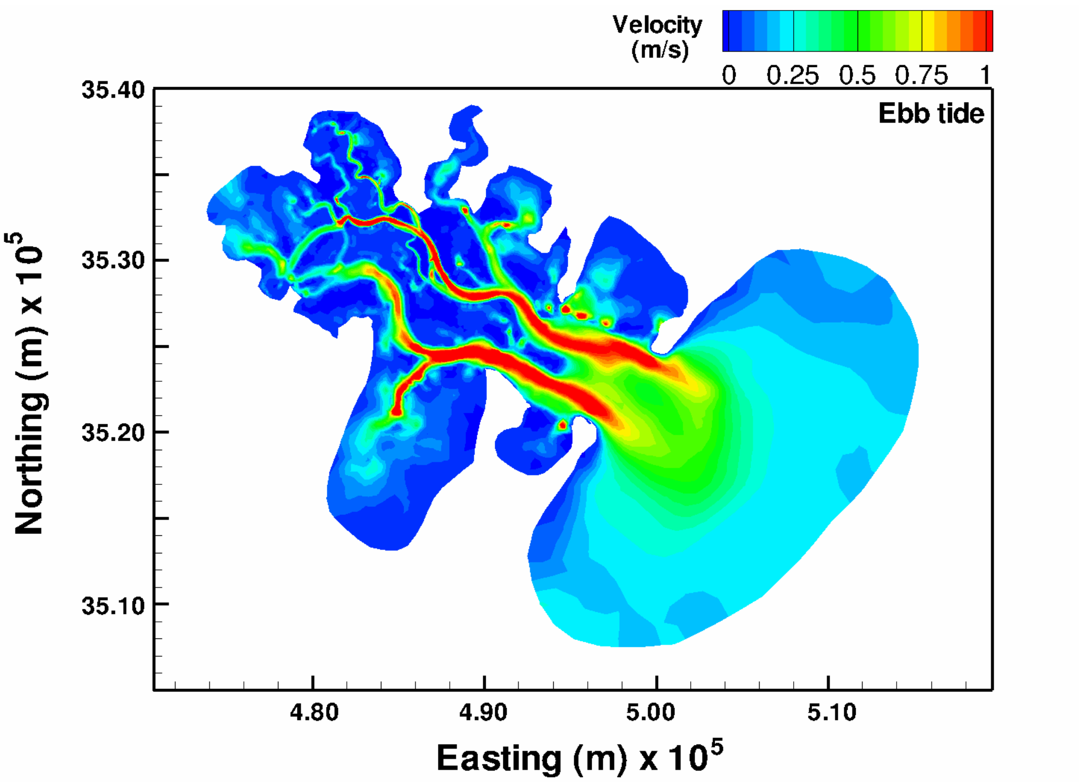

Figure 4.9: Contours of the depth-averaged current magnitude in the entire Ogeechee Estuary for an ebb tide

A comparison of Figure 4.8 and Figure 4.9 indicate that the ebb tide currents are much stronger than the flood tide currents causing tidal asymmetry in the Ogeechee Estuary. Huang et al. (2008) in their numerical studies of tidal flow in Okatee Creek, South Carolina, USA reported a similar behaviour and suggested that the storage volume provided by intertidal zones/wetlands play a significant role in the production of tidal asymmetry. During a flood tide when water enters the estuary, excess water in the main channel fills up the intertidal zones. During an ebb tide when water flows out of the estuary, previously stored water from the intertidal zones flows back into the main channel. Although not presented here, several snapshots of current magnitudes from the simulation clearly visualises this filling and emptying process and thereby reveals the importance of intertidal zones in providing additional storage for water.

4.4.1 Model Validation

Numerical model results are validated through comparison with available field measurement data. Firstly a qualitative comparison of model-predicted results is performed using the data from the first field campaign (i.e. October 2010). This is shown in Figure 4.10 and Figure 4.11 where contours of current magnitudes are compared for flood and ebb tides respectively, at regions close to the Rose Dhu Island.

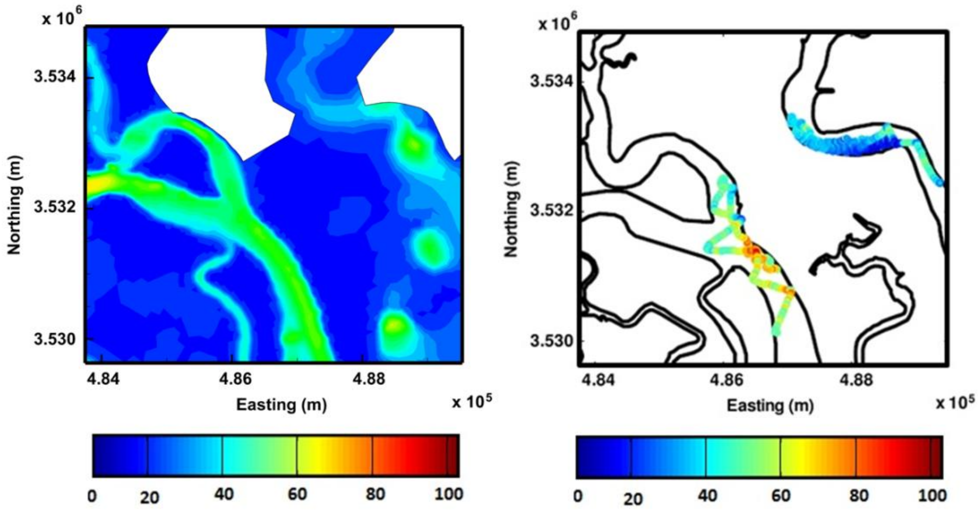

Figure 4.10: Zoomed in contours of the depth-averaged current magnitude (cm/s) close to the Rose Dhu Island for a flood tide, left from the model, right from measurements

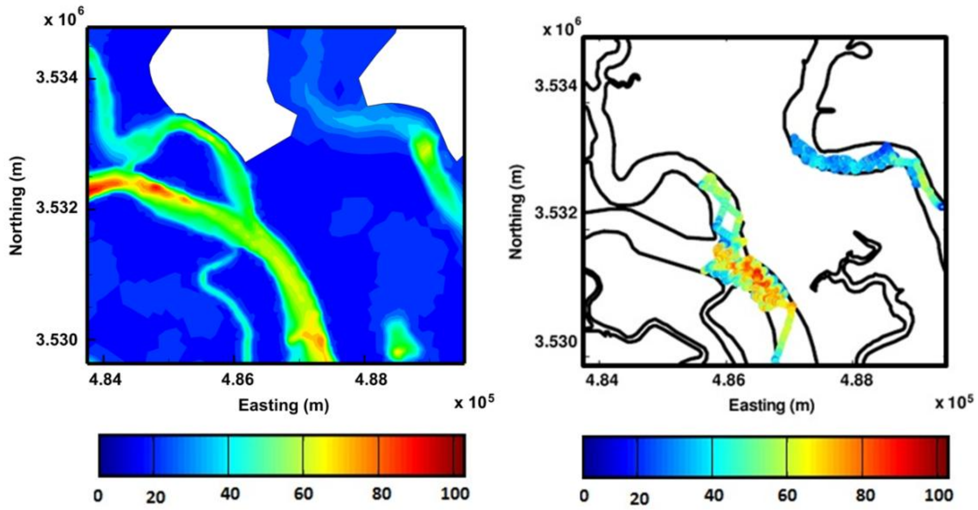

Figure 4.11: Zoomed in contours of the depth-averaged current magnitude (cm/s) close to the Rose Dhu Island for an ebb tide, left from the model, right from measurements

The model successfully captures the spatial variability of current magnitudes observed in the measurements. The currents in the South channel are also greater in magnitude than the currents in the North channel suggesting that the model was able to identify the "hotspots" of kinetic energy previously captured through field measurements.

For a quantitative comparison of numerical results with field measurements, time-series, each a month long starting from October 1, 2010 are extracted from the model. The time-series consist of depth-averaged current velocities in the East and North directions and water surface heights. Since the measurements from the second field campaign (Nov, Dec 2011) are in greater detail and have a better temporal resolution, they are used for comparison. To do this, the model extracted time-series are utilized to project future water surface heights and velocities in 2011, thereby allowing for a one-on-one comparison with measurements from the Nov and Dec 2011 campaign. This projection of model data is achieved through calculation of the tidal constituents via harmonic component analysis (Pawlowicz et al., 2002). Tidal constituents can reconstruct a water surface height signal by the series

$$\eta(t) = \sum_{i=1}^{I} a_i \cos(\omega_i t + \phi_i) \tag{4.3}$$

where $\eta(t)$ is the water surface height for time t, i and I represent the ith constituent and total number of constituents respectively, and a_i, ω_i, and ϕ_i are the amplitude, angular frequency, and phase angle of the ith constituent respectively. Similarly, constituents for current velocities as well can be calculated through the use of complex amplitudes to resolve the directionality of the associated with the velocity.

A water level time series from a grid point in the model near Rose Dhu Island (point 1 in Figure 4.13) is used to compute the harmonic constituents, which are then utilized for constructing time series of the water levels corresponding to the time periods of the measurements. Figure 4.12 shows a quantitative comparison of simulated water levels (represented by the red line) with field measurements (blue line) from four different days. It can be observed that the model-predicted water levels agree relatively well with measurements in 2010 than in 2011. The calculated Root Mean Square Error (RMSE) values between the predicted and observed water levels on October 20, 2010 and December 29, 2010 are 0.19m and 0.06m respectively, whereas, RMSE values between the predicted and observed water levels on November 27, 2011 and December 22, 2011 are 0.38m and 0.27m respectively. Overall, the error values are within 5-10% of the tidal range for 2010 predictions and 15-20% of the tidal range for 2011 predictions and suggest that the projection of 2010 model results to predict water levels in 2011 has reduced model accuracy.

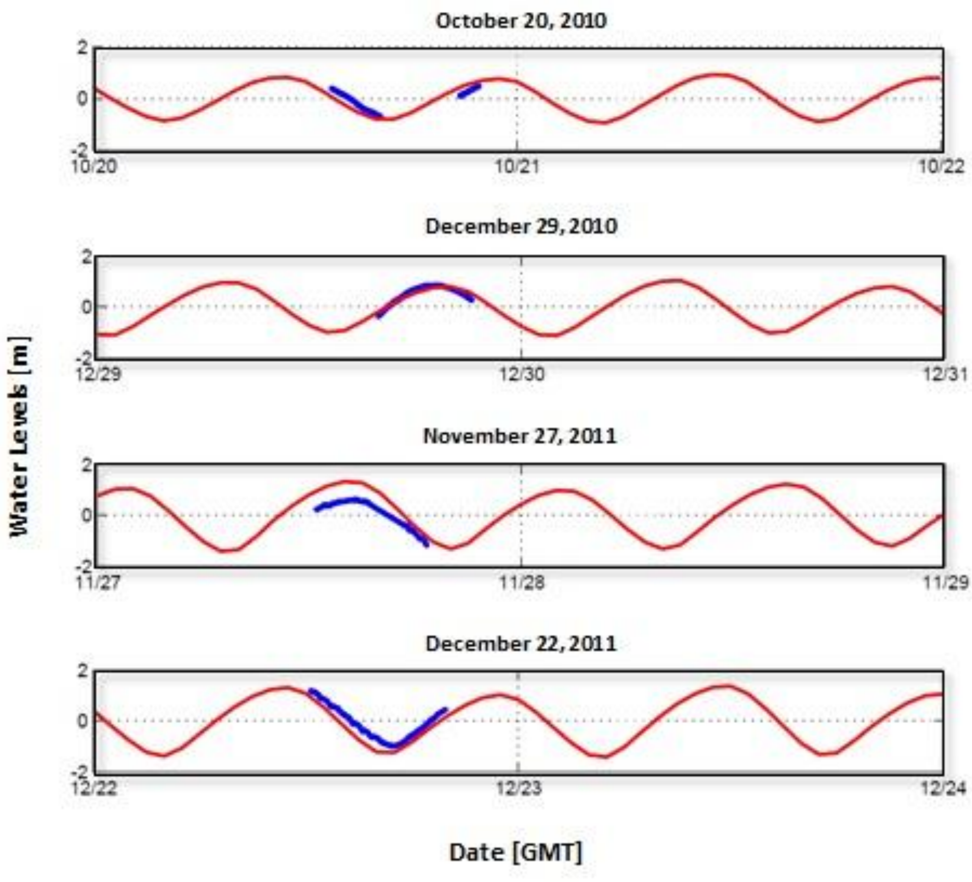

Figure 4.12: Comparison of computed water levels represented by red line against field measurements from four different days represented by blue symbols

For comparison of predicted current velocities with measurements, time-series of velocities from the model are extracted for the grid points along the three transects defined in Figure 4.13. Harmonic analysis is then used to generate time series of the velocity for the times matching the transect measurements from December 22, 2011. Figure 4.13 shows a comparison between computed and measured depth-averaged axial current magnitudes along the three transects A, B, and C, located close to Rose Dhu Island. The axial direction refers to the direction perpendicular to the prescribed transect, which is purposefully oriented in the direction parallel to the channel cross section. For each transect, a rotation of the coordinate system is performed to determine velocity components in the axial direction, where positive values represent flood currents and negative values represent ebb currents.

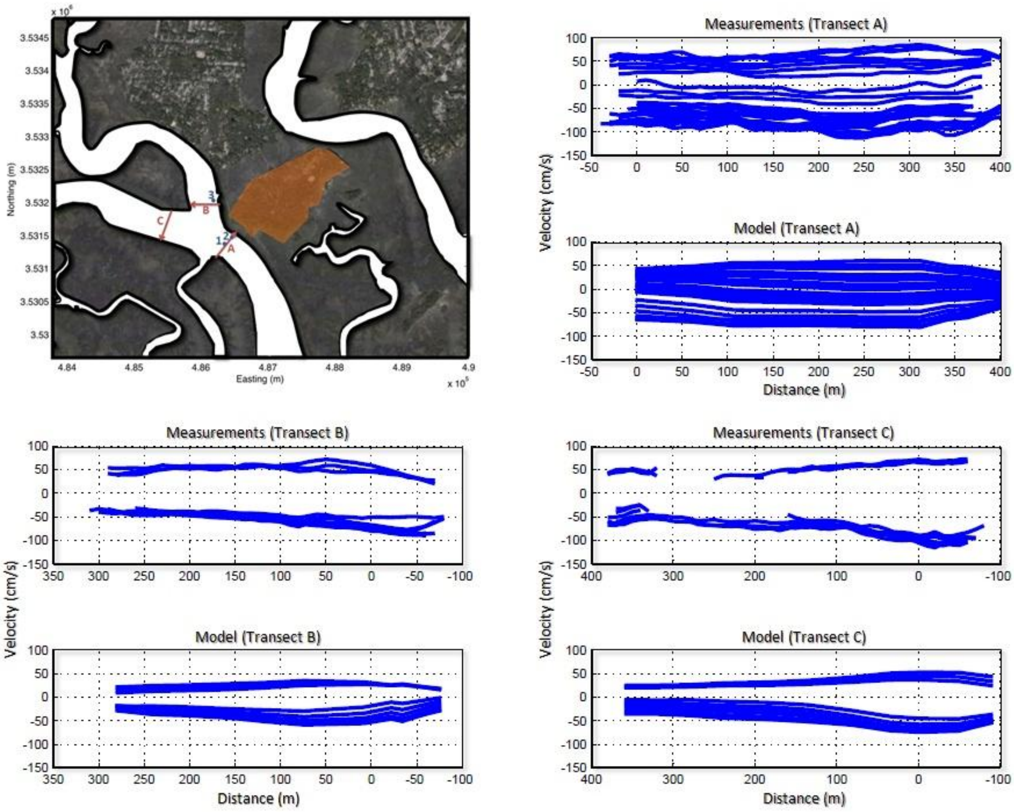

Figure 4.13: Locations of three points (1-3) selected for kinetic power density calculations and transects (A-C) from field measurements in 2011, the shaded region is Rose Dhu Island. Depth-averaged current magnitudes from the three transects for the model and measurements for different times. Positive and negative currents are flood and ebb tide, respectively

It can be observed from Figure 4.13 that the locations of the highs and lows in current magnitudes are well predicted by the model along each of these transects. However the current magnitudes from the model seem to be consistently lower (approximately 30%) than the measured values for most locations within the channel.

In addition to water level and currents, the model is compared against the December 2011 field measurements through a comparison of time varying volume and energy fluxes for transects A, B, and C. The total volume flux across a transect, Q, is calculated as

$$Q = \sum_{n=1}^{N} \bar{a}_n w_n h_n = \sum_{n=1}^{N} q_n \tag{4.4}$$

where for both model and field, N represents the total number of data points along the transect, w_n is the distance along the transect between the midpoints of the two adjacent data points, h_n is the depth, $\bar{a}_n$ is the depth averaged velocity component in the axial direction, and q_n is the volume flux associated with a given data point. The total kinetic energy flux, E, is calculated as a function of volume flux and kinetic energy

$$E = \sum_{n=1}^{N} q_n \left(\frac{1}{2}\rho \bar{u}_n{}^2\right) \tag{4.5}$$

where ρ is the water density and $\bar{u}_n$ is the depth averaged velocity magnitude for a given point along the transect. For both Q and E, the sign convention associated with axial directionality is retained, negative values refer to an ebb flux and positive refer to a flood flux.

Because each transect was measured multiple times throughout the day, Q is calculated from the field measurements and plotted as a function of time as seen in Figure 4.14. The time associated with each Q is the timestamp of the first data recording for each transect. Model volume fluxes at the same timestamps are similarly calculated from the predicted velocity time-series and also plotted for comparison in Figure 4.14.

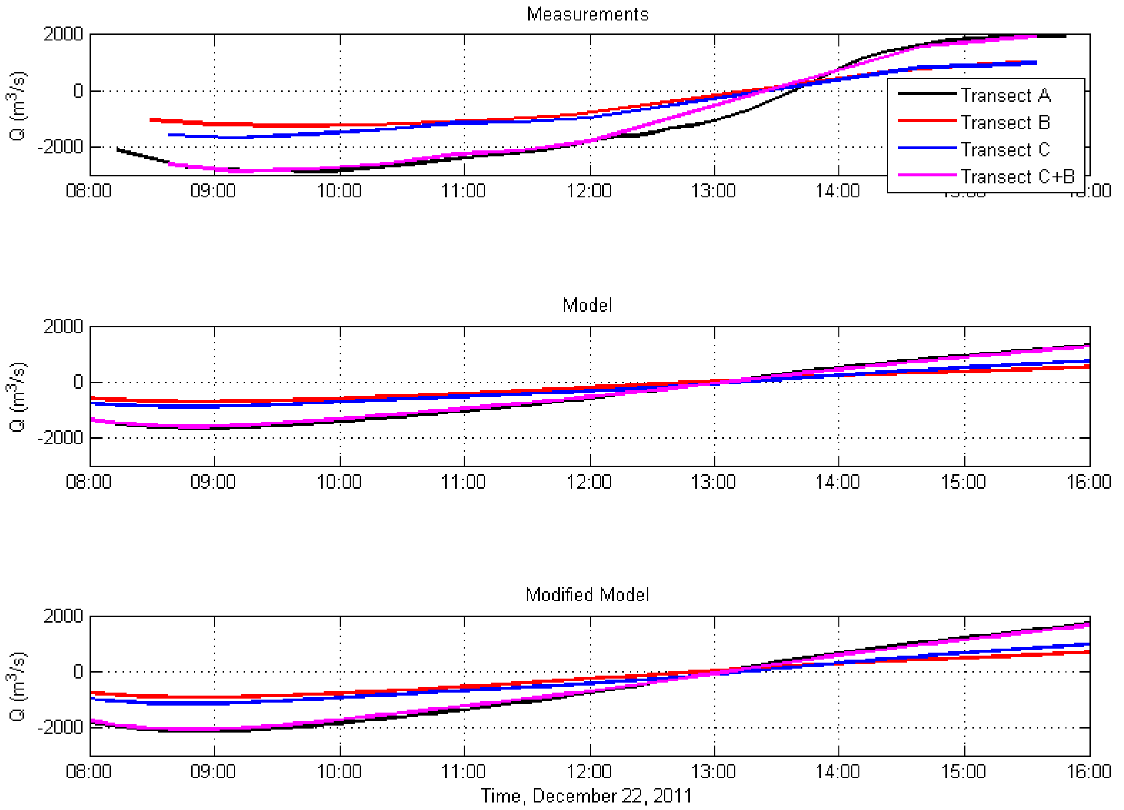

Figure 4.14: Time series of the volume flux for the three transects for the measurements (top), model (middle) and modified model (bottom). Positive and negative fluxes are for flood and ebb tide, respectively

In Figure 4.14, for both the measurement and the model calculations, the Q values share the same qualitative characteristics. The volume fluxes for the transects exhibit a temporal variability corresponding to the observed ebb and flood flow. In addition, the volume fluxes for transects B and C have roughly the same magnitude and when summed have a similar magnitude to transect A. This signifies an equal split/convergence of the incoming flood/ebb flow from transect A at the forking of the channel. Subtle discrepancies between the volume flux of A and summed flux of B and C suggest the prementioned effect of the wetlands. During the ebb tide, the volume flux of transect A is slightly larger than the sum of B and C, signifying an increase in volume from the draining wetlands. During the flood tide, the volume flux of B and C is slightly smaller, suggesting a loss in volume due to the flooding of the wetlands.

Quantitatively, the model, like the current velocities compared in Figure 4.13, under-predicted the volume fluxes by approximately 30%.

Figure 4.15 shows the kinetic energy flux as a function of volume flux determined from both the measurements and model for transect A where again, positive values denote flood tide and negative ebb tide. Not surprisingly, the basic shape of the curves for both the model and measurements show that the kinetic energy flux has a cubic relationship with the volume flux. Interestingly, for ebb tide, it is clear that for a given volume flux there can be quite a different corresponding kinetic energy flux. At the beginning of the ebb tide when the currents are increasing, the water level is higher than during the later portion of the ebb tide when currents are decreasing. Therefore, for a given volume flux, because the water levels are lower in the second half of the ebb tide, to retain the same volume flux the currents must be larger resulting in the kinetic energy flux being much larger. Both the measurements and model clearly show this feature, although again the model (green dots) under-predicts the volume flux and kinetic energy flux.

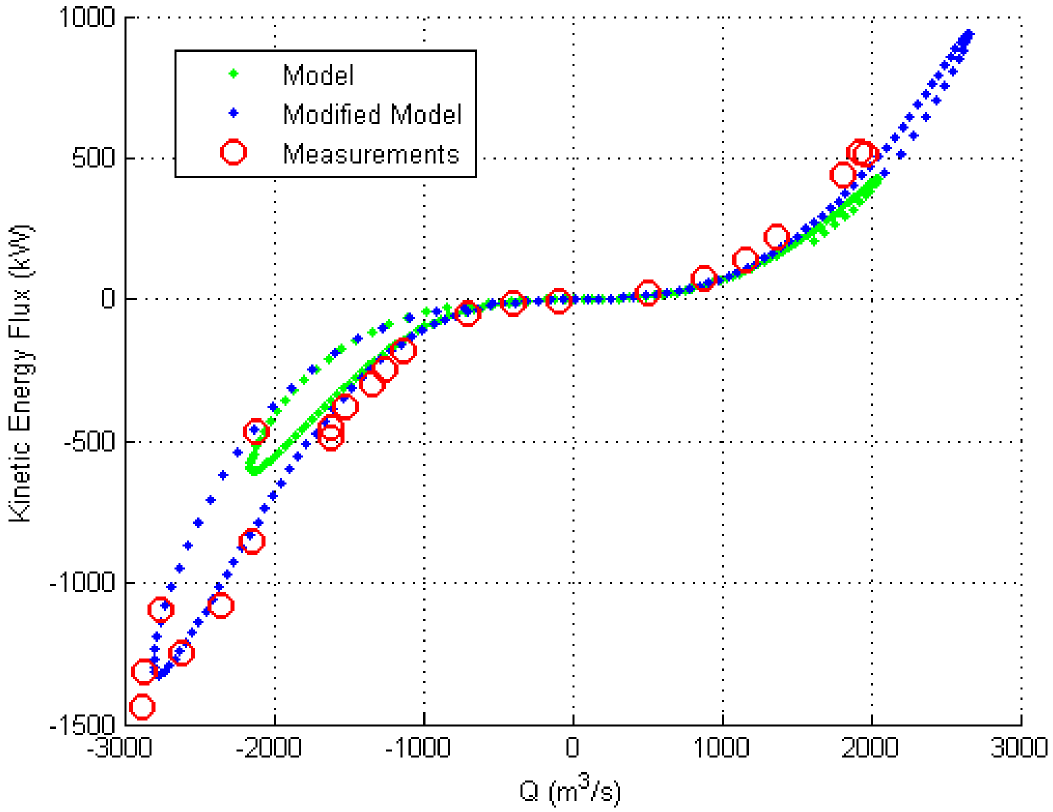

Figure 4.15: The kinetic energy flux as a function of the volume flux for transect A. Positive and negative fluxes are for flood and ebb tide, respectively

The under-prediction of the currents can be attributed to the improper resolution of smaller creeks further inland of Rose Dhu Island in the model. It was observed that the grid cell size used in the model was very large in comparison to the channel width of creeks resulting in the channel elevations being raised to those of the adjacent land masses during interpolation of bathymetric data. Therefore it is believed that the volume of water entering the estuary is significantly lower than that in the field resulting in under-prediction of fluxes and current magnitudes. Another factor affecting the model results could be the bathymetric data used in the model. Although reliable bathymetric data was available from the recent field surveys close to the Rose Dhu Island, data elsewhere (obtained from NOAA) is not believed to be up to date. Most of the NOAA surveys were conducted several decades beforehand and the bathymetry is likely to have changed significantly due to erosion and deposition of sediment in the tidal channels.

This is confirmed by comparing old bathymetric data from the diverse databases with the newly acquired bathymetry from this field campaign.

4.4.2 Tidal Energy Assessment

In order to perform a reasonable assessment of the tidal stream power available for Rose Dhu Island, accurate velocity data must be utilized. Because the model clearly shows a very consistent under-prediction of approximately 30%, a simple solution for achieving the goals of the resource assessment is to scale the existing model results to come into better agreement with the measurements. The scaling is preferred over unphysical calibration of the model to match specific data points, because it would obliterate the predictive capabilities of the model. Therefore, the time-series of the model currents are simply multiplied by a factor of 1.3 to enhance them. The harmonic analysis is then repeated on the model data and the new constituents are used to create the modified model predictions of the volume and kinetic energy fluxes shown in Figure 4.14 and Figure 4.15. Clearly the fluxes from the modified model are in close agreement with the measurements; therefore, the modified model results are used for the resource assessment.

To facilitate the resource assessment, three points in space (Points 1, 2 and 3 in Figure 4.13) are chosen for this analysis, all in close proximity to the 'hot spot' of high current velocities. For each point, tidal constituents are calculated through harmonic component analysis of the modified model data. The resultant amplitudes for each constituent can be seen in Table 4.3. The harmonic component analysis shows that tidal constituents, for all three points, can reconstruct over 98% of the total variance of the original signal for both current velocities and water surface heights. This overwhelming percentage is expected since no other forcing was introduced into the model. The dominant constituent for both current velocity and surface height is M2 (primary lunar semi-diurnal constituent with a period of 12.42 hours), which represents more than 89% of the total variance of each time series. Between points, amplitudes for each surface height constituent are found to be relatively similar. Amplitudes of velocity constituents vary slightly between Points 1 and 2 which can be expected since current velocities have more spatial variability than surface heights due to the hydrodynamics of the channel. Velocity amplitudes of Point 3 are smaller as expected due to the branching of the main channel.

Table 4.3: Harmonic analysis results derived from 31 day record of water surface heights and depth averaged current velocities for each selected point.

Period (Hrs)			
Constituent	**All Points**		
M2	12.42		
N2	12.66		
K1	23.93		
S2	12.00		
O1	25.82		
M4	6.21		
M6	4.14		
Water Surface Height Amplitude (m)			
Constituent	**Point 1**	**Point 2**	**Point 3**
M2	0.960	0.961	0.962
N2	0.197	0.197	0.197
K1	0.118	0.118	0.119
S2	0.182	0.182	0.182
O1	0.084	0.084	0.085
M4	0.080	0.080	0.083
M6	0.017	0.017	0.016
Current Velocity Amplitude (m/s)			
Constituent	**Point 1**	**Point 2**	**Point 3**
M2	0.755	0.800	0.559
N2	0.157	0.167	0.118
K1	0.063	0.067	0.046
S2	0.147	0.157	0.112
O1	0.045	0.051	0.036
M4	0.125	0.154	0.103
M6	0.054	0.053	0.037

Based on the derived constituents, the tidal stage and current velocity for an entire year are forecasted with an hour time step for each point. The current velocity magnitudes are utilised to calculate a time series of the available kinetic power density by

$$p_{kinetic} = \frac{1}{2}\rho \left|\overrightarrow{V(t)}\right|^3 \qquad (4.6)$$

where $\left|\overrightarrow{V(t)}\right|$ is the depth averaged current velocity magnitude for time t. From such time series, histograms of the depth averaged velocity magnitudes and power density are produced for each point and are shown in Figure 4.16. The most occurring or most probable depth averaged velocity is between 0.5-0.6 m/s around the 'hot-spot' site. The most likely power density is shown to be the lowest bin with power densities under 20 W/m^2. This is a result of slack or diminishing ebb and flood tides dominating the 12-hour tidal cycle.

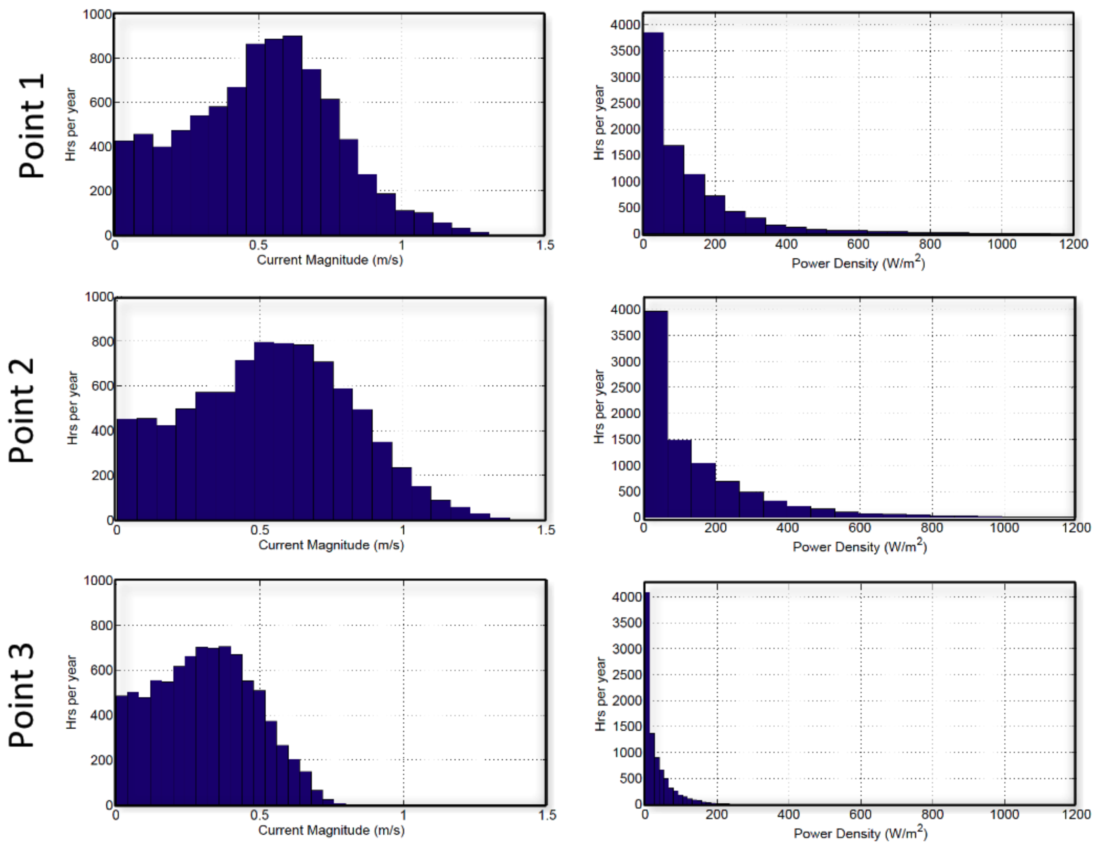

Figure 4.16: Histograms of depth averaged current velocity magnitudes and power density at points 1, 2, and 3 computed using harmonic analysis of the modified model data

To provide a better idea of the energy available for the Girl Scout camp on Rose Dhu Island, a number of assumptions may be applied and the time-series of power can be integrated over time to give a total energy for the year. The power (P_k) can be calculated as

$$P_k = \frac{1}{2}\rho \left|\overrightarrow{V(t)}\right|^3 E_f A_s \tag{4.7}$$

where E_f is the efficiency and A_s is the swept area. For this analysis a total swept area of 10 m^2 and a conservative efficiency of 45% is chosen based on 50% device efficiency and 90% mechanical to electrical efficiency. Additionally, a cut in speed of 0.5 m/s is also selected where all power below that speed is zero. For simplicity the calculations are performed using the total depth-averaged velocities rather than the velocity components in the axial direction. Moreover, this also allows for assessment of available energy independent of the turbine technology because unlike the horizontal-axis turbines which are mainly designed based on velocity components in the axial direction, vertical-axis turbines can function independently of the flow direction.

The time series of the power produced under these conditions at point 2 on transect A is shown in the top panel of Figure 4.17. It is shown that the peak power is over 4 kW during spring tides, but only 1 kW during neap tides. The cumulative power or energy for a full year is found by integrating the power time series over the entire year and is approximately 5400 kW hrs. Although this may seem like a fairly low amount of energy, especially compared to utility scale projects, this is the order of magnitude of energy desired for the Girl Scouts. It should be noted however that the above assessment is conservative and provides only the “theoretically” available kinetic power as the calculations were made based on the assumption that flow is undisturbed and predominantly is along the axial direction. In reality the presence of turbines would alter the flow hydrodynamics and kinetic power flow calculations.

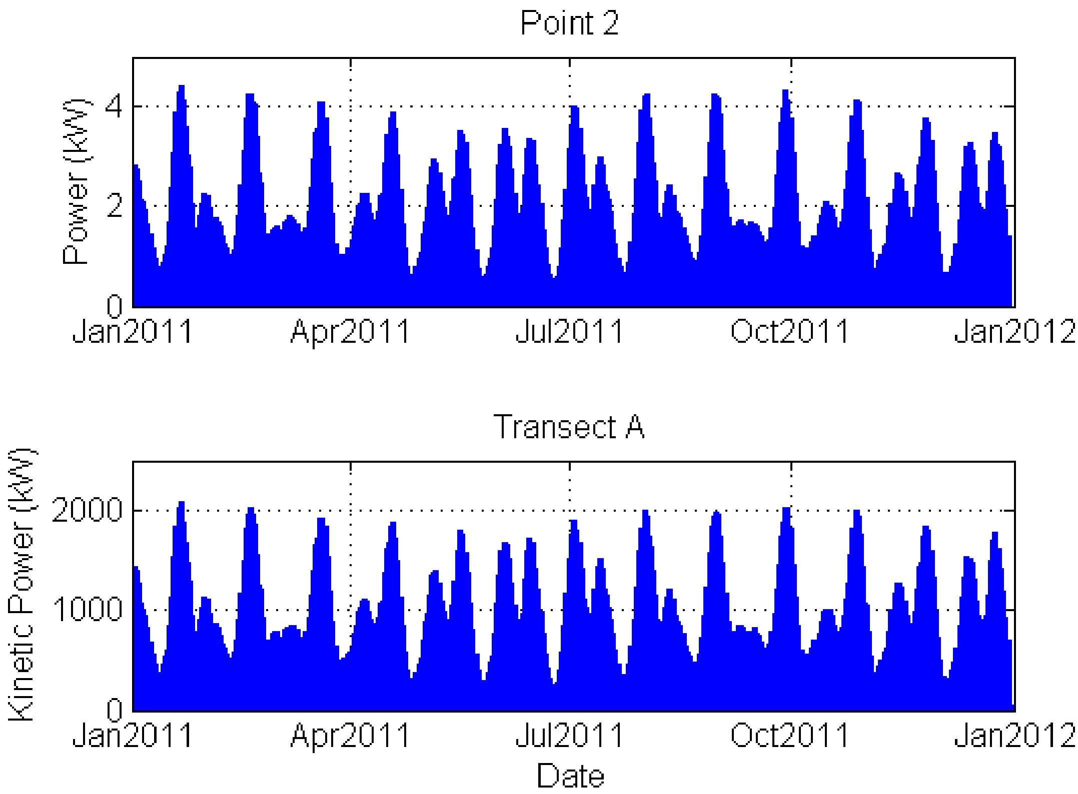

Figure 4.17: Time series of (top) the predicted power for point 2 and (bottom) total kinetic power in Transect A

A concern when extracting tidal stream energy is how much of the total energy in the flow field can be extracted while minimising impacts on the surrounding ecosystem. A preliminary assessment of this is to look at the percentage of the total kinetic power in the channel that would be extracted. In Figure 4.17, the time series of the total peak kinetic power in the full transect A is shown. The total power ranges from 500 kW during neap tides and up to 2000 kW during spring tides. The assessment above indicated a peak power extraction of around 1kW during neap tides and 4kW during spring tides. This is a very small fraction of the total power (0.2%) and would presumably have little impact on the hydrodynamics of the ecosystem as past studies have suggested that significant impact factor values range between 15-30%.

Another and perhaps better indicator of total available energy is to use the method of Garrett and Cummins (2005) to determine upper limit for maximum extraction of tidal stream energy. This simplified method considers both the kinetic and potential power with the exclusion of any technology specific assumptions is applied. The details of the method is outlined by Garrett and Cummins (2005). The method uses the undisturbed flow field from the model with simple analytical methods assuming that the full cross-section is filled with tidal energy devices. Considering a constricted channel connecting two large bodies of water in which the tides at both ends are assumed to be unaffected by the currents through the channel, a general formula gives the maximum average power as between 20 and 24% of the peak tidal pressure head times the peak of the undisturbed mass flux through the channel. This maximum average power is independent of the location of the turbine fences along the channel. Maximum average tidal stream power, P_{max}, is given as

$$P_{max} = \gamma \cdot \rho \cdot g \cdot a \cdot Q_{max} \tag{4.8}$$

where γ is a parameter dependent on the dynamic balance of the flux and waterlevel, a is the amplitude of the tidal water level constituent and Q_{max} is the maximum corresponding tidal flow rate. For a background friction dominated, nonsinusoidal (i.e. considering more than one tidal constituent) case, if data for the head and flux in the natural state are available, the maximum average power may be estimated with an accuracy of 10% using $\gamma = 0.22$, without any need to understand the basic dynamical balance (Garrett and Cummins, 2005). A multiplying factor is used to account for additional constituents (a_1, a_2, ...) given as

$1 + \left(\frac{9}{16}\right)(r_1^2 + r_2^2 + \cdots)$, where $r_1 = \frac{a_1}{a}, r_2 = \frac{a_2}{a}$ ...

This upper bound on the available power ignores losses associated with turbine operation and assumes that turbines are deployed in uniform fences, with all the water passing through the turbines at each fence. Using this method the total available power for transect A is computed as 4.75MW. Similarly, an extraction of up to 4kW of power is an extremely small portion of the total available power, indicating that this level of extraction would have minimal physical impacts.

Overall, the above assessment indicates that tidal stream energy is a viable option for renewable energy for the Girl Scouts on Rose Dhu Island. Although the calculated total power available in the tidal streams is 4.75MW, it should be noted that this value is the "theoretically" available maximum power. The total power will be significantly different to the "theoretically" available power after the inclusion of turbine device losses and consideration of all other practical constraints. Therefore further investigation, which however is beyond the scope of this study, is needed to quantify the available power in reality from tidal streams near Rose Dhu Island.

4.5 Investigation of tidal asymmetry in the Ogeechee Estuary

The recent study of Neil et al. (2014) highlighted that while there are several physical, socio-economic and environmental constraints that are considered in selection of sites for tidal energy projects, an important factor that is not routinely considered despite its importance in quantifying the resource, is tidal asymmetry. Their study showed that a 30% asymmetry in velocity can translate into a 100% asymmetry in tidal power density. With such direct implications to the available tidal stream energy it is important for resource assessment studies to accurately predict and understand the factors contributing towards tidal asymmetry. Therefore in the present study additional simulations are performed to investigate tidal asymmetry in the Ogeechee Estuary in view of assisting future resource assessment studies. However as the model results in section 4.4 showed under-prediction of current speeds, the computational setup is slightly modified to enhance the accuracy of model. Details of the modified computational setup and list of simulations related to tidal asymmetry are presented in the following section.

4.5.1 Modifications to computational setup

The computational domain of the model slightly differs from the previous simulations, with the boundary being extended further inland to provide a better representation of the smaller creeks upstream of Little Ogeechee River as indicated by dotted lines in Figure 4.18. This is performed to accurately represent the volume flux of water entering and exiting the computational domain and thereby enhance the tidal currents which have been under-predicted previously.

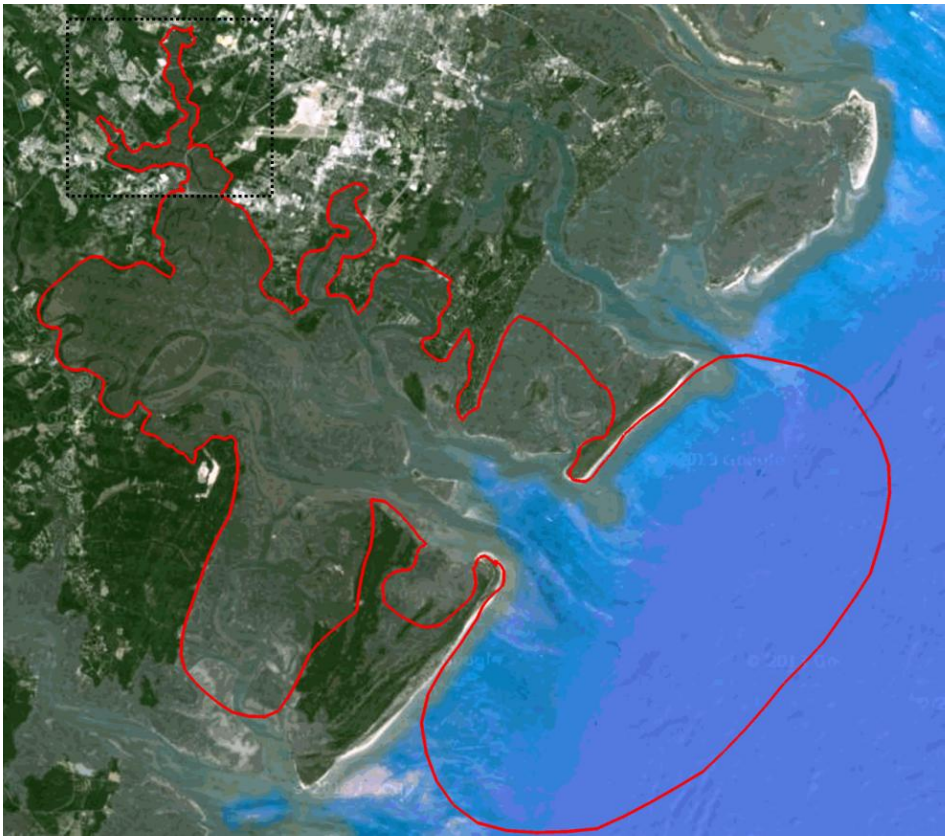

Figure 4.18: Modified computational domain. The area enclosed in black dotted lines shows the boundary extension made to better represent the smaller creeks upstream of the Little Ogeechee River

The numerical grid employed is finer than the previous simulations in both the horizontal (by a factor 1.5) and vertical directions (by a factor of 2.0). The bathymetric data used to calculate mean water depth in the main channels is similar to before;

however, wetland elevations were mapped using 2009 LIDAR elevation data published from NOAA and Savannah Area Geographic Information System in 2012, unlike the NWI data used in the previous simulations. A second computational grid is also created based on wetland elevations from the NWI to observe the effect of marsh elevation on tidal asymmetry as NWI data over predicted wetland elevation in the upper estuary by approximately 0.7m. The numerical model simulations are performed over a period of 45 days (November 16 to December 29, 2011) so that it covers the period during which detailed field measurements were performed (detailed in Section 4.2).

The model is validated for a control case which is referred to as Simulation A1 and for which measurement data is available. Other simulations, whose parameters along with A1 are presented in Table 4.4, include varying: marsh elevations (B1); overall frictional coefficients, f_b (B2, B3); and varying degrees of enhanced frictional coefficients in the wetlands, f_m (A2, A3). The model simulations are compared with each other and measurements to accurately describe the tidal asymmetry of the Ogeechee Estuary and the sensitivity of its hydrodynamics to these parameters; highlighting the importance of their accuracy.

Table 4.4: List of simulations and model parameters

	Simulation Name	**Model Parameters**			
		Marsh Elevation [m] z_m	f_b	f_m	$\frac{f_m}{f_b}$
Increasing Marsh Elevation ↓	A1	0.3	0.0025	0.025	10
	B1	1.0	0.0025	0.025	10
Decreasing Marsh Friction ↓	A3	0.3	0.0025	0.05	20
	A2	0.3	0.0025	0.0025	1
Increasing Domain Friction ↓	B3	0.3	0.01	0.01	1
	B2	0.3	0.02	0.02	1

4.5.2 Hydrodynamics: Model-predicted vs. measured comparisons

In this section, water surface heights relative to the MTL, η_t, and volume fluxes, Q, for the measured transect A and numerical model simulations are calculated and compared. Channel volume fluxes rather than localized current velocities, are compared due to the high variability of cross channel velocities induced by bathymetry and channel curvature. The volume flux Q is calculated, for both field and model output as

$$Q = \sum_{n=1}^{N} \bar{a}_n w_n h_n \tag{4.9}$$

where N represents the total number of data points along the transect, w_n is the distance along the transect measured between the centers of line connecting two adjacent data points, h_n is the depth, and $\bar{a}_n$ is the depth averaged velocity component in the axial direction. The sign convention for Q is positive for axial flow directed in the flood direction (to the northwest) and negative for axial flow directed in the ebb direction (to the southeast).

Water level and volume flux measurements are plotted as a function of time in Figure 4.19 for both days. While water level measurements have a direct corresponding timestamp, the time assigned to Q is midway through each transect, which took on average 5 minutes to transverse. In Figure 4.19, the measurements are compared to output from Simulations A1 and B1, each having different marsh elevations, derived from the 2012 LIDAR and 1980s NWI data respectively. Visually, it can be inferred that A1 more accurately predicts the asymmetry and timing of the change in water surface heights. The RMSE values between the predicted and observed water surface heights are presented for both the simulations A1 and B1 in Table 4.5. The error is significantly higher in B1 simulation for both the measurement days. For volume flux, while timing appears to be more correct for A1, relative magnitude seems more accurate for B1. This can be confirmed through comparison of RMSE values for the predicted and observed volume fluxes also presented in Table 4.5

Table 4.5: Root mean square error values between model-predicted and observed surface heights and volume fluxes for simulations A1 and B1

RMSE	**Surface heights (m)**		**Volume fluxes (m^3/s)**	
	Nov 2011	Dec 2011	Nov 2011	Dec 2011
A1	0.12	0.26	320.7	204.1
B1	0.27	0.31	205.3	173.1

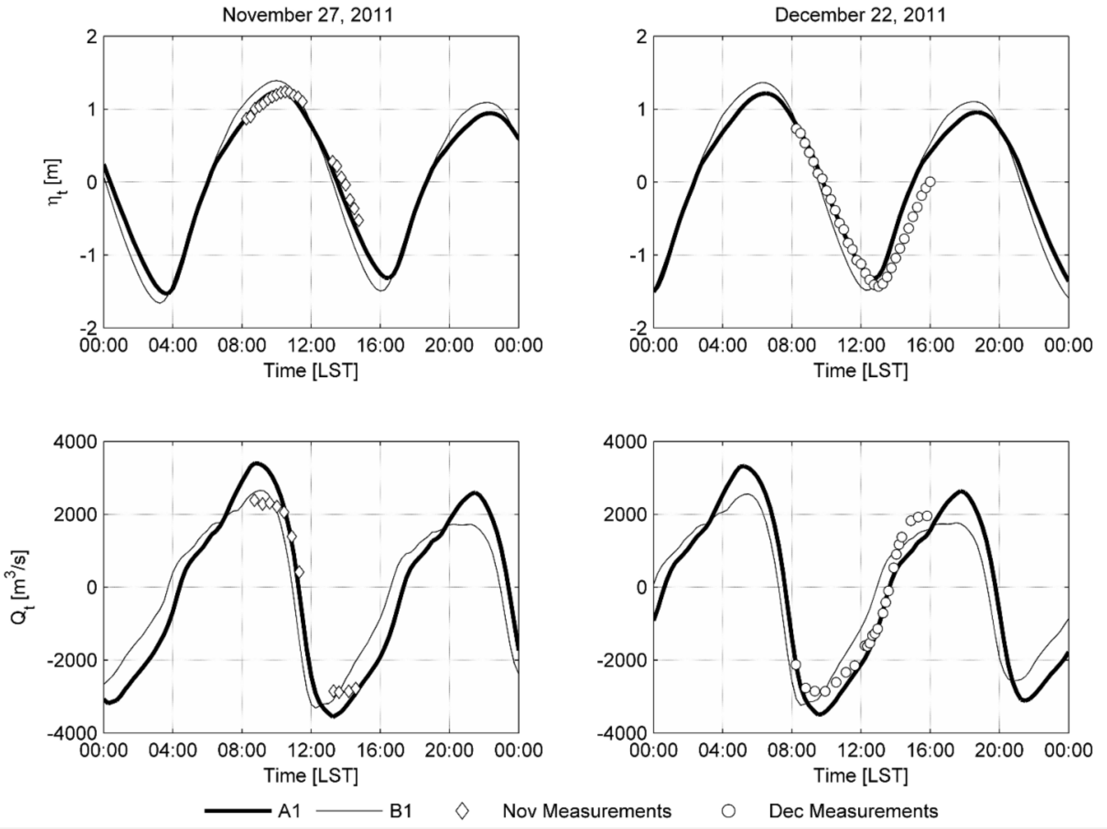

Figure 4.19: Comparisons between field measurements, Simulation A1, and Simulation B1, for water levels (top row) and volume fluxes (bottom row) for transect. Surface heights are all in MTL

Figure 4.20 highlights an inconsistency in the model and measurements that is not clearly apparent in Figure 4.19. During the rising tide in Quadrant I, the model under predicts the flood volume fluxes for a given water level, not reproducing the 'bulge' seen in the measurements. Because the measurements in that quadrant come from a singular day; it cannot be distinguished as either an anomaly or regular feature. It is hypothesized this discrepancy is due to additional non-tidal forcing in the measurements. Blanton et al. (2002) has reproduced similar tidal stage diagrams (without the bulge) through long term measurements and calculated constituents in the Charles Creek, suggesting the model is capturing the estuarine hydrodynamics correctly.

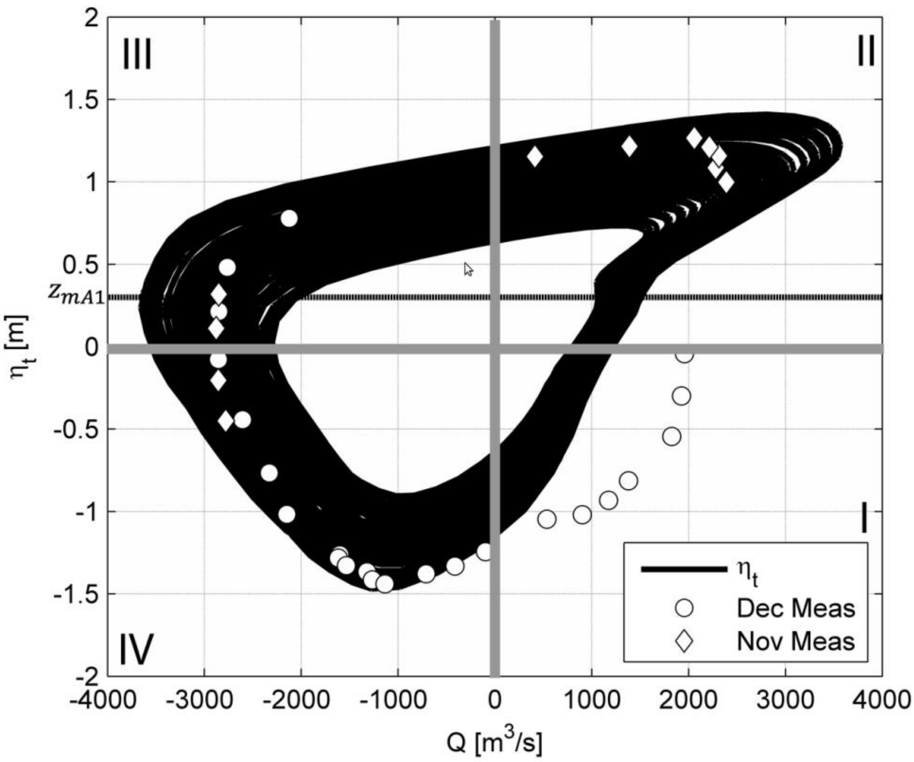

Figure 4.20: Tidal stage diagram for simulation A1 at the transect. Dashed lines represent marsh elevation z_{mA1}. All surface heights in MTL. Positive Q represents flood volume fluxes while negative Q represents ebb. Period represented: Entire duration of model simulation November 16 -December 29, 2011

4.5.2.1 Influence of intertidal storage on tidal asymmetry

To highlight the significance of relative marsh elevation to tidal stage, simulations were carried out with the same frictional parameters and channel bathymetries for two different sets of marsh elevations, simulations A1 and B1. For simulation A1, marsh elevations, z_{mA1}, are about +0.3m MTL, whereas for B1 the upper marsh elevation is approximately +1.0m MTL. As mentioned in Section 4.5.1, the different values are derived from different estuarine elevation data; A1 is from LIDAR data, and B1 is from older low resolution NWI data.

For both simulations, a representative spring tidal cycle is shown in Figure 4.21 of a) the surface heights of the open ocean boundary and measured transect; b) the relative surface height difference or pressure gradient proxy between the open ocean and transect; and c) the corresponding volume fluxes. It is important to note, both simulations share the same ocean boundary surface height since they both undergo the same tidal forcing. The corresponding tidal stage diagram is presented as well in Figure 4.22 with the identical marked timestamps.

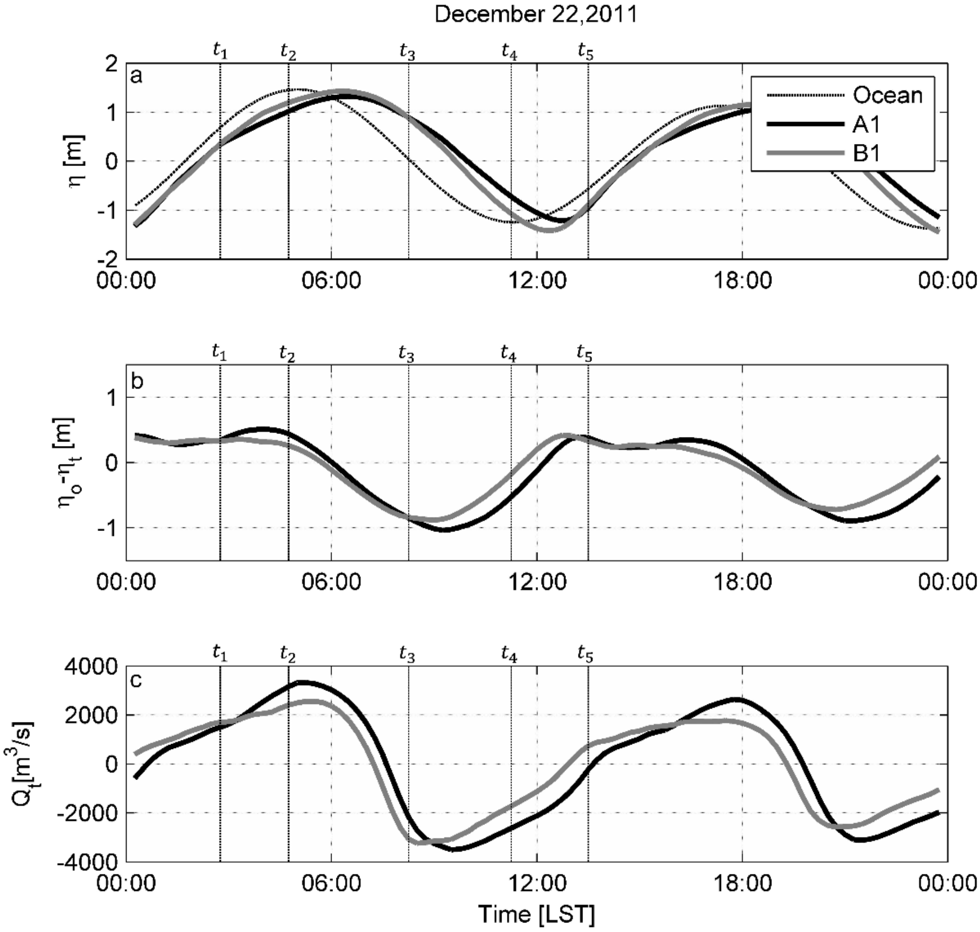

Figure 4.21: Hydrodynamic effects of change in marsh elevation: time series for Simulations A1 and B1. a) Relative surface heights in MTL, b) Relative surface height, or pressure gradient proxy, between the open ocean and transect surface heights and c) Transect volume flux for both simulations. Positive Q represents flood volume fluxes while negative Q represents ebb. Date represented: December 22, 2011. Timestamps, t_n, are reference points.

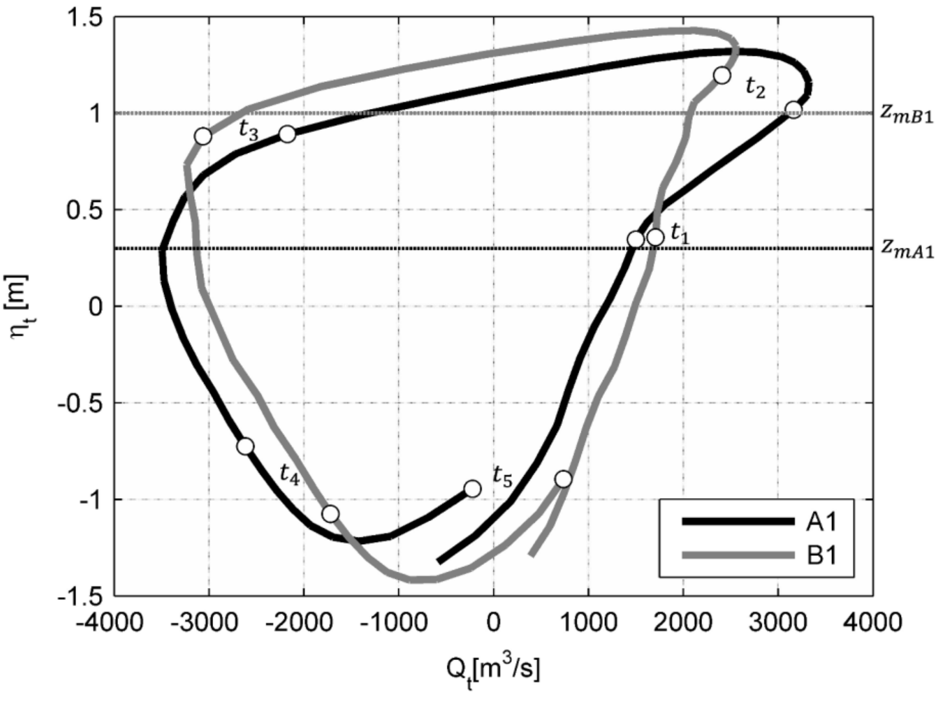

Figure 4.22: Hydrodynamic effects of change in marsh elevation: tidal stage diagrams for Simulations A1 and B1. Dashed lines represent marsh elevation for simulation. All surface heights in MTL. Positive Q represents flood volume fluxes while negative Q represents ebb. First tidal cycle of December 22, 2011 with labelled points corresponding to timestamps in Figure 4.21.

Shown in Figure 4.21a before timestamp t_1, both models have ocean and transect surface heights rising at similar rates and their difference, a proxy for pressure gradient, remains relatively constant as seen in Figure 4.21b. However, at t_1, A1 reaches the marsh elevation whereas B1 does not reach the (higher) marsh elevations until later. When the water level reaches the marsh elevation in both models, it floods the banks, and the rate of rising surface heights reduces. This results in a broader and flatter high tide for A1 (at the time t_1) and since this occurs later for the higher marsh case B1, the high tide is not as flat.

As the open ocean surface height continues to rise until t_2 and the transect water levels rise slower, there is an increase in pressure gradient in Figure 4.21b and Figure 4.21c and Figure 4.22 show the resultant surge in flood volume flux. Because the marsh flooding and resultant reduction in water level rise occurs earlier for A1, the increase in pressure gradient is much larger for that case and the flood flux is larger as shown in Figure 4.21c and Figure 4.22 prior to time t_2.

At time t_2 the ocean water level begins to fall. Because the water level for B1 is higher at this point, its floodward pressure gradient is smaller and takes less time to flip directions to be an ebb pressure gradient. Therefore, the flood flux for case B1, which is weaker anyway, flips to an ebb flux before case A1 and remains stronger, reaching a peak earlier. The net result of a later peak flood and earlier peak ebb is that the flux asymmetry is larger for the higher marsh B1.

For the higher marsh simulation B1, the shallower depth leads to a more significant difference in celerity between the marsh and the channel. At high tide, B1 has a relative marsh/channel depth ratio of 0.5/11.5 whereas A1 has 1.1/11.4. As a result, B1 has a greater phase lag difference between the marsh and channel. Thus, B1 initially has a stronger enhancement to the ebb pressure gradient causing the water level to fall faster and the ebb flux to be narrower.

At time t_4, the ocean water level begins to rise. At this point the ebbward pressure gradient, which is already weakening, diminishes quickly and flips back to flood in B1 much quicker than A1 due to its extra inclination. Again, this allows a quicker transition into flood flux for B1, giving slightly larger nascent flood volume fluxes. Interestingly, A1 actually has a longer ebb flux despite having a larger magnitude because the water level is falling much slower due to the larger storage in the marsh resulting in a larger and more persistent ebb pressure gradient in the back half of the ebb tide. The flux for case A1 does not flip to flood until time t_5, and although the pressure gradients are the same for the two cases, the flux for A1 remains smaller because of the phase lag in flipped pressure gradients, until the water level again reaches the marsh elevation and the flood pressure gradient is again enhanced for A1.

In summary, Figure 4.21 and Figure 4.22 revealed that the estuarine hydrodynamics is sensitive to a change in marsh elevation relative to MTL. The increase in marsh elevation produced narrower and shorter high tides making the system slightly more ebb-dominant. The observed differences in timing and magnitude of currents/fluxes between the two models suggest that it is very important for resource assessment studies to take into account tidal asymmetry in estuaries caused by the extensive intertidal storage.

4.5.2.2 Influence of bottom friction on tidal asymmetry

In order to observe the relative significance of friction for an estuarine system with extensive intertidal storage, simulations are carried out with various values of friction applied uniformly across the domain. Figure 4.23 and Figure 4.24 show similar plots shown in the previous section (4.5.2.1) but compares simulations A2, B3, and B2 with different bottom friction coefficients, f_b, of 0.0025; 0.01; and 0.02 respectively. In all simulations, bottom friction is uniform across the domain (i.e. $f_b = f_m$). At time t_1 there is no significant difference in water levels between the simulations in Figure 4.23a. However, in Figure 4.23c and Figure 4.24, a significant decrease in volume flux for both ebb and flood may be observed. This is not surprising as increased friction removes energy from the system. The entire tidal stage curve is shown in Figure 4.24; fluxes and surface heights shrink in amplitude. Clearly, the shallower depths at ebb tide lead to a larger reduction in ebb than flood, similar to the findings of Dronkers (1986).

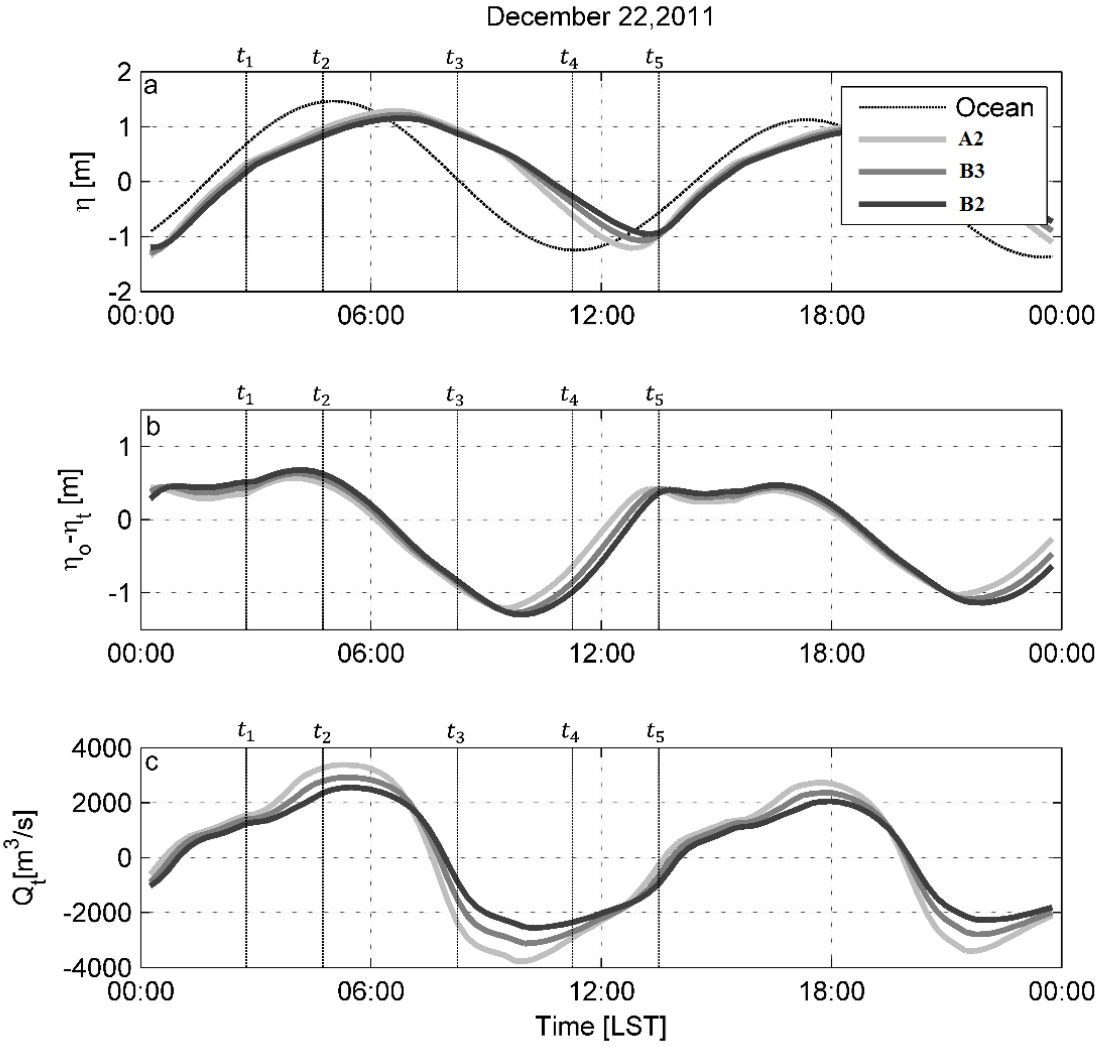

Figure 4.23: Hydrodynamic effects of change in overall friction: time series for Simulations A2, B3, and B2. Line colours are darker with increasing friction. a) Relative surface heights in MTL, b) Relative surface height, or pressure gradient proxy, between the open ocean and transect surface heights and c) Transect volume flux for both simulations. Positive Q represents flood volume fluxes while negative Q represents ebb. Date represented: December 22, 2011. Timestamps, t_n , are reference points.

After t_3 there is a larger discrepancy between the water levels for the simulations shown in Figure 4.23a. As the tide drops at t_3, simulations with higher values of friction decrease at a slower rate due the slowing of wave propagation, providing a slightly larger ebbward pressure gradient shown in Figure 4.23b. Despite the increased pressure gradient forcing, the higher friction is still sufficient to reduce the overall peak ebb volume flux. However, the higher friction simulations, because of this enhanced ebb gradient, have stronger ebb flows near the end of the ebb stage near t_4.

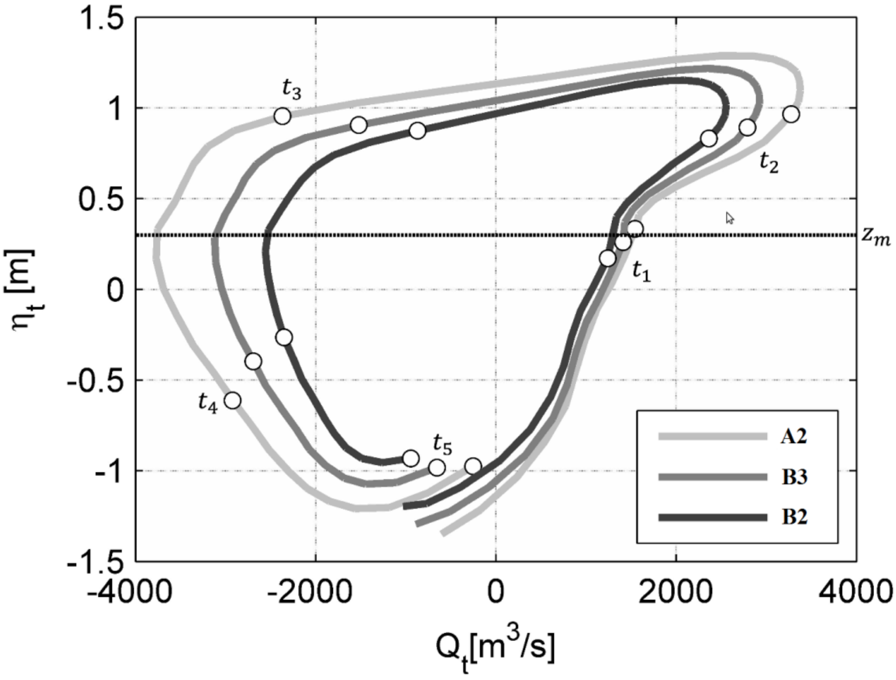

Figure 4.24: Hydrodynamic effects of change in overall friction: tidal stage diagrams for Simulations A2, B3, and B2. Line colours are darker with increasing friction. Positive Q represents flood volume fluxes while negative Q represents ebb. First tidal cycle of December 22, 2011 with labelled points corresponding to timestamps in Figure 4.23.

It was observed that an overall increase in friction induces a slightly less ebb dominated system, however to what extent varies over the domain. More significantly, higher friction results in greater energy dissipation thereby significantly reducing volume flux and surface height amplitudes. In view of further understanding the effect of friction, additional simulations are performed by increasing the bottom friction coefficient, f_m, for the marsh/wetlands to a value greater than that of the regular channel, f_b. This is done to simulate the higher flow resistance in the marsh due to denser vegetation. The effects of increasing f_m are highlighted in Figure 4.25, through the comparisons of simulations A2, A1, and A3, where f_m/f_b are 1, 10 and 20 respectively.

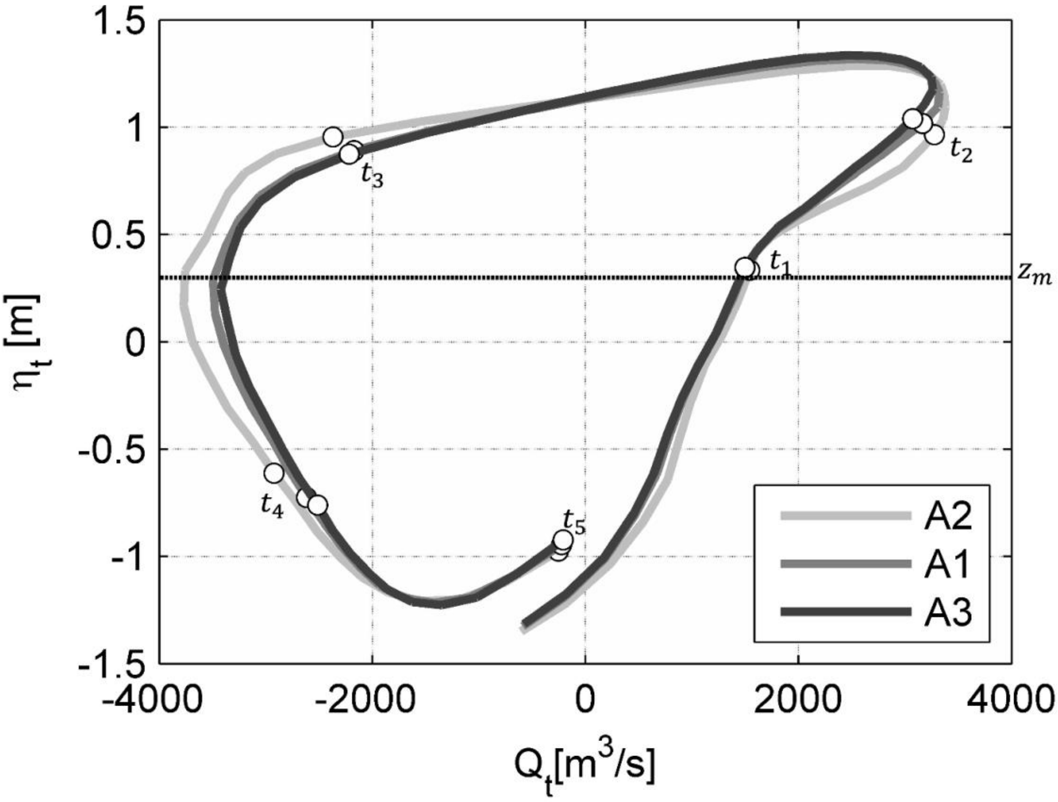

Figure 4.25: Hydrodynamic effects of change in marsh friction: tidal stage diagrams for Simulations A2, A1, and A3. Line colours are darker with increasing marsh friction. Positive Q represents flood volume fluxes while negative Q represents ebb. First tidal cycle of December 22, 2011 with labelled points corresponding to timestamps in Figure 4.23.

During the rising tide around time t_2, the water level is lower, but the volume flux is larger for the lower marsh friction case. The increased water levels yet smaller fluxes for the higher friction coefficient in the marsh are due to a reduction of flooding into the marsh in both height and lateral expanse. This impedance of flow in the marsh is further highlighted in Figure 4.26. Here, at time t_2, areas where water levels are higher for the model with enhanced friction, A3, are highlighted as compared to lower marsh friction A2.

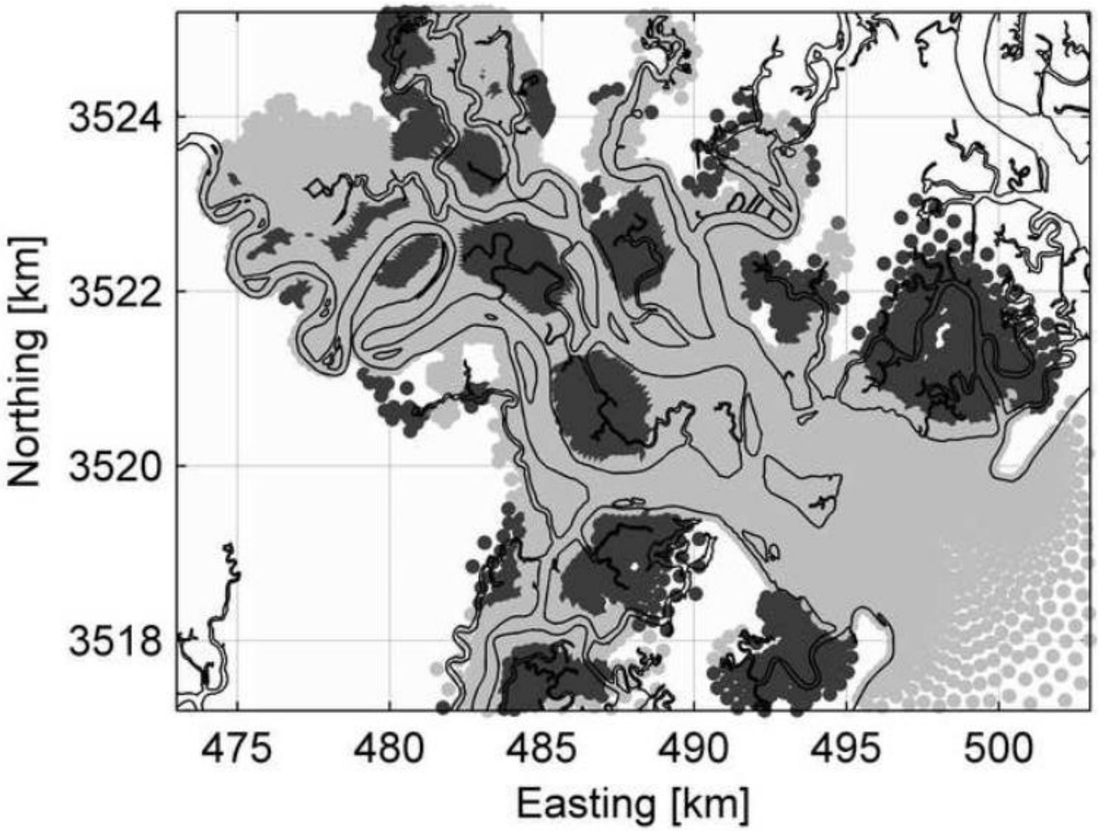

Figure 4.26: Binary map of differences in surface heights between simulations A2 and A3 at time t_2. Dark grey represents areas where water levels are higher for A2 and light grey represents areas where water levels are higher for A3

It is clear that water levels are higher in the main channels for A3, whereas A2 has higher water levels and thus further excursion and extent into the marsh and therefore more water storage. The enhanced friction results in less storage in the marsh and more water retained in the channel; therefore, the water level rises faster in the channel as shown between t_1 and t_2 in Figure 4.25. Because water levels cover a smaller area, the marsh depths are increased and there is a smaller discrepancy of marsh and channel celerity. As a result, there is less of an enhanced ebb pressure gradient resulting in a modest decrease in peak ebb flux.

Unlike bottom friction, the significant effect of enhanced marsh friction is in the reduction of the flow in the lateral, rather than axial direction. Although the enhanced marsh friction reduces ebb dominance much like bottom friction, the separate mechanisms result in different surface height profiles, resultant fluxes, and degrees of influence. Bottom friction mostly affects the magnitude of volume fluxes and surface height amplitudes, preferentially at low tide; whereas reasonable enhanced marsh friction has less effect on magnitudes, but alters distortion. Ultimately, the marshes rather than friction dictate the degree of distortion in this system due to its extremely large intertidal storage compared to channel area.

4.6 Summary

In this study, numerical simulations of tidal flow in Ogeechee Estuary, GA, USA, were carried out using the 3D Finite Volume Coastal Ocean Model. The simulations were used to quantify the flow in the tidal channels around Rose Dhu Island, GA, in order to identify hotspots of hydro-kinetic energy and to quantify the tidal stream energy potential at this site. For the validation of the numerical model, data from boat-based field measurements performed at the site were utilized. It was observed that the model-predicted velocity distributions and water surface heights agree reasonably with field measurements. The simulations revealed a tidal asymmetry in the Ogeechee Estuary with the ebb tide currents dominating over the flood tide ones. The model was able to successfully predict the distribution of the discharge into smaller creeks around Rose Dhu Island and thereby was successful in capturing the location of local hotspots of hydro-kinetic energy. An assessment of tidal stream power for Rose Dhu Island was then carried out using simulated timeseries and tidal constituents calculated through harmonic component analysis. Based on the constituents, tidal stage and current velocities were forecasted for an entire year, with which the available hydrokinetic power density at various locations was computed. It is found that local hotspots do exist near the island, and the analysis suggests a maximum available annual power of 4.75 MW. However, realistic extraction which would be sufficient for the required power demand for the Girl Scouts on Rose Dhu Island has peak powers only surpassing 4 KW during Spring tides. Because this is a small fraction of the total available resource, tidal stream energy has been determined to be a viable option for renewable energy on Rose Dhu Island with little expected impacts on the hydrodynamics.

In addition to the simulations carried out for tidal stream energy assessment at Rose Dhu Island, simulations were performed to improve the hydrodynamic predictions from the model and to further investigate tidal asymmetry in Ogeechee Estuary. It was observed that a better resolution of smaller creeks further inland of Rose Dhu Island allowed higher discharge of water in the channels and thereby improved the model-predicted fluxes in relation to field measurements. Investigation of tidal asymmetry through variation of marsh elevations and bottom friction parameters in the model revealed the significance of intertidal storage and friction in the distortion of tidal flow in the estuary. The simulations revealed that the estuarine hydrodynamics are sensitive to changes in marsh elevation relative to the mean tide level. In particular, it was found that increasing the intertidal storage by lowering marsh elevation enhances the effects on high tide and volume flux magnitudes and at the same time decreases the ebb dominance and volume flux asymmetry typically associated with the intertidal storage. Changes to bottom friction parameters in the model showed that higher friction results in greater energy dissipation resulting in significant reduction of volume flux and surface height amplitudes. Enhanced friction in marshes reduced the influence of intertidal storage on tidal distortion as higher marsh frictional coefficients laterally impede the flooding of wetlands. Overall, the simulations revealed the importance of accurate marsh elevation modelling flow in estuaries with extensive intertidal storage. The findings can be used academically to further parameterise tidal asymmetry in wetlands, or, practically to better calibrate numerical models of similar estuarine environments.

Chapter 5

Bathing water quality assessment for Swansea Bay, UK

In this chapter details of a numerical modelling study carried out towards an assessment of bathing water quality at Swansea Bay, UK are presented. Firstly, an introduction to this study including a description of site characteristics, pollution sources and the scope of the study are presented. Following this, details of field measurement data utilised in this study for model validation are provided. Next, numerical modelling details including setup, validation and discussion of the model-predicted flow hydrodynamics and faecal coliform transport characteristics in Swansea Bay are presented. Finally, the chapter concludes with a summary of the findings from this study.

5.1 Introduction

UK's Environment Agency in 2012 has estimated that approximately 10% of designated bathing waters in England and Wales are likely to fail to comply with the EU's rBWD standards. In accordance with the Directive, bathing waters which consistently fail to comply with the standards are required to put up notices prohibiting their use in order to protect public health. Since this could have huge impact on the tourist economies of nearby towns and cities along with the loss of approximately 50% of UK's current 'Blue Flag' beach awards, efforts are currently underway in many places within UK towards improving water quality at beaches and bathing water sites. In this context, the present study aims to perform assessment of faecal coliform pollution at a bathing water site in UK, namely Swansea Bay, which is under the risk of non-compliance and potential de-designation.

Located towards the northwest end of the Bristol Channel, Swansea Bay is on the South Wales coast of the UK. There are two main beaches along the bay: Swansea Beach - a 9km stretch of sandy beach from Mumbles Head to Maritime Quarters near River Tawe, and Aberavon Beach - a 5km stretch of sandy beach located in the north-eastern edge of Swansea Bay near Port Talbot. A satellite image with some of the prominent places along the bay and the Environment Agency's DSP for compliance monitoring is shown in Figure 5.1.

Figure 5.1: Satellite image of Swansea Bay showing prominent locations along the bay

Water quality at Swansea Bay is influenced by several rivers, small streams, and surface water drains which empty directly into the bay. These sources are typically affected by sewage and industrial runoff from further up the catchment and contribute towards reduced water quality in the bay especially during periods of heavy rainfall. The discharges from the small streams and drains are usually quite low ($< 1m^3/s$) but the rivers namely Tawe, Clyne, Nedd and Afan have relatively higher discharge values ($> 5m^3/s$). In addition to these sources the water quality is influenced by three offshore continuous sewage/industrial effluents that discharge pollutants directly into the bay. With many such sources of pollution contributing towards poor water quality, rating of Swansea Bay has been consistently poor with respect to the standards of rBWD and under huge risk of non-compliance.

In order to help prevent the de-designation of Swansea Bay bathing waters, extensive field measurements of faecal coliform concentrations in various polluting sources and at the Swansea Bay DSP have been carried out recently by Aberystwyth University, Wales as a part of the "Smart Coasts = Sustainable Communities" project (http://www.smartcoasts.eu/). One of the main aims of the Smart Coasts project, which this study is also a part of, is to develop and install a water quality prediction and communication system at Swansea Bay to advice the public of the bathing water quality in real-time. As there are provisions within the rBWD to discount water quality samples at bathing water sites equipped with real-time water quality prediction and communication systems, Swansea Bay bathing waters could potentially be prevented from de-designation.

The water quality prediction part of the Smart Coasts project will rely on two types of modelling systems. The first system, which is currently being used by The City and County of Swansea to predict faecal coliform concentrations at Swansea Bay DSP, was developed by Aberystwyth University. This system makes use of real-time data from meteorological and river gauging stations to predict concentrations at the DSP through empirical relationships previously derived from statistical analysis of field data. The second system, which the present study contributes towards its development, aims to predict faecal coliform levels at Swansea Bay through a hydro-environmental numerical model. Unlike the statistical model, the hydro-environmental model provides more realistic, physics-based prediction of the pollutant levels as it solves the governing equations of fluid flow and transport to simulate the flow hydrodynamics and faecal coliform transport processes in Swansea Bay. Moreover, the hydro-environmental model enables a holistic assessment of water quality in the bay as it can be used to predict water quality at several locations within the bay unlike the statistical model which currently provides predictions only at the DSP. Therefore the main objective of the present study is to setup and validate a hydro-environmental model which can accurately model the flow and transport processes and provide an assessment of bathing water quality in Swansea Bay. The scope of this study includes:

a) Conduct 3D numerical simulations of tidal flow in the Bristol Channel and Severn Estuary using FVCOM to predict flow hydrodynamics at Swansea Bay.
b) Perform a detailed analysis of flow hydrodynamics in the bay and validate the results against field measurement data.
c) Conduct 3D numerical simulations of the transport of FIO, particularly, E. coli bacteria, discharged from various sources in Swansea Bay and perform validation of model-predicted concentrations through comparisons with field measurement data.
d) Perform an assessment of the faecal coliform levels at Swansea Bay DSP and evaluate the spatial-temporal variability of FIO for the purpose of developing a real-time water quality prediction system.

5.2 Field Measurements

In order to support the numerical model, data from field measurements consisting of water levels, currents, and faecal indicator organism concentrations in Swansea Bay have been utilised in this study. The field operations were carried out by Aberystwyth University as a part of the Smart Coasts project and are described below in detail.

5.2.1 Flow measurements

Measurements of the flow hydrodynamics in Swansea Bay were carried out through drogue releases and Acoustic Doppler Profiler (ADP) deployments at several locations within the bay. Figure 5.2 shows an example of the release of a drogue and ADP deployment at one of the locations.

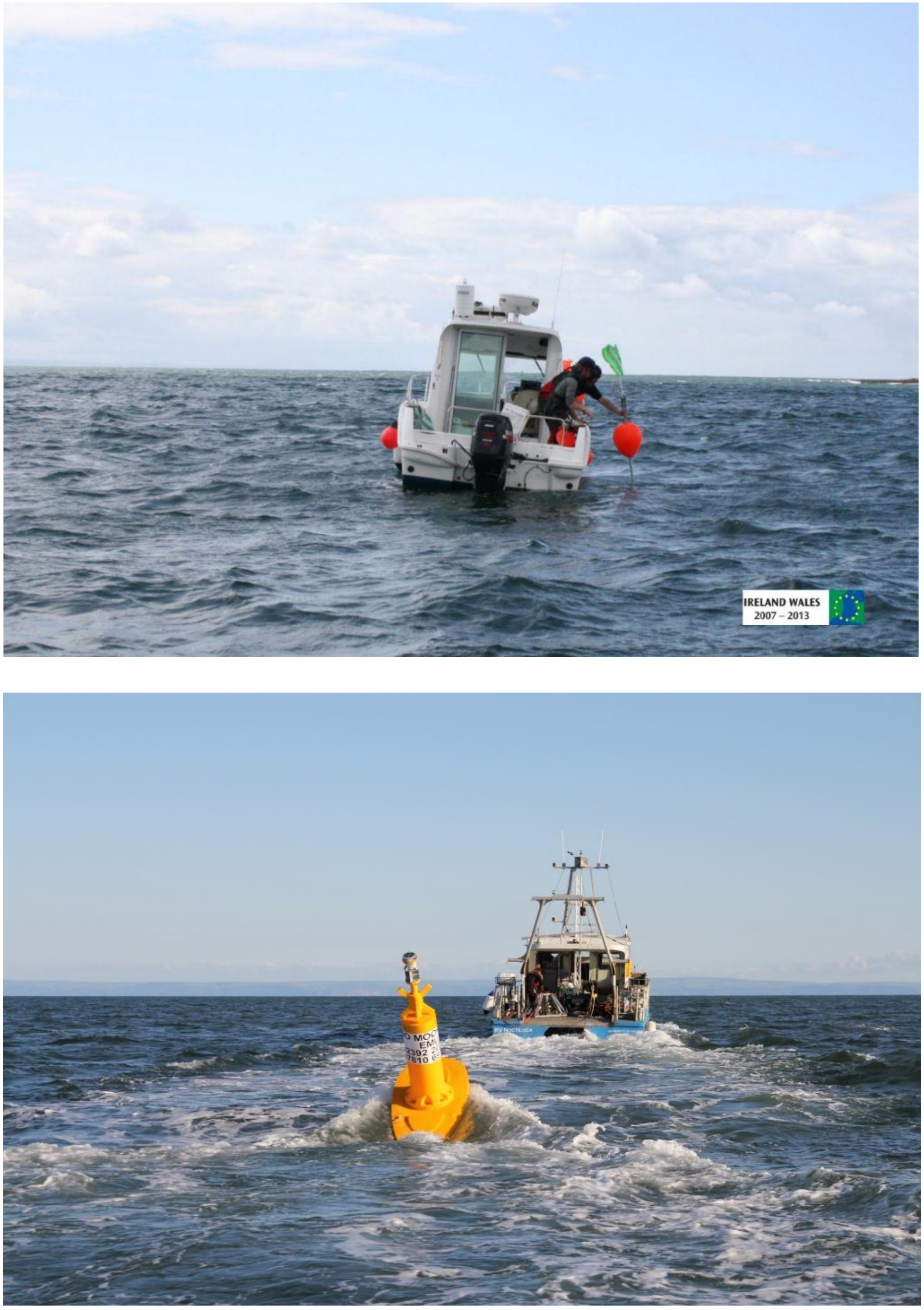

Figure 5.2: Top panel - Release of a drogue as a part of field measurements, Bottom panel – ADP deployment in the field.

Five drogues were released at different locations to capture the general flow patterns within the bay. At each of these locations, two sets of drogues at 1m and 2m sail depth were released and their positions were tracked using GPS recordings. An overview of the drogue tracks recorded in Swansea Bay is presented in Figure 5.3.

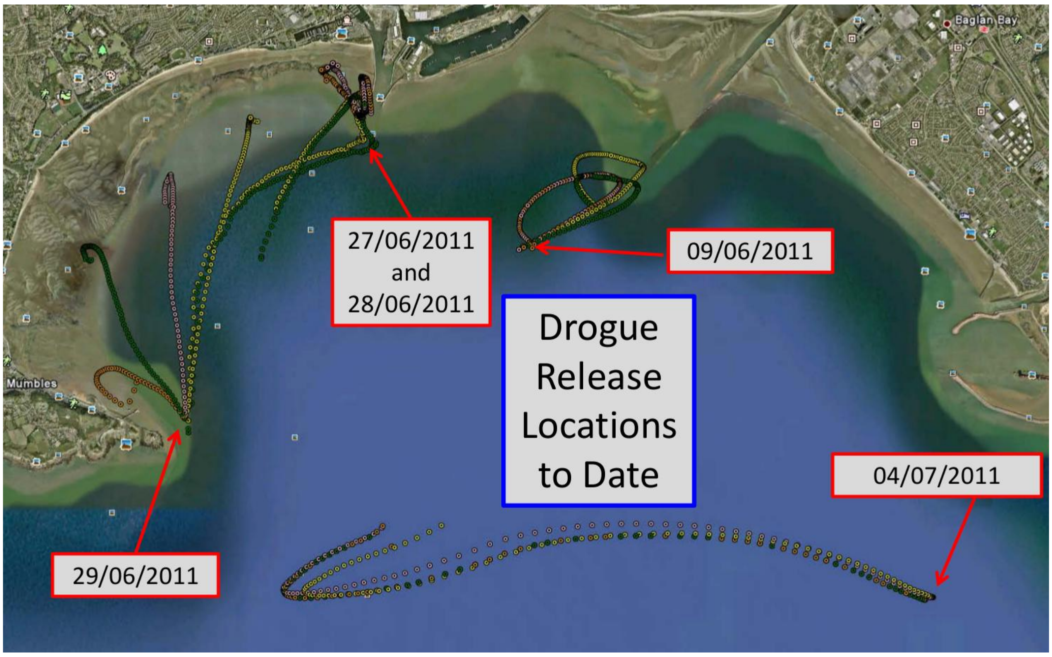

Figure 5.3: Summary of the release locations and drogue movements observed in Swansea bay. Yellow and Green symbols correspond to drogues released at a vertical depth of 1m below the water surface, Pink and Orange symbols correspond to drogues released at a vertical depth of 2m below the water surface.

The deployment of a seabed frame mounted Aquapro ADP was carried out at five offshore locations shown in Figure 5.4. The measurement of tidal water levels and currents at these locations were carried out through two deployments. Deployment 1, which was based on Aquapro 600kHz ADP, was placed at locations 2 and 5 for a period of three weeks between July and August 2012. Deployment 2, which was based on Aquapro 1MHz ADP, was placed at locations 1, 3, and 4 for a period of three weeks between September and October 2012. The ADPs were configured to acquire a water level record and current profile every 10 minutes over an averaging period of 60 seconds. A statistical summary of the water levels and current measurements for all five locations is presented in Table 5.1 and Table 5.2 respectively.

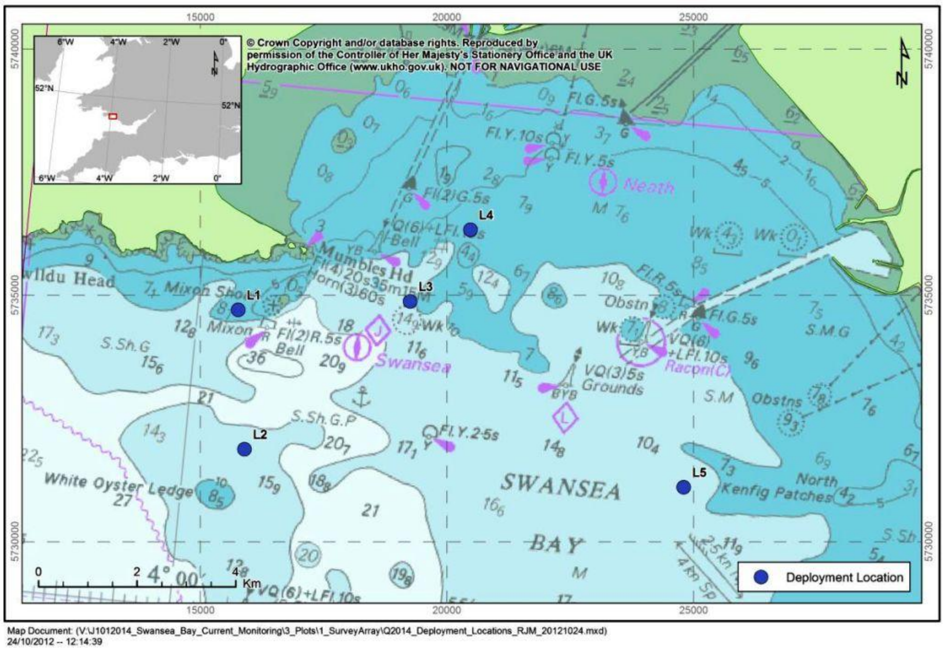

Figure 5.4: Five locations where model data is compared against field data from ADP deployments.

Table 5.1: Water level statistics from each location

Astronomical Statistics	Location				
	L1	L2	L3	L4	L5
Highest Astronomical Tide, HAT (m)	10.464	10.524	10.594	10.604	10.709
Mean High Water Spring, MHWS (m)	9.412	9.368	9.455	9.483	9.470
Mean High Water Neap, MHWN (m)	7.194	7.142	7.203	7.225	7.192
Mean Sea Level, MSL (m)	5.208	5.140	5.187	5.205	5.150
Mean Low Water Neap, MLWN (m)	3.222	3.138	3.171	3.185	3.108
Mean Low Water Spring MLWS (m)	1.004	0.912	0.919	0.927	0.830
Lowest Astronomical Tide, LAT (m)	0.000	0.000	0.000	0.000	0.000

Table 5.2: Depth-averaged current speed statistics from each location

Astronomical Statistics	Location				
	L1	L2	L3	L4	L5
Metonic Maximum Speed (m/s)	1.126	1.336	1.009	0.801	0.792
Mean Spring Rate (m/s)	0.936	1.065	0.804	0.653	0.619
Mean Neap Rate (m/s)	0.494	0.520	0.397	0.320	0.295
Bearing (+180º) (ºT)	89.7	76.9	51.3	46.4	85.7

The collected data was processed further to produce time-series plots of water levels, current speeds and current direction. Figure 5.5 shows an example of the time-series of water levels and contours of current profiles obtained from measurements at location 2.

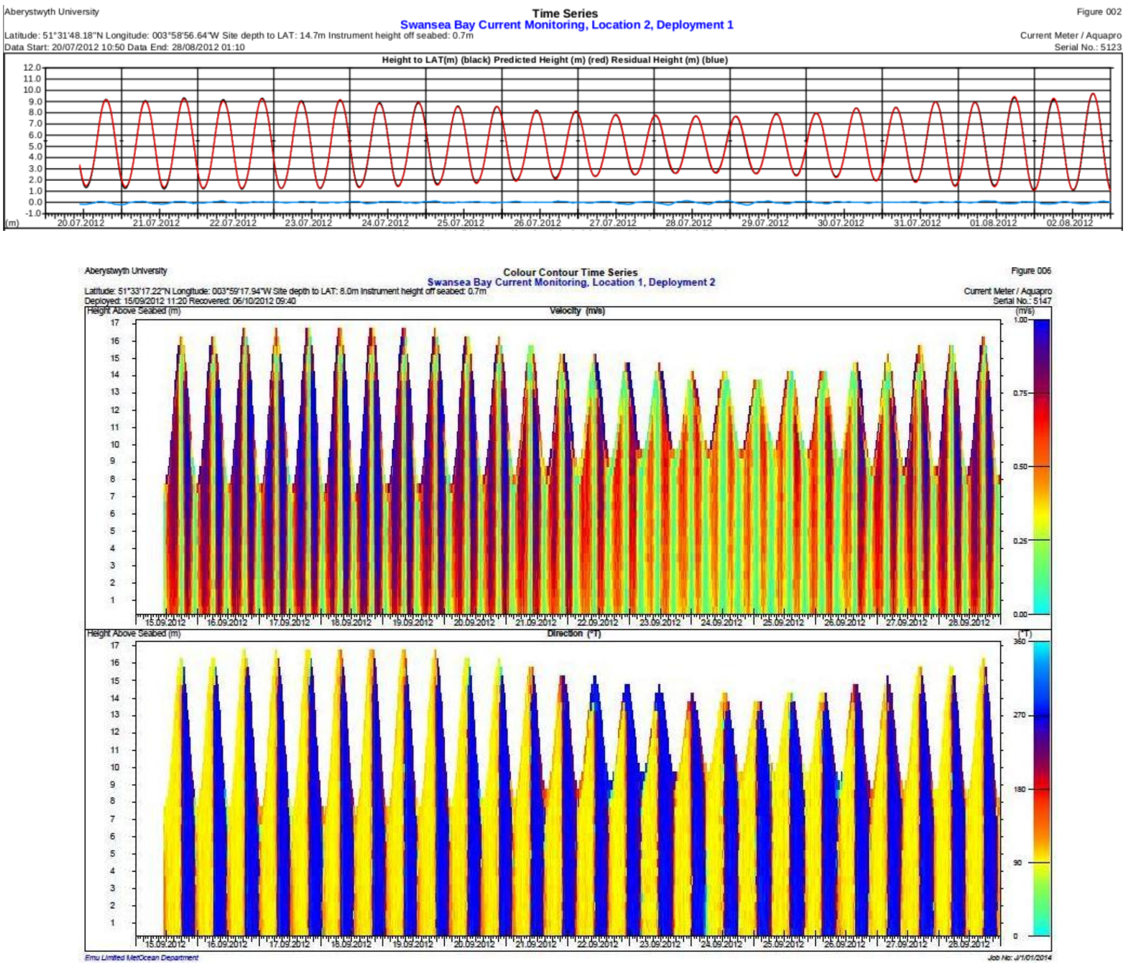

Figure 5.5: Top panel- time-series of water levels obtained from measurements, Bottom panel- contours of current profiles obtained from measurements.

5.2.2 Faecal Indicator Organism Concentration Measurements

Measurements of discharges and FIO concentrations for several pollution sources entering the bay were carried out to provide information to the numerical model. These sources included six rivers, twelve streams, four surface water outlets and three offshore sewage/industrial effluents. Figure 5.6 shows the location of some of these major pollution sources. Also shown in the figure are locations of three offshore sites: Site 1, 2, and 3 where hourly water samples have been collected on a selected day (November 15th, 2012) for validation of numerical model predicted FIO concentrations.

Figure 5.6: Red and black dots show locations of major pollution sources in Swansea Bay. Sites 1 to 3 are the locations where field data of FIO concentrations is available for model validation.

In addition, intensive field sampling operations were conducted at DSP to analyse the FIO concentrations at the bay and to compare with numerical model predictions. The water samples were collected at half-hourly intervals between 07:00 GMT and 16:00 GMT during three days of each week (typically Monday-Wednesday) throughout the 20 week bathing season in 2011 (16/05/2011 to 28/09/2011). In total the field data consisted of information from over 60 sampling days, each with 19 water quality samples.

5.3 Numerical modelling details

Details of the numerical model setup including the computational domain, numerical grid, bathymetry, boundary conditions and FVCOM model parameters are presented below.

5.3.1 Computational Domain

Although the focus of the present study is on Swansea Bay, the computational domain in the model is extended to include regions of the Bristol Channel and the Severn Estuary in order to minimise the effect of boundary conditions. Figure 5.7 shows the computational domain along with a satellite image on the background. The Swansea Bay region is indicated in the figure by a black box.

Figure 5.7: Computational domain of the present study.

Since the coastline data (from NOAA) used for the generation of the computational domain was not detailed enough to accurately represent the geometric features of Swansea Bay, several modifications to the coastline were performed in this study using satellite images. These modifications were mainly related to the inclusion of the rivers Tawe, Neath, and Afan which are some of the major sources of pollution in the bay. Figure 5.8 shows as an example of the computational domain before and after coastline modifications at Swansea Bay.

Figure 5.8: Top panel- computational domain before modifications to coastline geometry at Swansea Bay, Bottom panel- computational domain after modifications to coastline geometry at Swansea Bay.

5.3.2 Numerical Grid

Figure 5.9 shows the horizontal numerical grid employed in the model. At the open boundary, the grid is coarse with a horizontal grid spacing of ~600m. At Swansea

Bay, the grid is relatively fine with a spacing of approximately 25 to 75m. The number of vertical layers used in the model is 5; for a maximum water depth of 15m in the bay, this corresponds to a vertical resolution of ~3m.

Figure 5.9: The numerical grid employed in this study.

The horizontal grid spacing at Swansea Bay was determined to be optimum as several model runs with different grid resolutions produced similar results. Figure 5.10a and Figure 5.10b present as an example two numerical grids tested in this study with an average spacing of 50m (the grid used in this study) and 25m respectively in Swansea Bay.

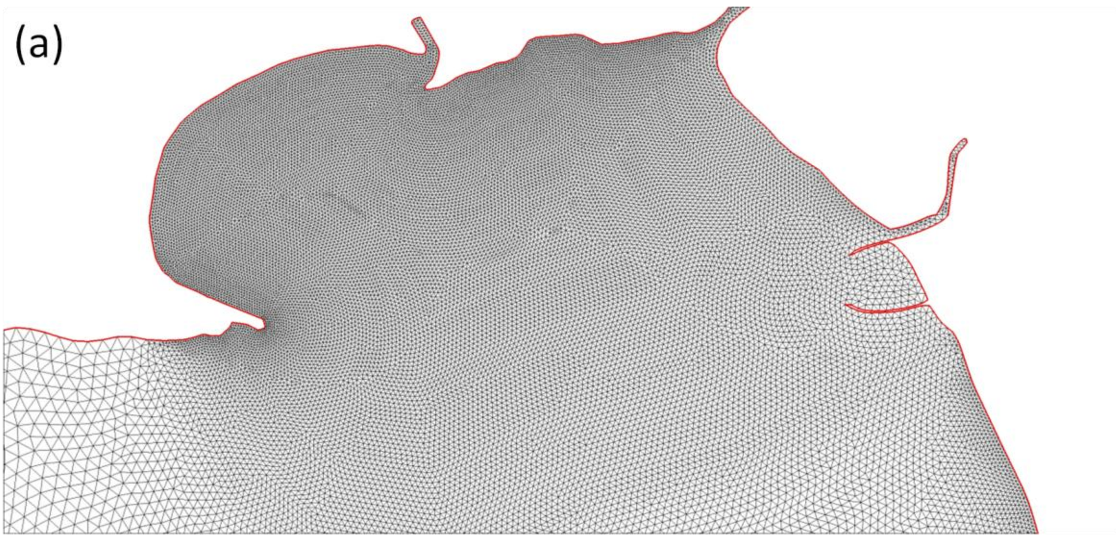

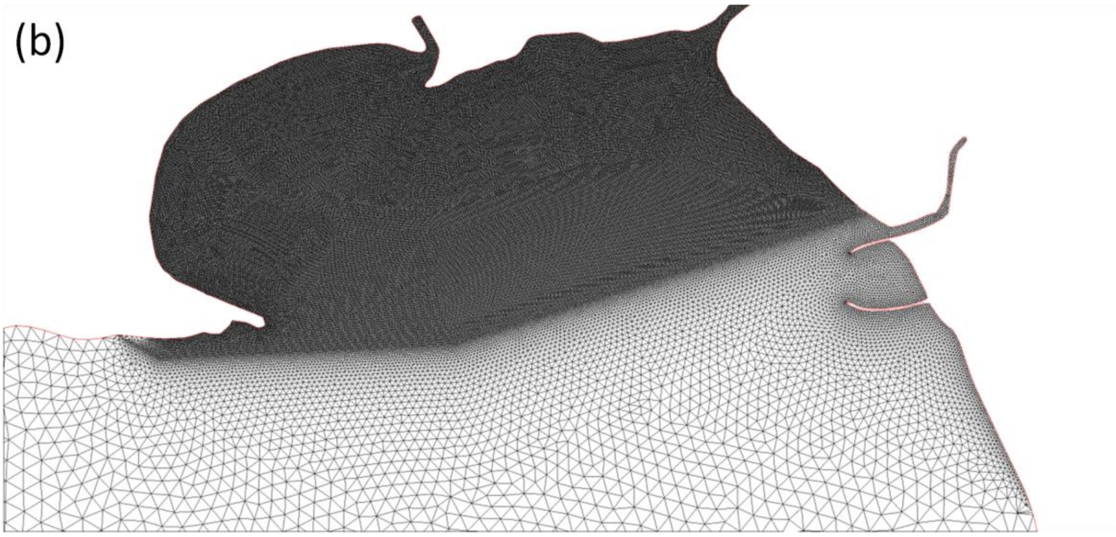

Figure 5.10: a) Numerical grid with average grid spacing of 50m in Swansea Bay, and b) Numerical grid with average grid spacing of 25m in Swansea Bay.

5.3.3 Bathymetry

Gridded bathymetry data at a uniform spatial resolution of 200m was obtained from Sea Zone (http://www.seazone.com/marine-maps/type/bathymetry-data) and additional data was extracted manually from the Swansea Bay Admiralty Chart (number: 1161). Figure 5.11 shows the contours of mean water depth obtained after interpolation of bathymetry data on to the computational domain.

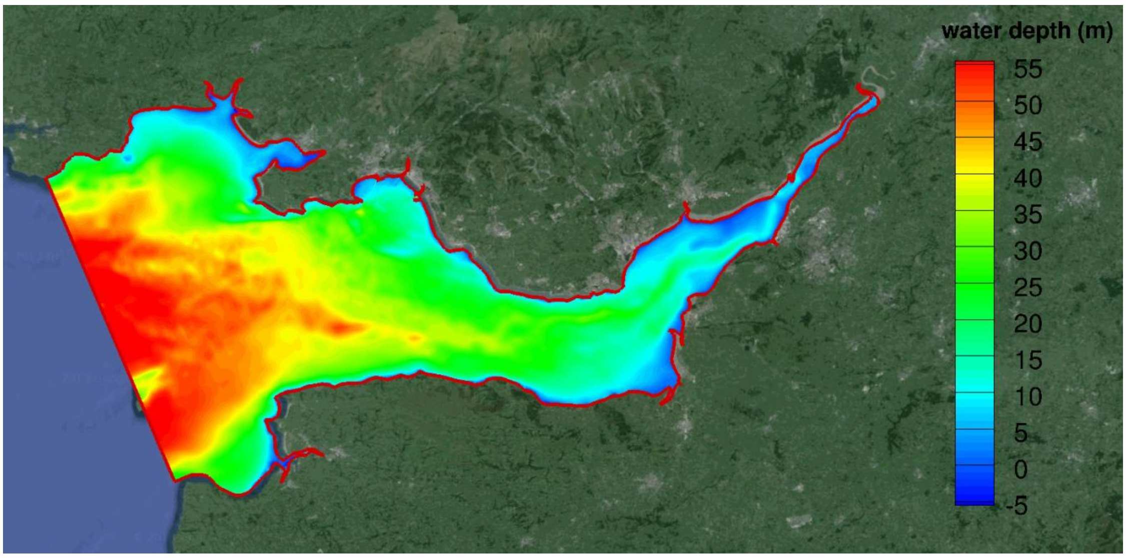

Figure 5.11: The contours of mean water depth in the entire computational domain.

5.3.4 Boundary conditions

The computational model is driven by tidal water level forcing at the seaward open boundary using the data obtained from National Oceanography Centre. A time-series of water levels specified at the seaward boundary is shown as an example in Figure 5.12.

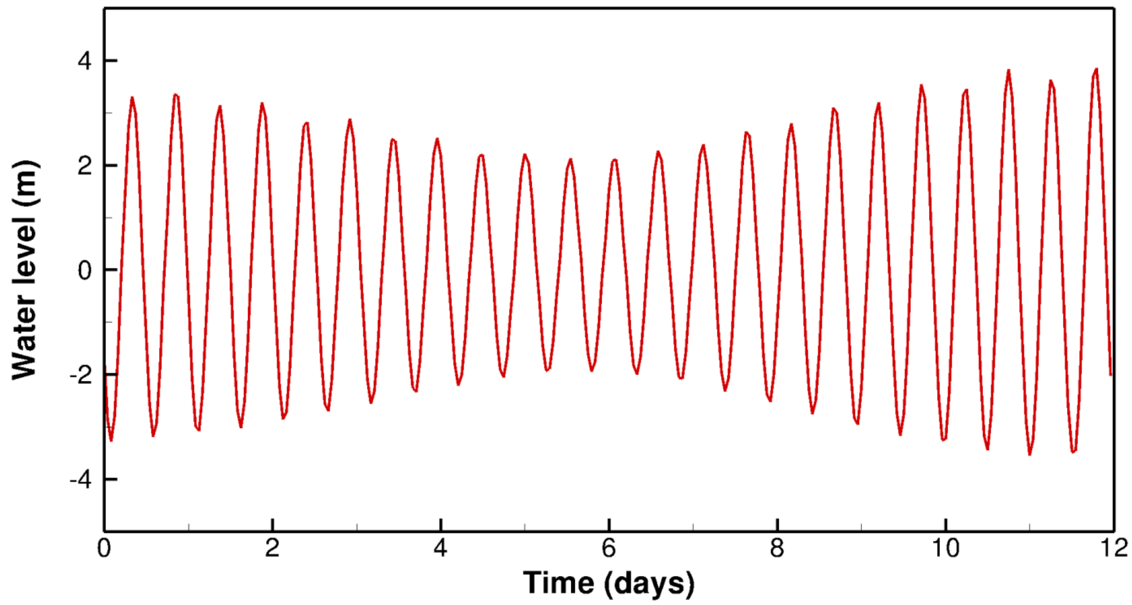

Figure 5.12: Example of water level time-series that is specified at the seaward boundary.

At Swansea Bay, time-series of discharges from various input sources such as rivers, streams, outlets and sewage effluents are specified as point-source boundary conditions. This data was obtained from Natural Resources Wales, Dŵr Cymru/Welsh Water (DCWW) and measurements from the Smart Coasts project. Time-series of FIO concentrations are specified at these input sources for modelling faecal coliforms. Table 5.3 provides a summary of discharge and FIO concentration values for all the input sources considered in this study for the time period between mid July and September 2011.

Table 5.3: Summary of discharges and FIO concentrations for all the input sources considered in this study for the time period between mid July and September 2011.

	Discharge (m^3/s)			FIO Conc. (cfu/100ml)		
	Min	Mean	Max	Min	Mean	Max
Norton Avenue	0.004	0.010	0.445	1468	5092	28937
Washinghouse Brook	0.009	0.021	0.972	5677	9125	31816
Brockhole Stream	0.005	0.014	0.161	887	3154	15995
Clyne River	0.085	0.237	7.272	1035	5965	24759
Sketty Lane Stream	0.002	0.004	0.402	31	1453	14952
University Stream	0.003	0.007	0.725	716	4141	36659
Brynmill Stream	0.015	0.036	3.820	7268	9895	34840
Patti Pavillion Short	0.002	0.005	0.569	4572	8581	46647
Tawe Barrage	2.403	11.185	195.025	1612	3670	9409
Nedd Estuary Total	1.968	10.162	170.535	836	2675	17249
Afon Afan	1.339	4.635	68.864	482	1385	3689
Ffrwd Wyllt	0.160	0.822	5.478	636	1240	3001
Abbey Beach Culvert	0.063	0.323	2.150	177	1975	7216
Swansea STW FE+SSO	0.002	0.517	1.471	38390	231538	2415463
Afan STW FE	0.217	0.700	1.106	171333	195129	222175
Tata FE	0.000	0.551	1.234	0	366	372
Port Tawe	0.000	0.024	3.769	0	15704	955820
Knab Rock SPS	0.000	0.006	0.747	0	955	25701
CSO 401 Mumbles	0.000	0.000	0.192	0	11983	680237
Baldwins SPS	0.000	0.001	0.110	0	9924	52217
Queens Docks outfall	0.000	0.000	0.059	0	779	112172

5.3.5 FVCOM model parameters

The simulations are performed using the 3D version of the FVCOM model in baroclinic mode. Details of various model parameters including grid resolution, time step, friction coefficient, horizontal diffusion and vertical diffusion are presented in Table 5.4. All the parameters were selected through experimentation/model calibration and by referring to the guidance available in FVCOM manual.

Table 5.4: Swansea Bay Model Parameters

Horizontal grid resolution	25-40m at Swansea Bay ~600m at open boundary
Number of horizontal grid nodes	43528
Number of horizontal grid cells	85107
Number of vertical layers	5
External mode time step, DTE	0.25s
Ratio of external to internal model time step, ISPLIT	10
Internal mode time step, DTI	2.5s
Wet/Dry cell bottom thickness, MIN_DEPTH	0.05m
Bottom stress drag coefficient, BFRIC	0.005
Bottom roughness height, Z0B	0.001
Horizontal diffusion calculation method	Smagorinsky Formulation
Smagorinsky horizontal diffusion coefficient, HORCON	0.2
Turbulence Model	Mellor Yamada level 2.5
Background mixing coefficient, UMOL	0.0001

Several simulations with varying time periods are conducted in this study to match the time periods during which field measurements were carried out. The field measurement data consisted of drogue tracks, water level and current measurements, FIO concentration measurements at three offshore sites and intensive sampling at DSP. Table 5.5 provides a summary of the model simulations conducted in this study.

Table 5.5: List of simulations conducted in this study

Simulation purpose	Period of simulation
Comparison with four drogue releases on 29/06/2011at Mumbles Head	25/06/2011 – 30/06/2011
Comparison with four drogue releases on 28/06/2011at River Tawe	25/06/2011 – 30/06/2011
Comparison with four drogue releases on 27/06/2011at River Tawe	25/06/2011 – 30/06/2011
Comparison with four drogue releases on 09/06/2011at River Neath	05/06/2011 – 10/06/2011
Comparison with four drogue releases on 04/07/2011at River Afan	30/06/2011 – 05/07/2011
Comparison of water levels and currents with ADP deployments	15/07/2012 – 26/07/2012
Comparison of FIO (E. Coli) concentrations at three off-shore sites	05/11/2012 – 16/11/2012
Analysis of FIO concentrations at Swansea Bay designated sampling point	12/07/2011 – 29/09/2011

For all the simulations carried out in this study a ramping period of two days is considered during which the tidal forcing at the open boundary is gradually increased to its actual value in order to avoid any numerical instabilities. Due to the large extents of the computational domain (~6000 km^2) and the large number of grid cells (~90,000 horizontal grid cells*5 vertical layers) employed in the model, the simulations are carried out on a computing cluster using 128 processors. The approximate time taken for a simulation with a time period of 5 days is 2 hours.

5.4 Swansea Bay hydrodynamics

In order to understand the general flow characteristics in the Bristol Channel, contours of depth-averaged current magnitudes and current vectors are visualized in Figure 5.13 and Figure 5.14 at approximately three hours after low and high tides respectively. It can be observed from the figures that the current speeds vary significantly within the domain and the highest values are found at regions downstream of Swansea Bay near the Severn Estuary.

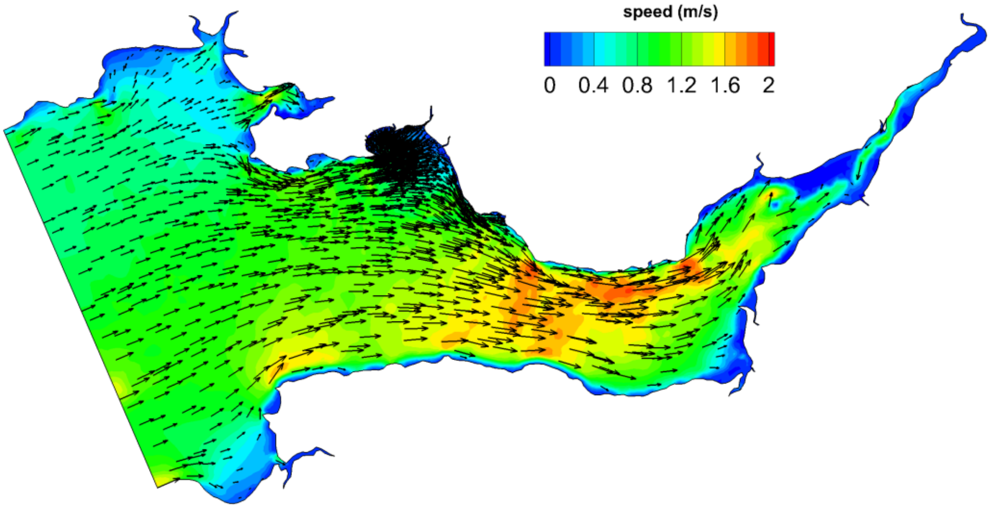

Figure 5.13: Contours and vectors of depth-averaged current speeds at approximately three hours after low tide for the entire computational domain.

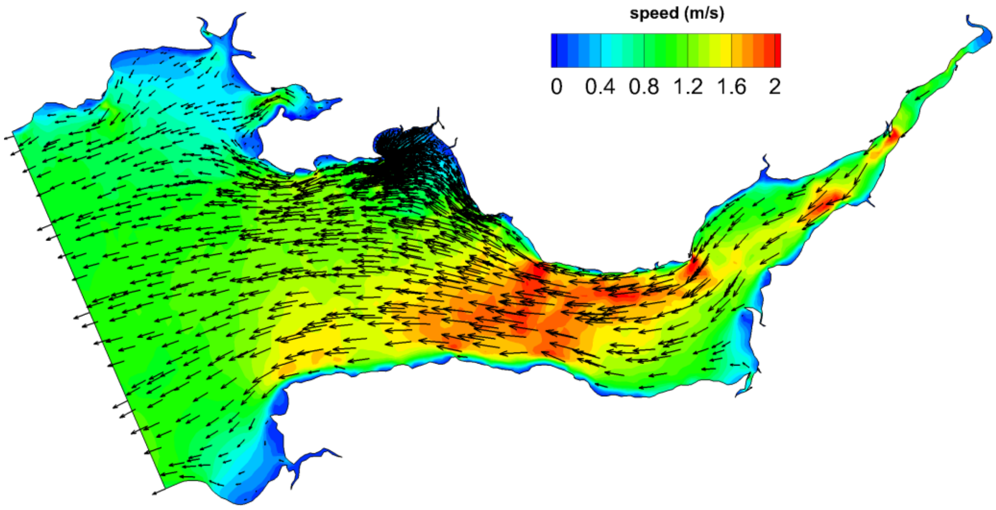

Figure 5.14: Contours and vectors of depth-averaged current speeds at approximately three hours after high tide for the entire computational domain.

In order to understand the flow characteristics in Swansea Bay region, similar plots are presented in Figure 5.15 and Figure 5.16. It can be observed from the figures that the current speeds are relatively lower within the bay in comparison to the speeds observed in the Severn Estuary. Moreover, a marked difference can be observed in the current patterns between the incoming and outgoing tides particularly because of the flow separation occurring at Mumbles Head during the incoming tide.

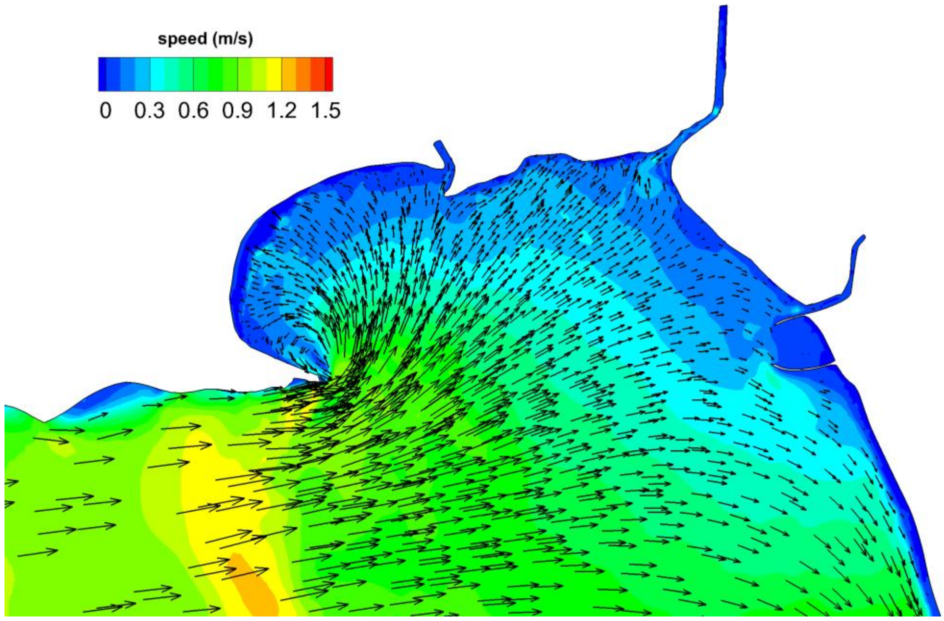

Figure 5.15: Contours and vectors of depth-averaged current speeds at approximately three hours after low tide at Swansea Bay.

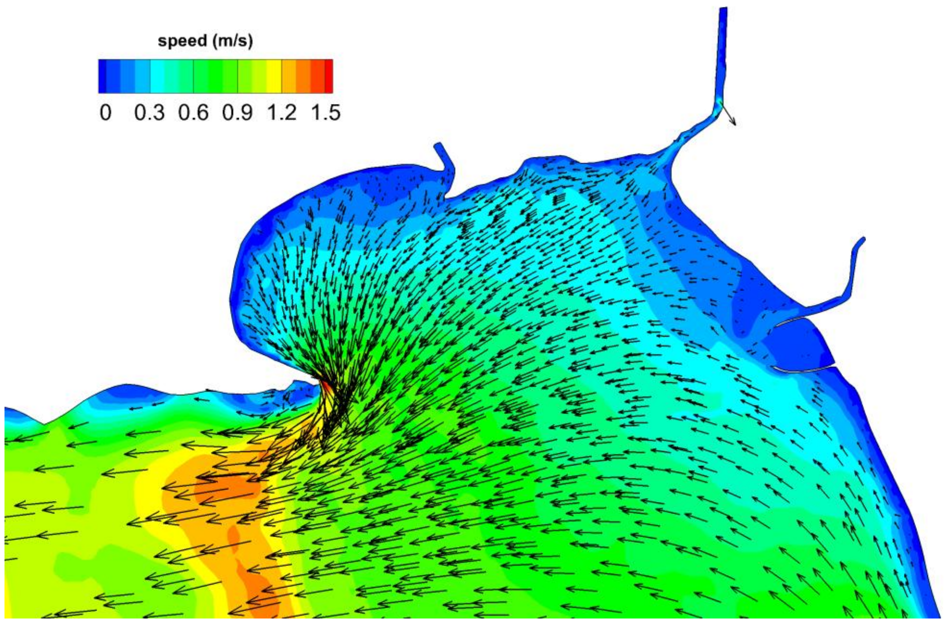

Figure 5.16: Contours and vectors of depth-averaged current speeds at approximately three hours after high tide at Swansea Bay.

In order to evaluate the accuracy of model-predicted flow hydrodynamics in Swansea Bay, comparison of simulation results against field measurements is performed as detailed in the following sections.

5.4.1 Hydrodynamics validation

For the purpose of numerical model validation, tidal water levels and currents predicted by the model are compared with field measurements at five locations (refer Figure 5.4). Figure 5.17 to Figure 5.21 present a comparison of model-predicted water levels with field measurements at the five locations.

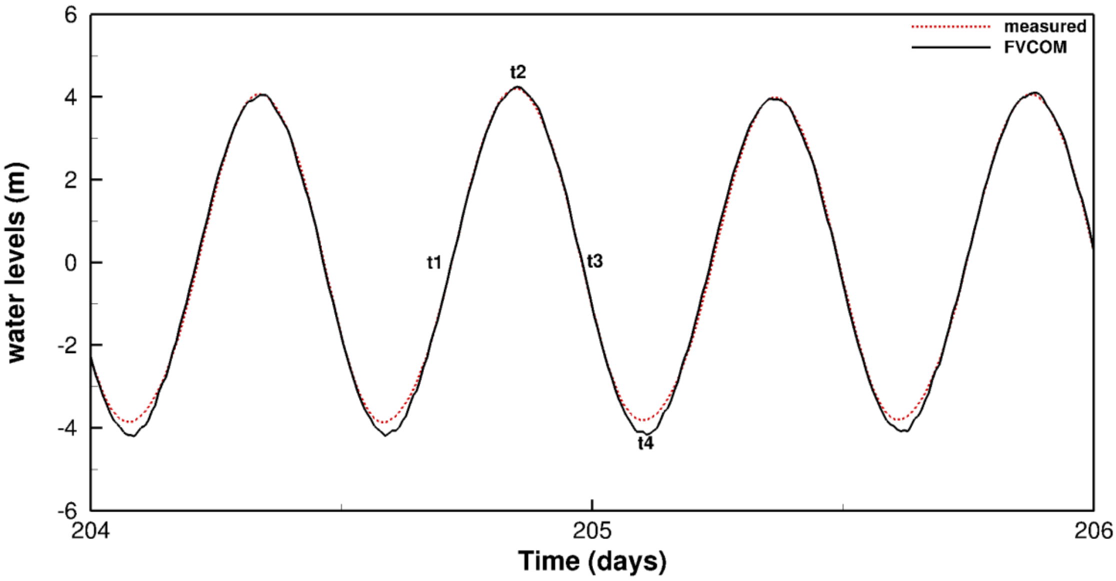

Figure 5.17: Comparison of simulated vs. measured water levels at Location 1. Time stamps t1, t2, t3, t4 refer to four selected points in time at which current comparisons in the vertical direction are performed.

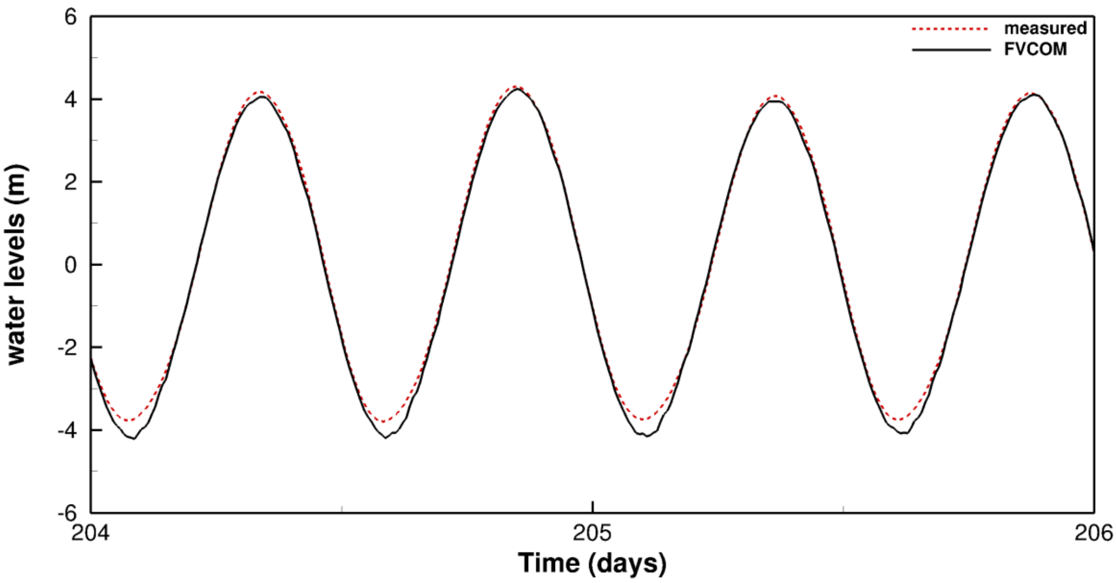

Figure 5.18: Comparison of simulated vs. measured water levels at Location 2.

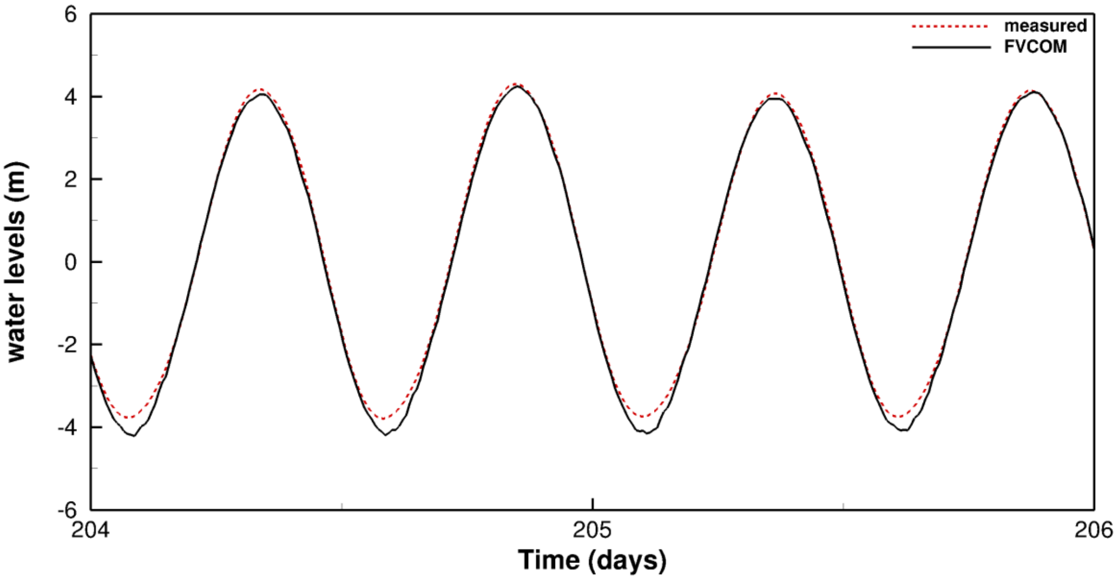

Figure 5.19: Comparison of simulated vs. measured water levels at Location 3.

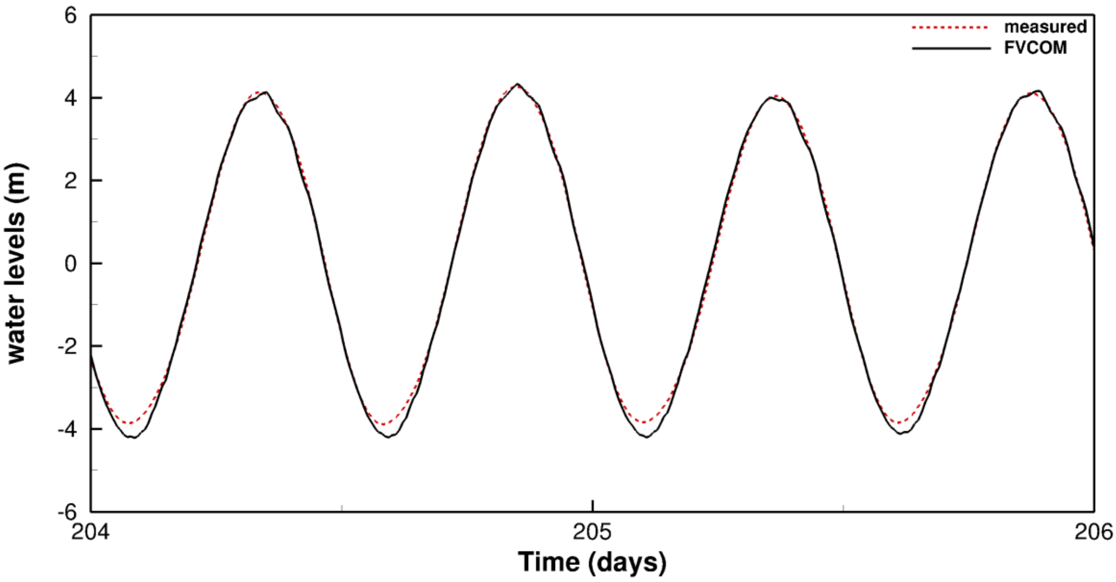

Figure 5.20: Comparison of simulated vs. measured water levels at Location 4.

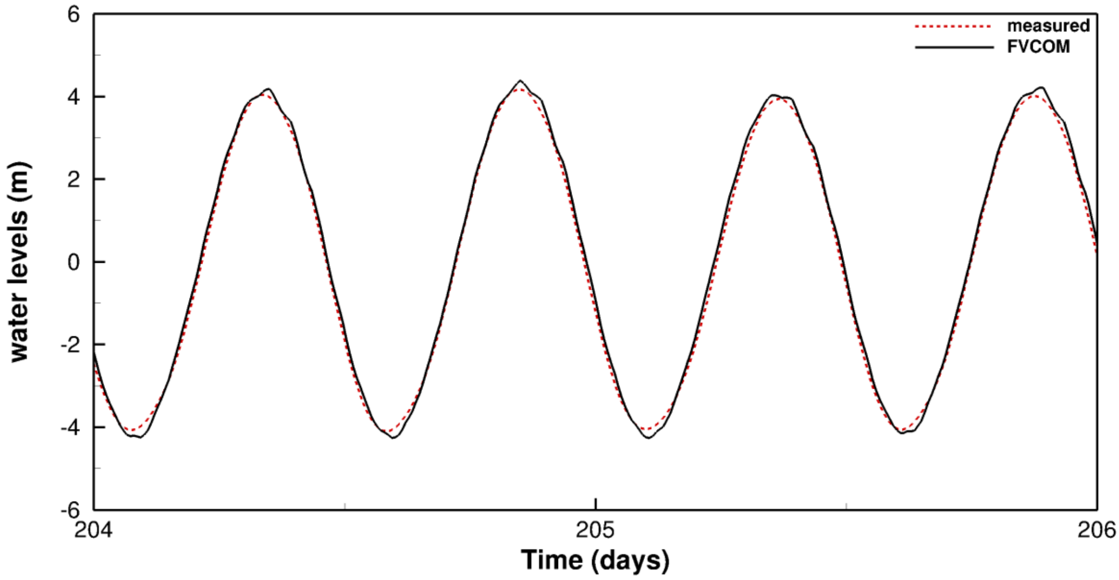

Figure 5.21: Comparison of simulated vs. measured water levels at Location 5.

It can be observed from the figures that the model accurately predicts water levels at all the locations. However, differences can be observed at low tides where the models over-predict water levels in comparison to measurements. The RMSE values between model-predicted and measured water levels at each of the five locations are presented in Table 5.6. The RMSE values are highest for Location 5; however the error magnitude (=0.22m) is about 2.3% of the observed MHWS (~9.4m) at the sites and falls well below the +/- 10% limit recommended by FWR (1993).

Table 5.6: Root Mean Square Error between model-predicted and measured water levels and depth-averaged currents at five locations in Swansea Bay.

RMSE	L1	L2	L3	L4	L5
Water levels (m)	0.17	0.21	0.19	0.20	0.22
Depth-averaged current speed (m/s)	0.13	0.08	0.08	0.07	0.05
Depth-averaged current direction (°)	42.6	36.6	38.5	49.9	50.6

Figure 5.22 to Figure 5.26 present a comparison of model-predicted depth-averaged current speeds with field measurements at the five locations.

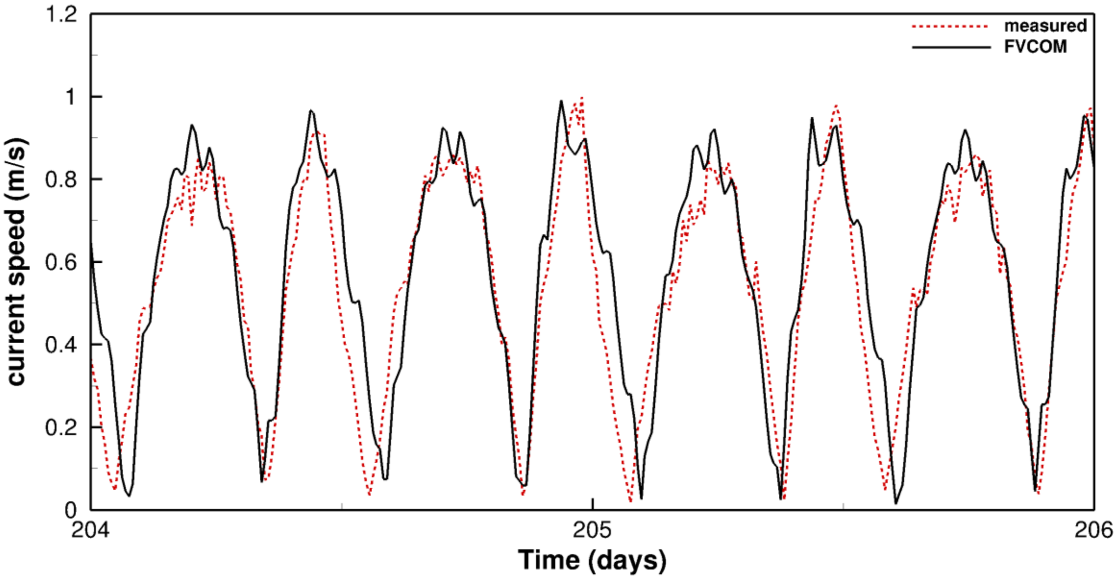

Figure 5.22: Comparison of simulated vs. measured depth-averaged current speeds at Location 1.

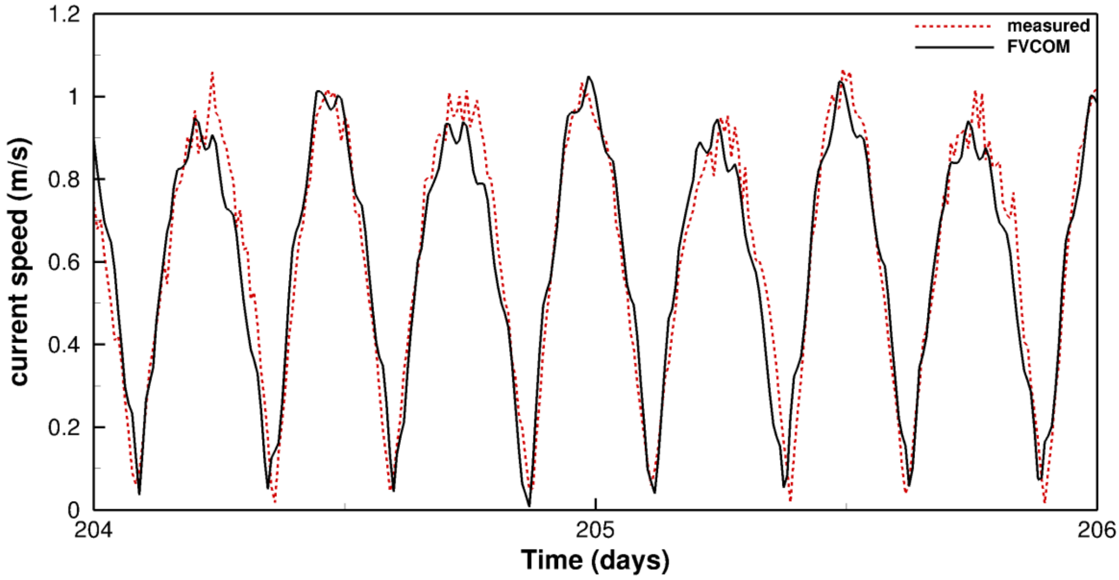

Figure 5.23: Comparison of simulated vs. measured depth-averaged current speeds at Location 2.

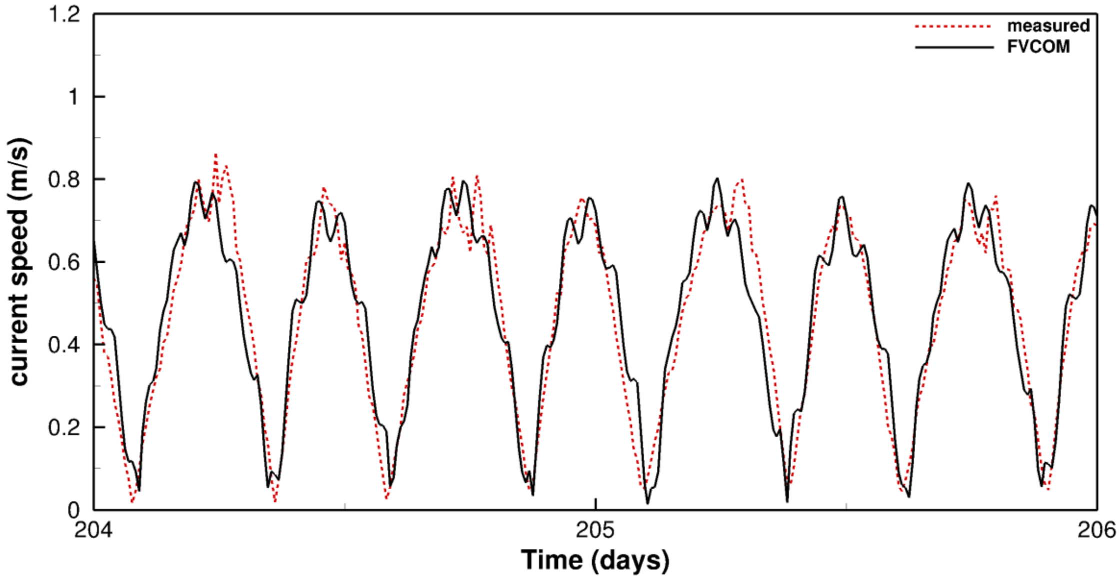

Figure 5.24: Comparison of simulated vs. measured depth-averaged current speeds at Location 3.

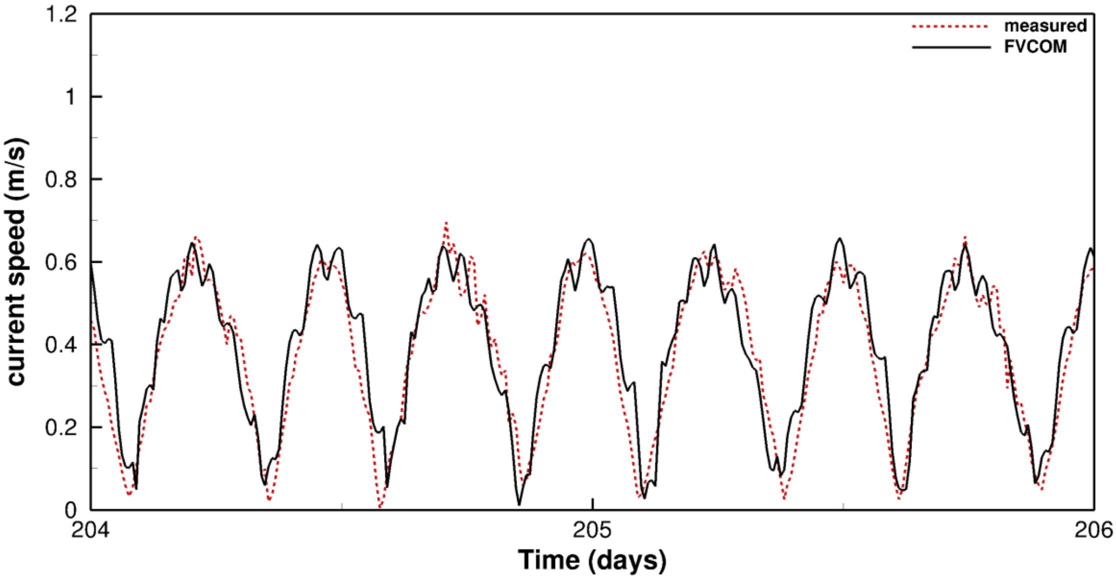

Figure 5.25: Comparison of simulated vs. measured depth-averaged current speeds at Location 4.

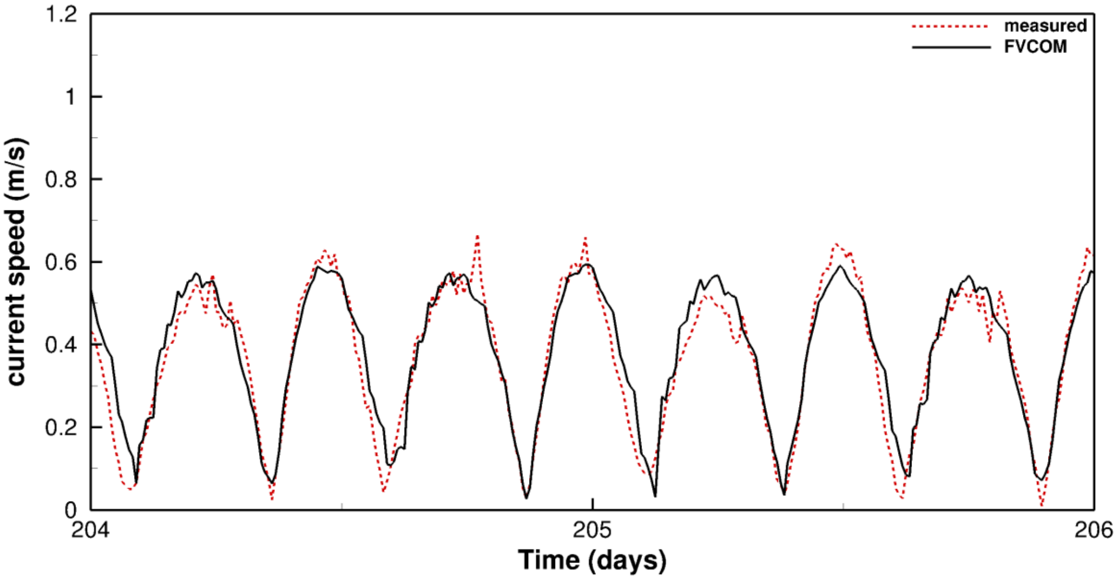

Figure 5.26: Comparison of simulated vs. measured depth-averaged current speeds at Location 5.

It can be observed from the figures that the model results are in agreement with the measurements. The RMSE values between predicted and measured depth-averaged current speeds presented in Table 5.6 show that the maximum error is at Location 1 with a magnitude of 0.13m/s. The differences between predictions and observations can be attributed to a combination of several factors. For example, at some of the locations where field data was collected, shifting of sands near the bed was frequently observed. This can slightly alter the bathymetry and measurement data at these locations which the model fails to represent. In addition, the model does not consider the effect of wind on surface water speeds which are accounted for in field measurements.

Figure 5.27 to Figure 5.31 present a comparison of model-predicted current directions with field measurements at the five locations.

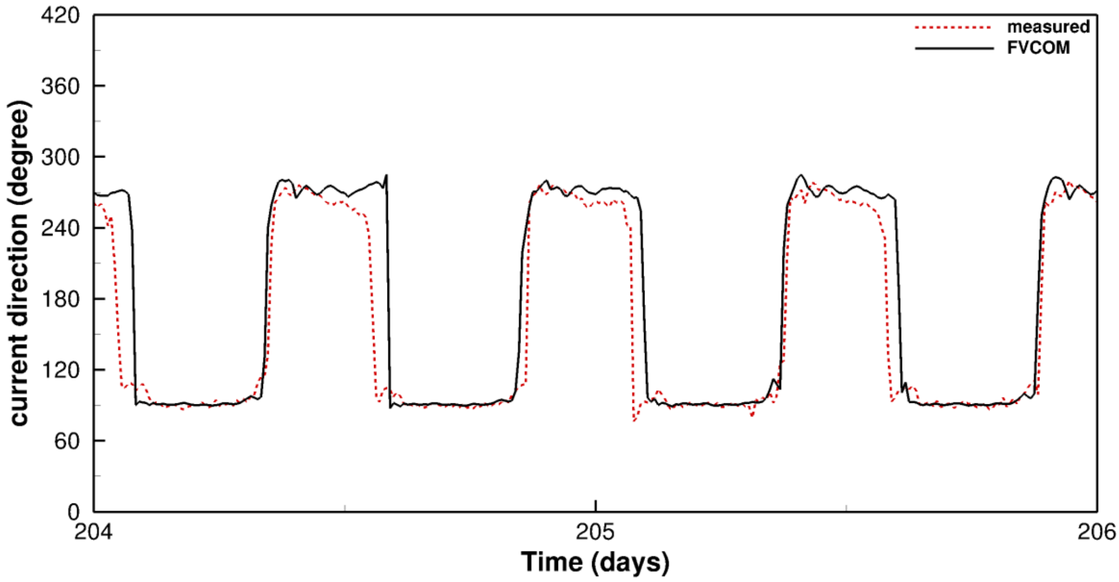

Figure 5.27: Comparison of simulated vs. measured depth-averaged current directions at Location 1.

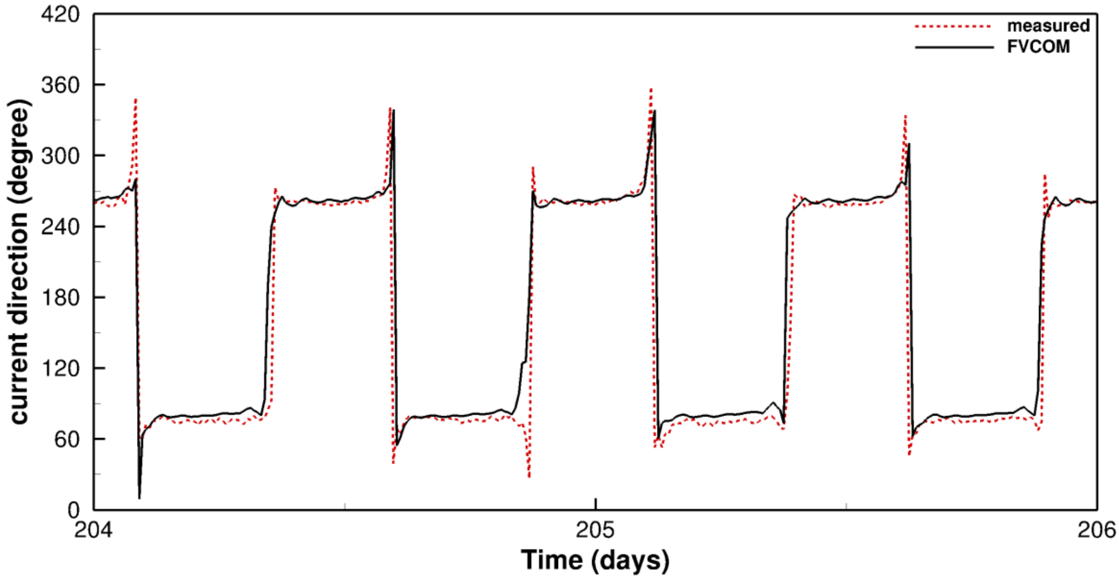

Figure 5.28: Comparison of simulated vs. measured depth-averaged current directions at Location 2.

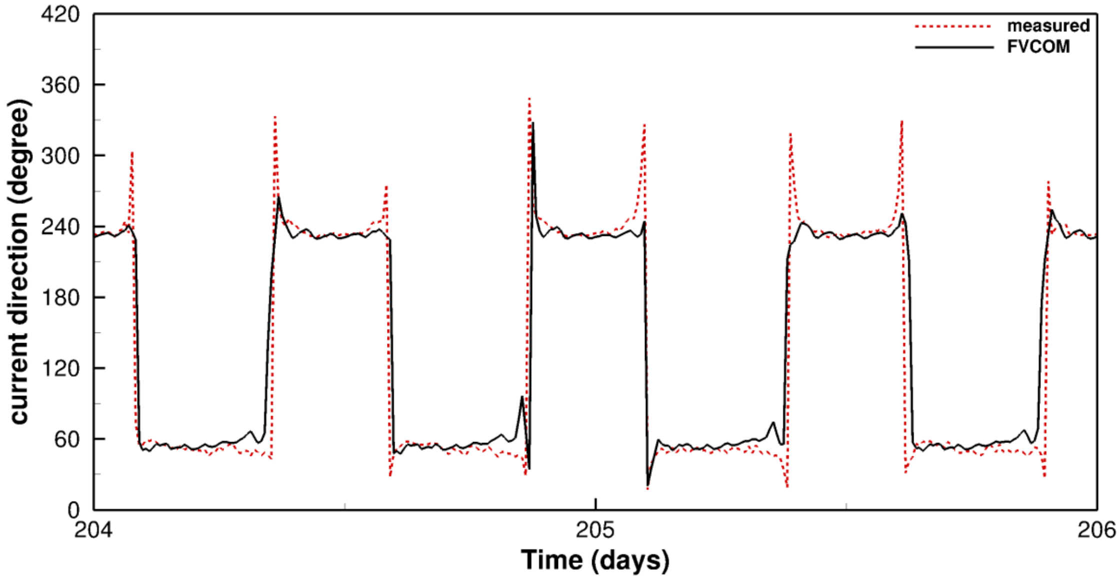

Figure 5.29: Comparison of simulated vs. measured depth-averaged current directions at Location 3.

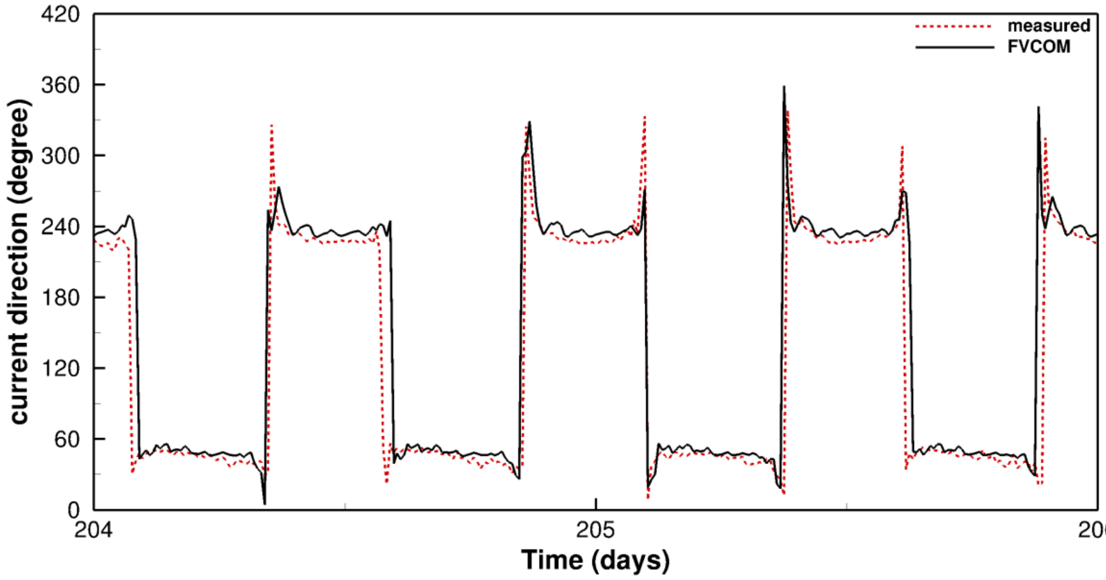

Figure 5.30: Comparison of simulated vs. measured depth-averaged current directions at Location 4.

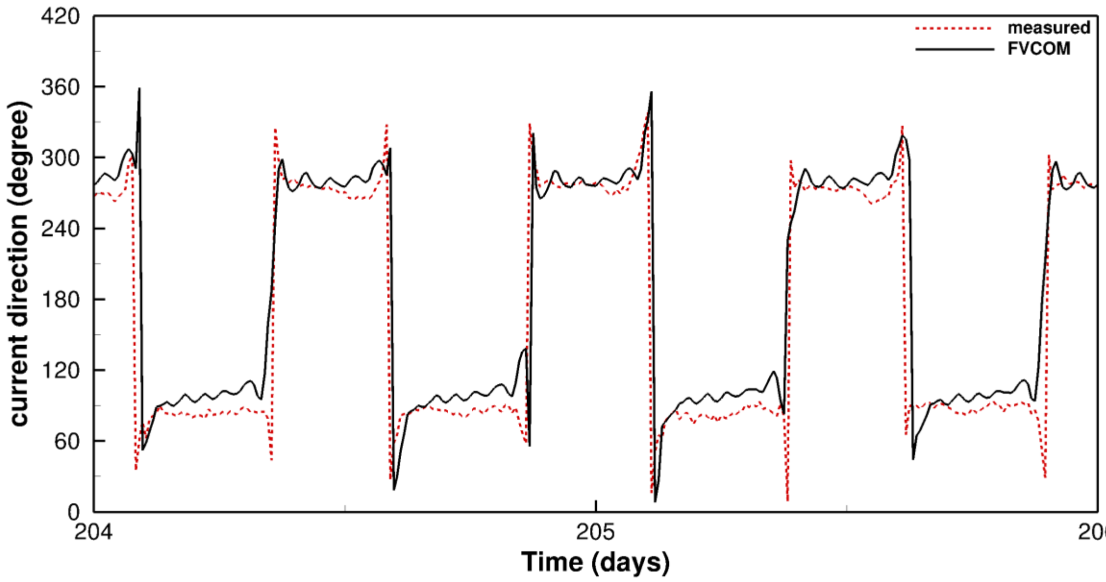

Figure 5.31: Comparison of simulated vs. measured depth-averaged current directions at Location 5.

It can be observed from the figures that at locations L1, L2, and L5 the currents are rectilinear with an angle of 90 degrees during the incoming tide and 270 degrees during the outgoing tide. At locations L3 and L4, the currents are oriented at angles of 60 and 240 degrees for incoming and outgoing tides respectively. The calculated RMSE values presented in Table 5.6 show that the maximum error is at Location 5 with a magnitude of 50.6 degrees. The significantly high RMSE in current direction can be attributed to the current directions at slack tide being not well predicted in the model. This can be appreciated in the figures where the model-predicted current direction agrees generally well with the measurements for most part of the tidal cycle expect at slack tides. It is believed that the differences with field measurements are a result of local effects like wind which can be especially important when current magnitudes are close to zero near slack tide.

Figure 5.32(a-d) to Figure 5.36(a-d) present a comparison of model-predicted depth-varying current speeds with field measurements at the five locations. The comparisons are performed at four time instants t1, t2, t3, and t4 corresponding to mid-flood, high water, mid-ebb, and low water respectively as indicated in Figure 5.17.

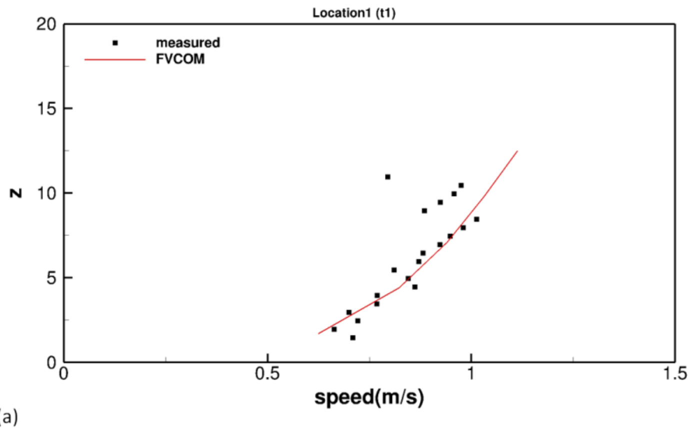

(a)

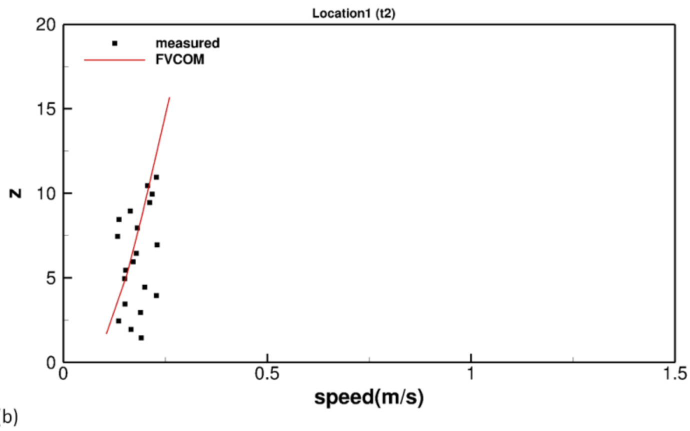

(b)

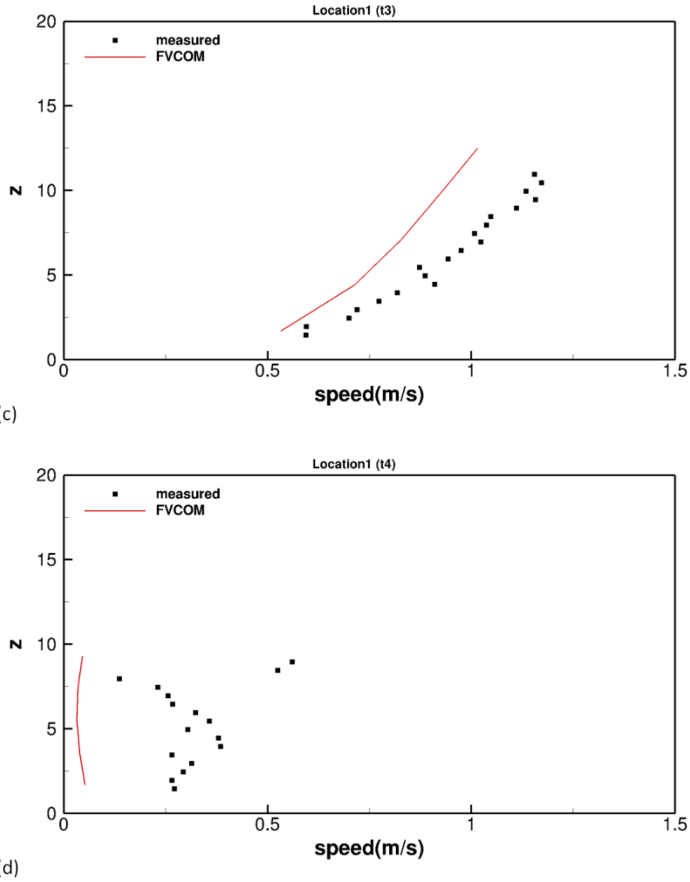

(c)

(d)

Figure 5.32: Simulated vs. measured profiles of current speeds at Location 1.

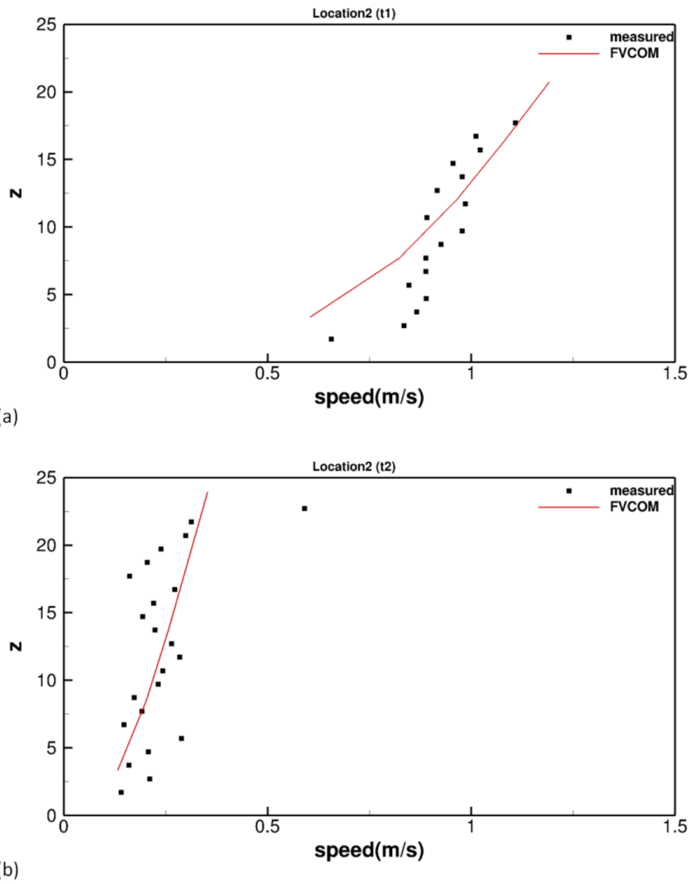

(a)

(b)

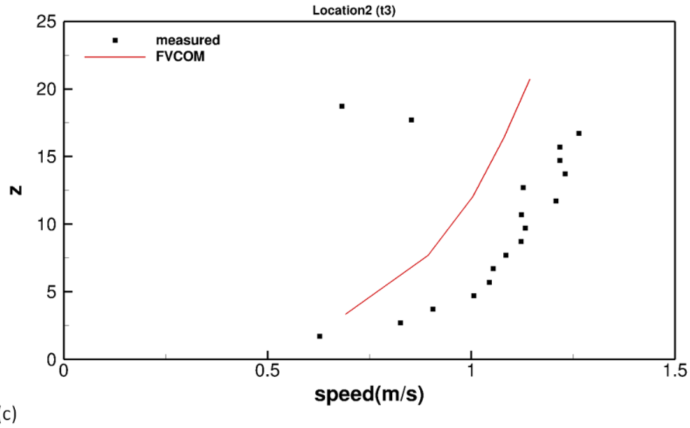

(c)

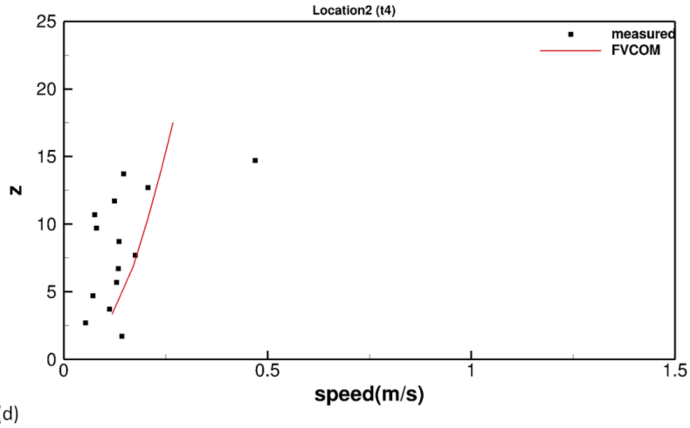

(d)

Figure 5.33: Simulated vs. measured profiles of current speeds at Location 2.

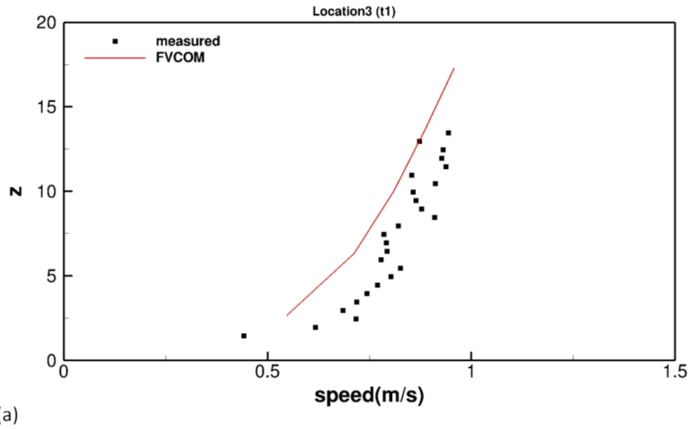

(a)

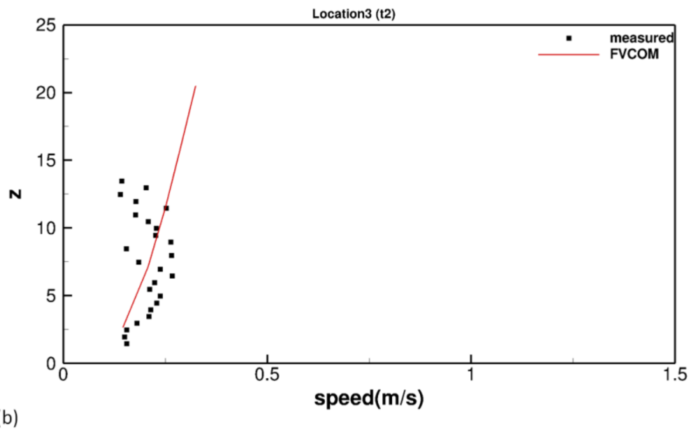

(b)

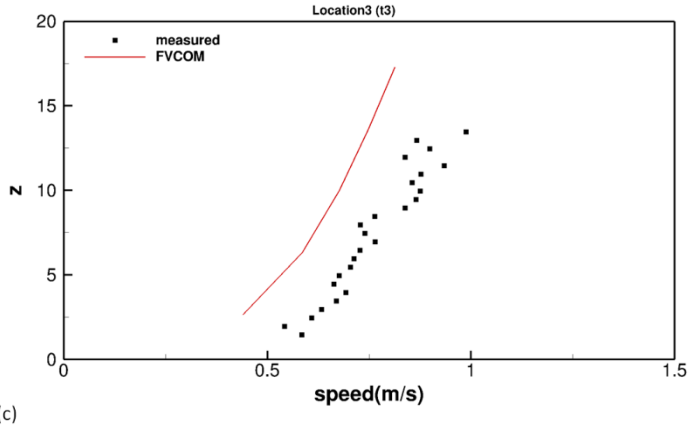

(c)

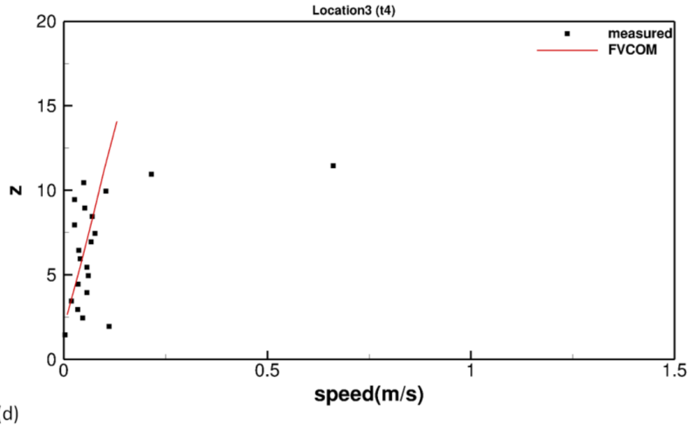

(d)

Figure 5.34: Simulated vs. measured profiles of current speeds at Location 3.

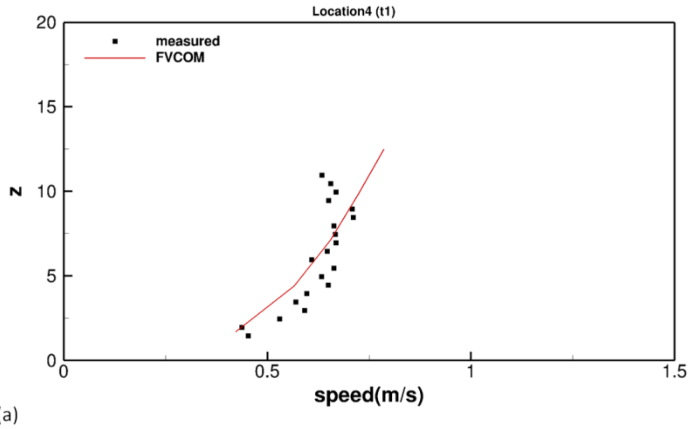

(a)

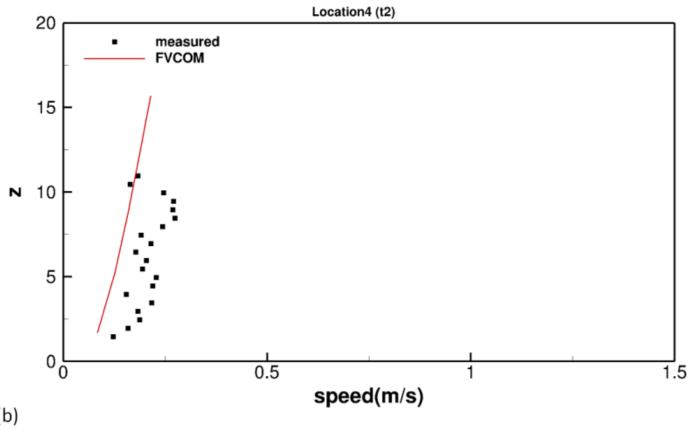

(b)

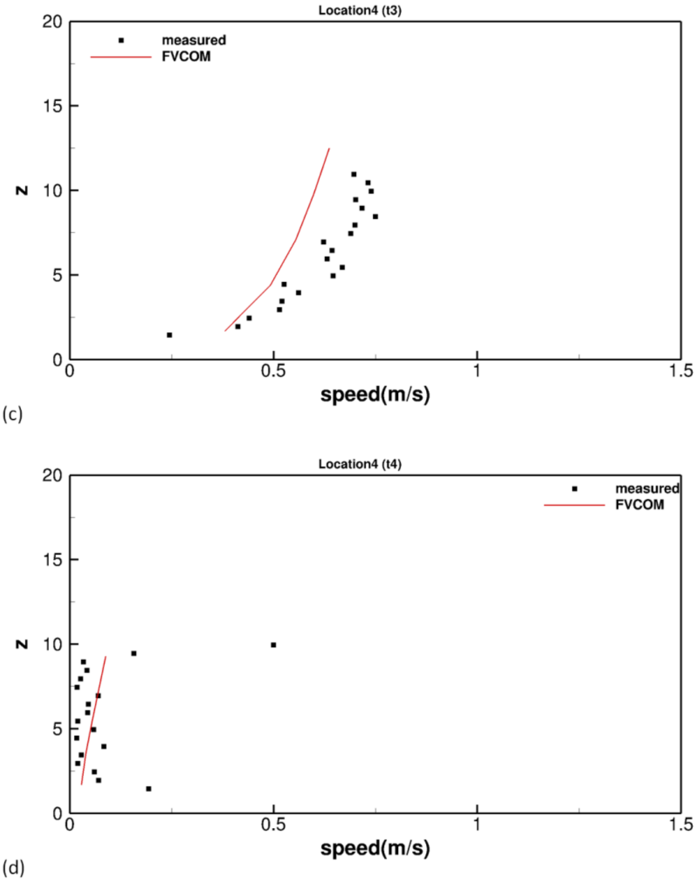

Figure 5.35: Simulated vs. measured profiles of current speeds at Location 4.

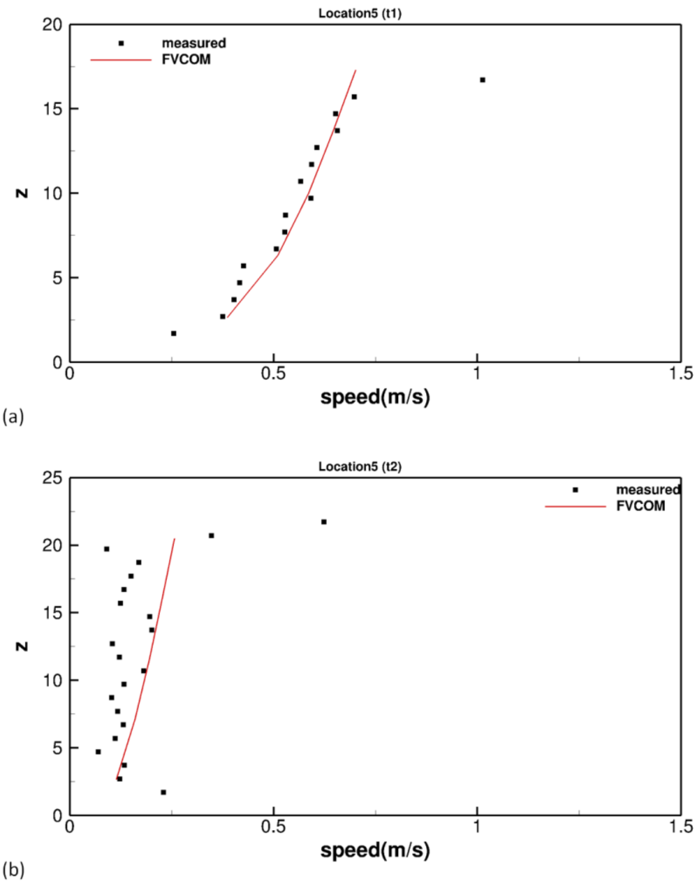

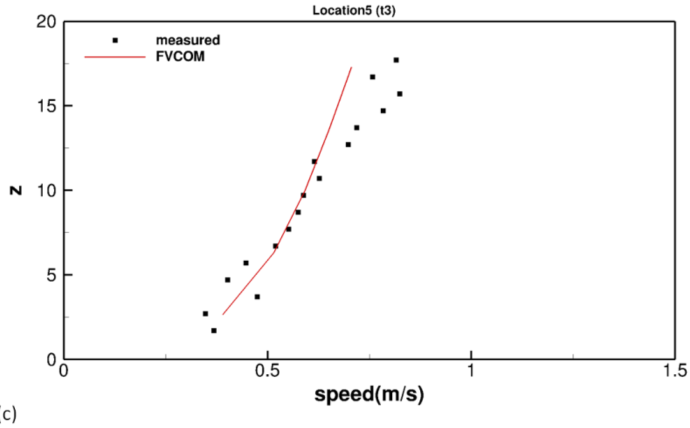

(c)

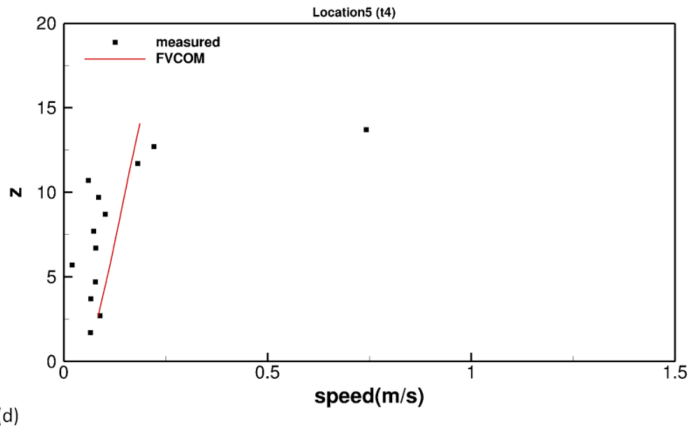

(d)

Figure 5.36: Simulated vs. measured profiles of current speeds at Location 5.

It can be observed from the figures that along the water depth, the model-predicted current speeds seem to follow a logarithmic profile in accordance with the field measurements. The current speeds, as expected, are higher during mid-flood (t1) and mid-ebb (t3) in comparison to high water (t2) and low water (t4). The spatial variability of current magnitudes can be observed with locations L1 and L2 featuring the highest current speeds in comparison to locations L3, L4, and L5. Near the water surface the model under-predicts the current speeds in comparison to measurements. It is believed that the large surface current speeds observed in the field is because of the wind blowing over the water surface which the model does not take into consideration.

Table 5.7 presents the RMSE values between measured and predicted current profiles for each time instant and location. Significant variability in RMSE values can be observed during a tidal cycle with highest error at mid-ebb tide ('t3') for all the locations except L1 and L5 where the error is highest at low-water ('t4'). The RMSE values are highest at location L1, as also indicated by RMSE values for depth-averaged current magnitudes in Table 5.6. The close proximity of L1 to the shoreline could be a reason for large RMSE values at this location as there is higher possibility of inaccurate representation of bathymetry in the model near the inter-tidal zones/boundaries. Overall, the model predicts the current magnitudes reasonably well in comparison to field measurements, however, discrepancies can be observed at certain locations and time instants. It is believed that observed model vs. measured discrepancies could be due to a combination of different factors such as wind or shifting sands at channel bottom which can alter bathymetry locally that are not represented in the model.

Table 5.7: Root Mean Square Error between model-predicted and measured current speed vertical profiles for four selected time instants at five locations in Swansea Bay.

RMSE	L1	L2	L3	L4	L5
Current speed vertical profile at mid-flood (t1)	0.09	0.18	0.13	0.08	0.09
Current speed vertical profile at high water (t2)	0.06	0.08	0.06	0.1	0.1
Current speed vertical profile at mid-ebb (t3)	0.21	0.23	0.2	0.13	0.07
Current speed vertical profile at low water (t4)	0.3	0.09	0.13	0.11	0.16

5.4.2 Simulated vs. Measured drogue tracks

In order to simulate the drogue movement in the field, particles are released in the model at the exact release locations and their transport is modelled using the Lagrangian particle tracking method. Figure 5.37 shows the comparison of simulated vs. measured tracks of four drogues released approximately at high water on 04/07/2011 at an offshore location. In the figure, the symbols represent measurements whereas the lines represent simulation results. Out of the four drogues, two drogues represented in the figure by red, blue colours correspond to releases at 9:22 AM, 9:38 AM respectively and at a vertical depth of 1m. The two drogues represented in the figure by black, green colours correspond to releases at 9:24AM, 9:40AM respectively and at a vertical depth of 2m. It can be observed from the figure that the model seems to accurately predict the general direction of flow during the outgoing and incoming tides at this location. However, the simulated drogues seem to move slightly towards the south unlike the drogues in the field.

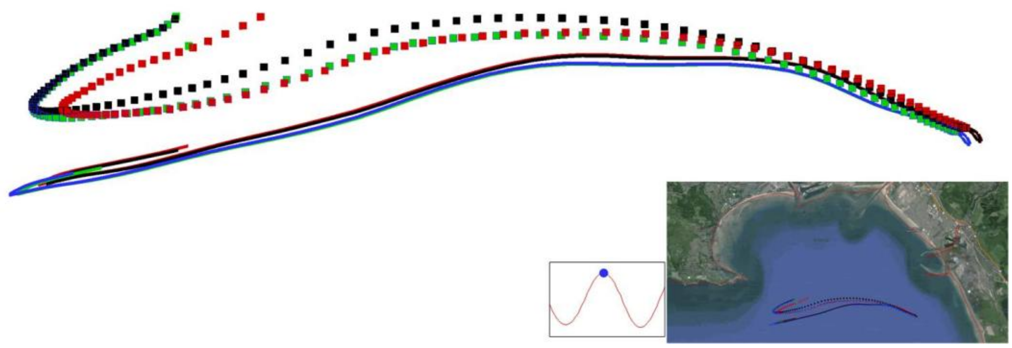

Figure 5.37: Observed (symbols) vs. simulated (lines) drogue movements at an offshore location corresponding to releases on 04/07/2011. 1m drogues are represented by red and blue symbols/lines, whereas 2m drogues are represented by black and green symbols/lines. Time of drogue release is indicated by blue symbol in the tide curve plotted as inset.

Similar to Figure 5.37, comparison of simulated vs. measured drogue tracks for releases on 09/06/2011 (approximately at mid-flood) is performed and shown in Figure 5.38. The drogues represented in red, blue colours correspond to releases at 9:24AM, 9:47AM respectively and at a vertical depth of 1m. The drogues represented in black, green colours correspond to releases at 9:23AM, 9:46AM respectively and at a vertical depth of 2m. It can be observed from the figure that the model accurately predicts the flow direction during the incoming tide, whereas the model fails to capture the recirculating flow pattern on the outgoing tide. It is believed that during the day of measurements the surface waters might have been influenced by wind in the field causing the drogues to deviate from the outgoing tide direction. This is confirmed through wind data observations at Swansea provided by the City and County of Swansea (http://www.swansea.airqualitydata.com/cgi-bin/reporting.cgi). Meteorological data at the 30m Mast – Cwm Level Park monitoring station indicates that west-south-westerly winds with a magnitude of approximately 5m/s have been observed in the afternoon of 09/06/11 at 10m height. As indicated in Figure 5.37, wind from this direction could have caused the drogues in the field to deviate their path from the outgoing tide direction. Since local wind effects were not included in the model, the simulated drogues seem to follow the outgoing tide direction in the bay.

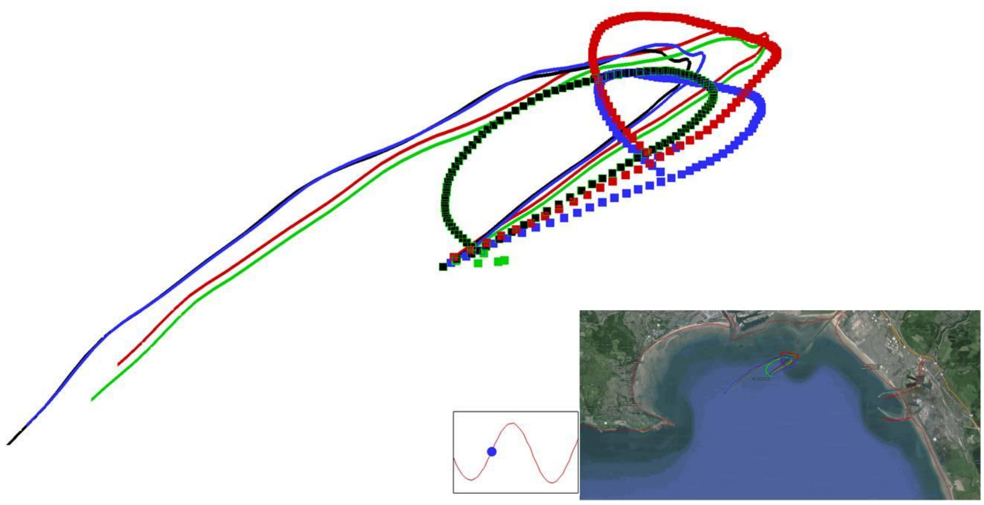

Figure 5.38: Observed (symbols) vs. simulated (lines) drogue movements near the River Neath on 09/06/2011. 1m drogues are represented by red and blue symbols/lines, whereas 2m drogues are represented by black and green symbols/lines. Time of drogue release is indicated by blue symbol in the tide curve plotted as inset.

Figure 5.39 and Figure 5.40 show the simulated vs. measured tracks of drogue releases at mid-flood near the River Tawe on 27/06/2011 and 28/06/2011 respectively. In Figure 5.39, the drogues represented in red, blue colours correspond to releases at 1:26PM, 1:42PM respectively and at a vertical depth of 1m, whereas, the drogues represented in black, green colours correspond to releases at 1:23PM, 1:45PM respectively and at a vertical depth of 2m. Similarly, in Figure 5.40, the drogues represented in red, blue correspond to releases at 2:15PM, 2:32PM respectively and at a vertical depth of 1m, whereas, the drogues represented in black, green colours correspond to releases at 2:13PM, 2:33PM respectively and at a vertical depth of 2m.

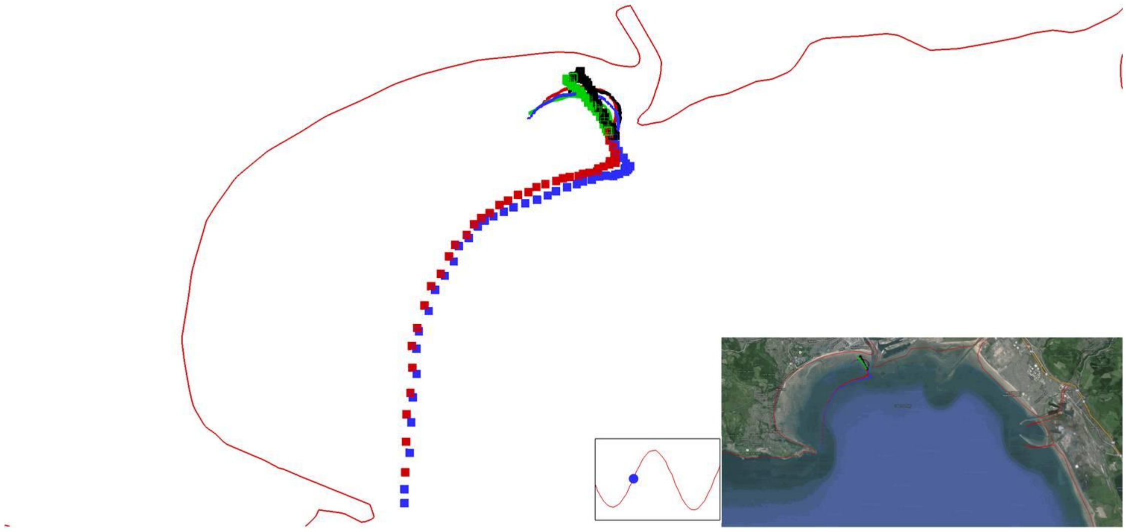

Figure 5.39: Observed (symbols) vs. simulated (lines) drogue movements near the River Tawe on 27/06/2011. 1m drogues are represented by red and blue symbols/lines, whereas 2m drogues are represented by black and green symbols/lines. Time of drogue release is indicated by blue symbol in the tide curve plotted as inset.

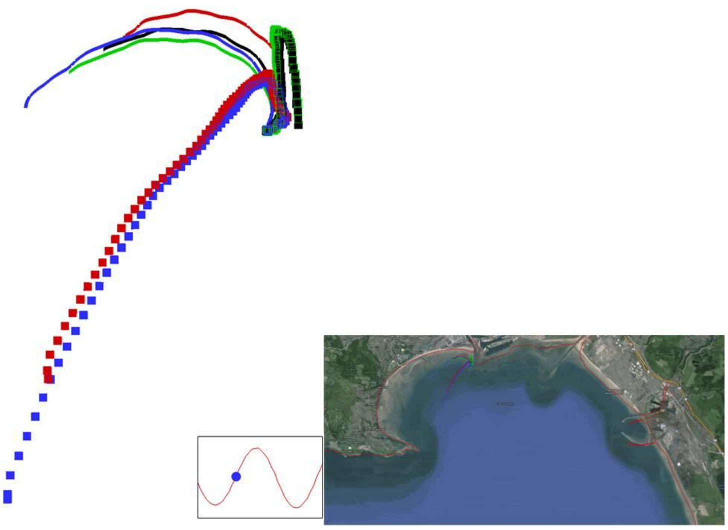

Figure 5.40: Observed (symbols) vs. simulated (lines) drogue movements near the River Tawe on 28/06/2011. 1m drogues are represented by red and blue symbols/lines, whereas 2m drogues are represented by black and green symbols/lines. Time of drogue release is indicated by blue symbol in the tide curve plotted as inset.

Figure 5.39 and Figure 5.40 show that the 1m drogues in the field moved in the opposite direction to the 2m drogues. However, the model results show that all drogues move inward irrespective of the depth of release. In view of investigating the reason behind the movement of drogues in opposite directions, additional simulations are performed with enhanced vertical grid resolution (three-fold) and improved coastline geometry near River Tawe. Figure 5.41 shows the results from these simulations for the drogue release corresponding to 27/06/2011. Also shown in the figure is the coastline from the original computational domain (represented in black).

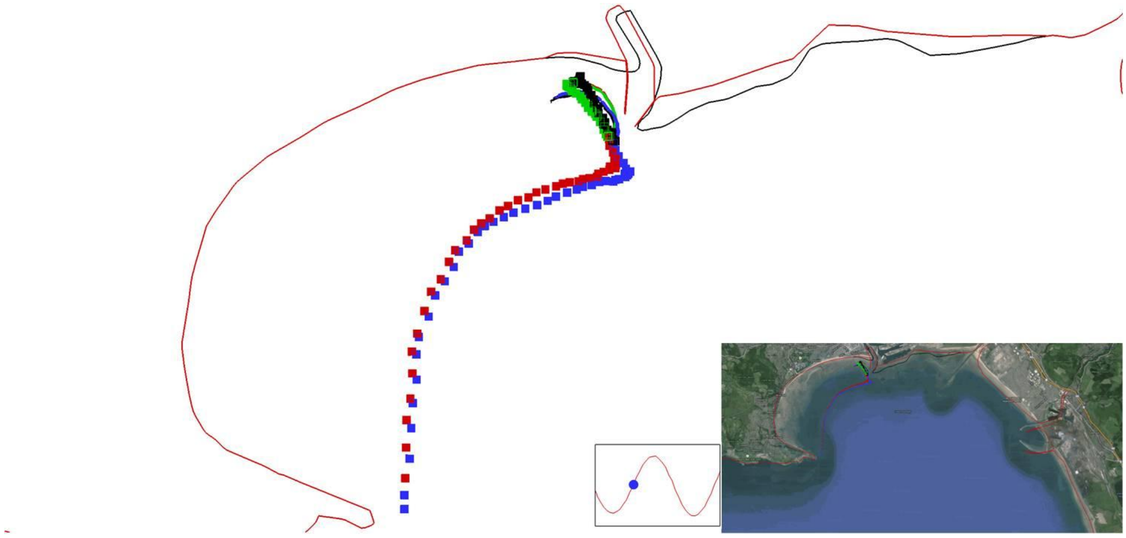

Figure 5.41: Observed (symbols) vs. simulated (lines) drogue movements near the River Tawe on 27/06/2011 for modified computational domain shown in red. 1m drogues are represented by red and blue symbols/lines, whereas 2m drogues are represented by black and green symbols/lines. Time of drogue release is indicated by blue symbol in the tide curve plotted as inset.

It can be observed from the figure that there is no marked improvement in the model results and the 1m and 2m drogues moved towards the bay as in the previous simulations. This suggests that the flow hydrodynamics has not significantly changed with modifications to vertical grid resolution and coastline geometry and therefore had no influence on the movement of 1m drogues away from the bay. It is believed that wind had a significant effect during the day of measurements causing the 1m drogues (located much closer to the water surface) to move against the tide in the opposite direction of the 2m drogues. Wind data from the 30m Mast – Cwm Level Park monitoring station show that north-north-westerly winds with a magnitude of 4.0m/s were observed on 27/06/2011 and 28/06/2011 at 10m height. As seen from Figure 5.39 and Figure 5.40, winds from this direction would have made the drogues in the field move against the tide unlike the simulated drogues which does not include the effects of wind.

Figure 5.42 presents results from the simulations of drogue releases at low water near Mumbles Head on 29/06/2011. In the figure, the drogues represented in red, blue colours correspond to releases at 11:34AM, 11:54AM respectively and at a vertical depth of 1m, whereas, the drogues represented in black, green colours correspond to releases at 11:35AM, 11:56AM respectively and at a vertical depth of 2m.

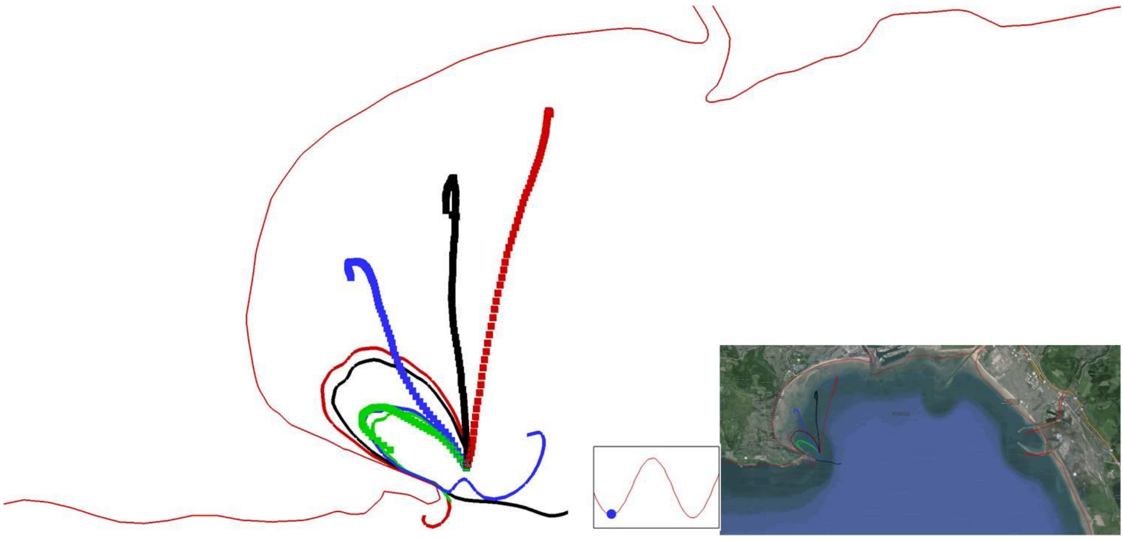

Figure 5.42: Observed (symbols) vs. simulated (lines) drogue movements at Mumbles Head on 29/06/2011. 1m drogues are represented by red and blue symbols/lines, whereas 2m drogues are represented by black and green symbols/lines. Time of drogue release is indicated by blue symbol in the tide curve plotted as inset.

It can be observed from the figure that with the exception of 2m drogues represented in green, all other drogue tracks obtained from the model are dissimilar to the measurements. The drogues in the model seem to follow a circular path due to the eddy-like flow patterns resulting from flow separation at Mumbles Head. Since this feature is not very prominent in the field measurements, investigation of the reason behind over-prediction of flow re-circulation at Mumbles Head is performed. Figure 5.43a presents a closer look at the coastline geometry currently being used to represent Mumbles Head in the model. Since flow recirculation at the Mumbles Head is a consequence of flow separation, it is believed that the sharp geometrical feature of the headland (marked in Figure 5.43a) caused the over-prediction of flow re-circulation in the model. Therefore, additional simulations are conducted with the shape of the coastline modified as shown in Figure 5.43b and Figure 5.43c to investigate the extent of flow-recirculation at the Mumbles headland for the hypothetical cases with extremely smooth and slightly sharp geometric features respectively. The drogue tracks obtained from the simulations with modified Mumbles headland shape are presented in Figure 5.44.

Figure 5.43: a) Original computational domain, b) Hypothetical case with extremely smooth geometrical features at Mumbles Head, and c) Hypothetical case with slightly sharp geometrical features at Mumbles Head.

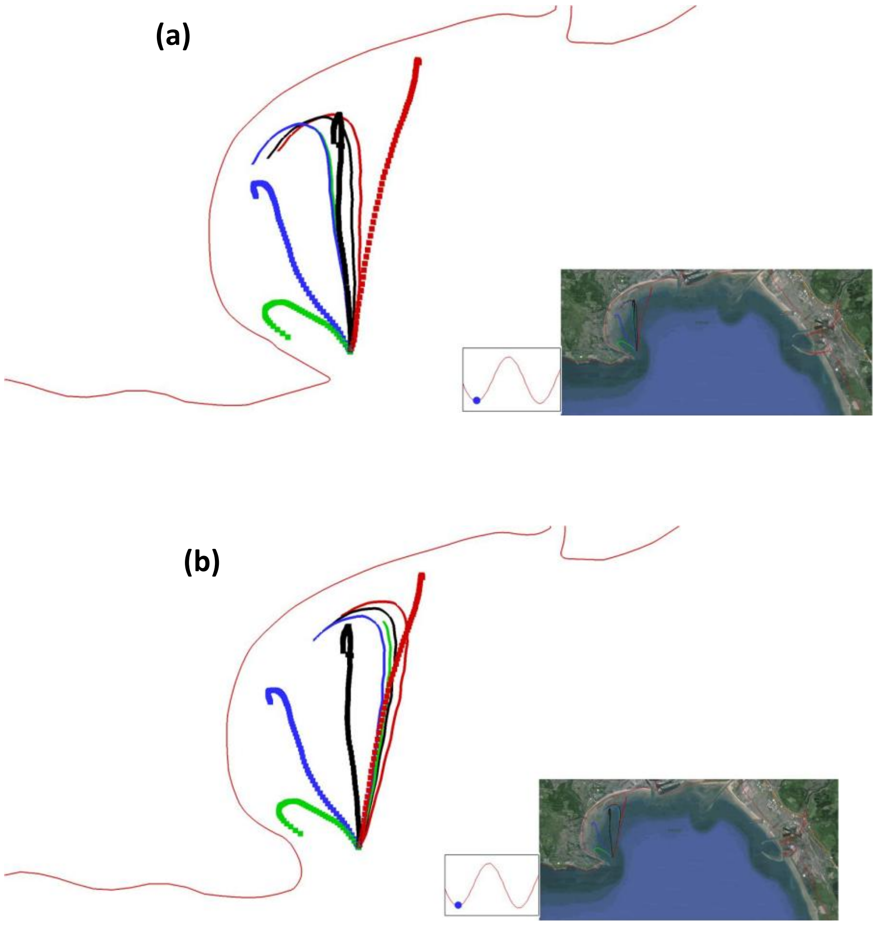

Figure 5.44: Observed (symbols) vs. simulated (lines) drogue movements at Mumbles Head on 29/06/2011 for a) Hypothetical case with extremely smooth geometrical features at Mumbles Head, and b) Hypothetical case with slightly sharp geometrical features at Mumbles Head. Time of drogue release is indicated by blue symbol in the tide curve plotted as inset.

It can be observed from the figure that flow re-circulation is reduced for modified headland shapes (Figure 5.44a, Figure 5.44b) and drogues no longer move in circular paths. Moreover, the extent of re-circulation seems to be related to the smoothness of the headland shape, with the drogues drifting relatively farther away in the extremely smooth case (Figure 5.44a) than the slightly sharp case (Figure 5.44b). Overall, the simulations revealed that the flow hydrodynamics and drogue movement is influenced by the shape of the Mumbles headland used in the model.

Although the coastline geometry used in the model (Figure 5.43a) seems to accurately represent the Mumbles headland, a closer look into the admiralty chart of

Swansea Bay reveals that the headland comprises of two land masses which are incorrectly represented in the model. This can be observed clearly in Figure 5.45 where two images of Mumbles headland at different instants of time are shown. The first image (top panel) shows the Mumbles headland during ebb tide when the water level is at its lowest, whereas the second image (bottom panel) corresponds to a high tide when water inundates the lower areas of Mumbles Head.

Figure 5.45: Top panel- Mumbles Head as one land mass during low tide (http://www.panoramio.com/photo/731975), Bottom panel- Mumbles Head comprising of two disjointed land masses during the major portion of the tidal cycle (http://www.geograph.org.uk/photo/3213222).

It can be observed from the figure that Mumbles headland comprises of two different land masses which are disjointed during the major portion of a tidal cycle and only connected during low water. This feature, however, was not included in the model setup because of the lack of high resolution bathymetry in the region and due to the assumption that flow in Swansea Bay is not affected significantly by such small changes to the computational domain. Since the model results shown in Figure 5.44 revealed the sensitivity of flow re-circulation to the shape of the headland, the downside of inaccurately representing Mumbles Head as a single land mass irrespective of the tide being low or high is investigated. Figure 5.46 shows the comparison of model-predicted flow patterns against simplified flow sketches from the work of Ferentinos and Collins (1979).

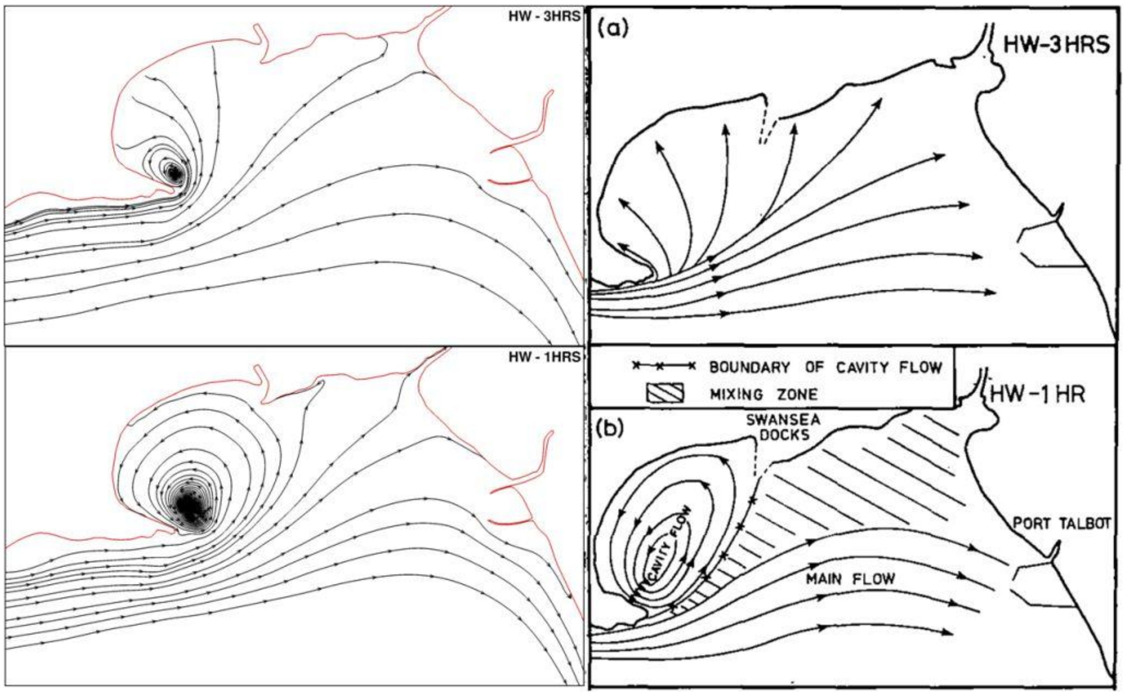

Figure 5.46: Comparison of model-predicted flow patterns against simplified flow sketches from the work of Ferentinos and Collins (1979).

In general, the model seems to predict the flow patterns well at three and one hours before High Water (HW) at Swansea Bay. However, in the model, at HW-3hrs the flow has already separated at Mumbles Head with the formation of an eddy, unlike the observations of Ferentinos and Collins (1979). It is believed that the extended Mumbles headland shape in the model caused the flow to separate at lower current speeds during the early stages of the flood tide. Moreover, these observations also explain the movement of drogues (released during the early stages of the flood tide) in circular paths at Mumbles Head unlike the field measurements.

5.5 FIO Modelling

In this section results from model simulations related to the transport of faecal indicator organisms are analysed for an assessment of faecal coliform pollution at Swansea Bay. Firstly, the fate and transport of FIO and the extent of pollution within the bay is studied. Next, validation of numerical model results through comparison of model-predicted vs. measured FIO concentrations at three selected sites is performed. Finally, the spatial and temporal variability of FIO concentrations at Swansea Bay's DSP is investigated.

5.5.1 FIO distribution at Swansea Bay

For a general understanding of the transport of faecal indicator organisms (E. coli) affecting the bathing water quality in Swansea Bay, contours of FIO concentrations are plotted at different stages of a tidal cycle in Figure 5.47 to Figure 5.51. Figure 5.47 corresponds to a time instant when water enters the bay during a flood tide at approximately 3 hours before high water (HW). Figure 5.48 corresponds to a time instant close to high water in the bay at approximately 1 hour before HW. Figure 5.49 corresponds to a time instant when the flood tide recedes and a transition to ebb tide begins approximately 1 hour after HW. Figure 5.50 corresponds to a time instant when water drains from the bay during an ebb tide at approximately three hours after HW. Figure 5.51 corresponds to a time instant close to low water (LW) in the bay. Also shown in the figures is the Swansea Bay DSP where water samples are collected during the bathing season to check for compliance with water quality standards.

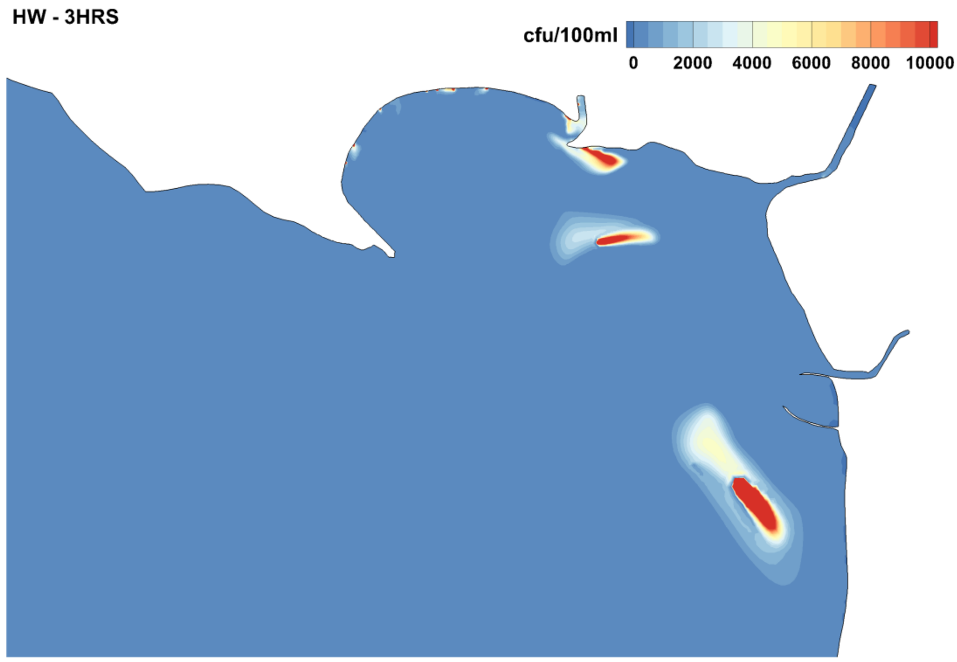

Figure 5.47: Contours of FIO concentrations in Swansea Bay at a time instant when water enters the bay during a flood tide.

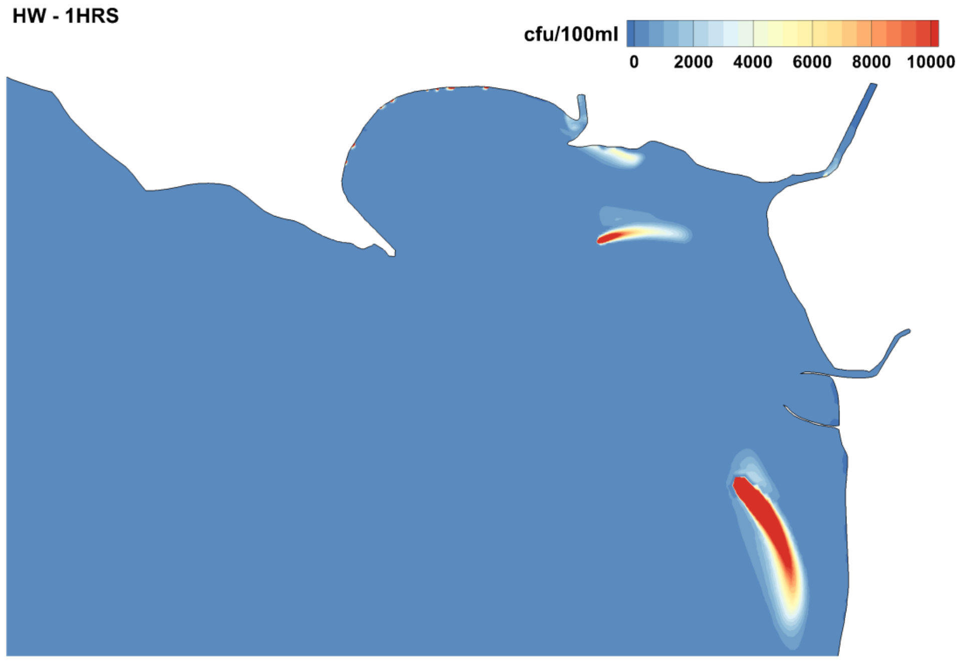

Figure 5.48: Contours of FIO concentrations in Swansea Bay a time instant close to high water.

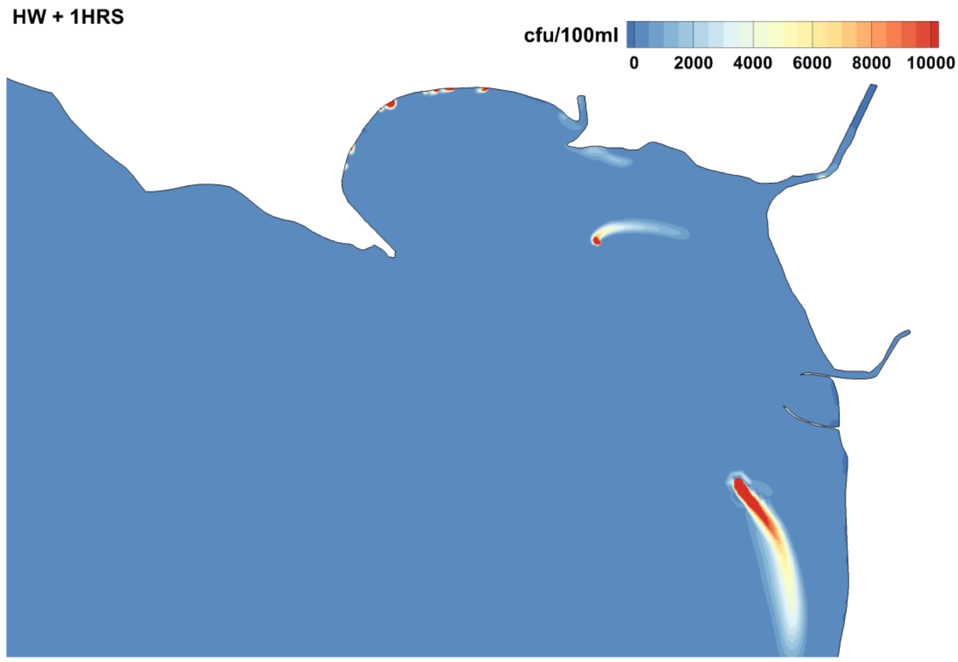

Figure 5.49: Contours of FIO concentrations in Swansea Bay at a time instant when the flood tide recedes and a transition to ebb tide begins.

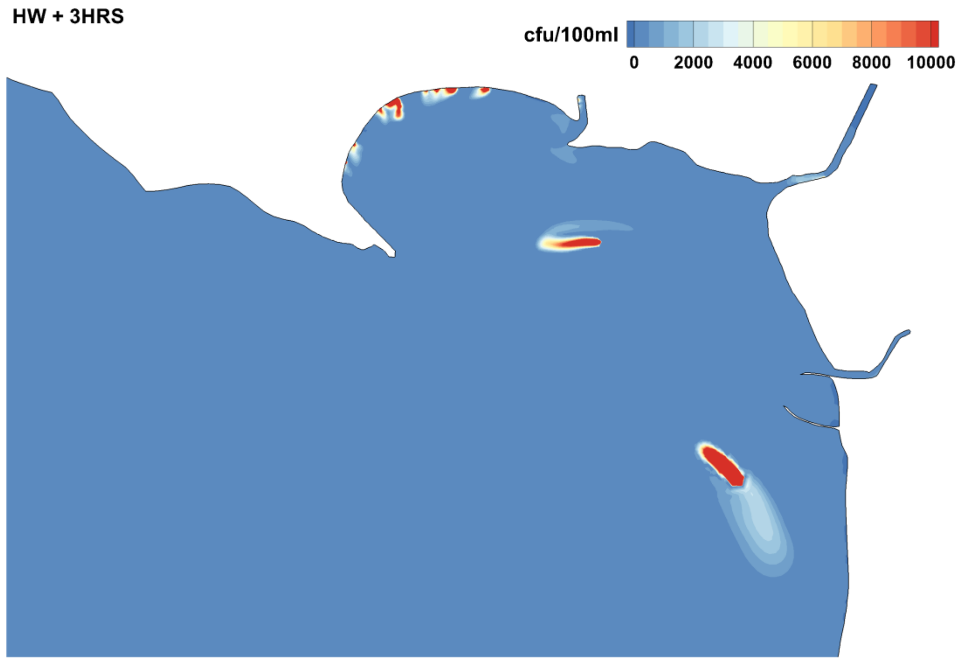

Figure 5.50: Contours of FIO concentrations in Swansea Bay at a time instant when water drains from the bay during an ebb tide.

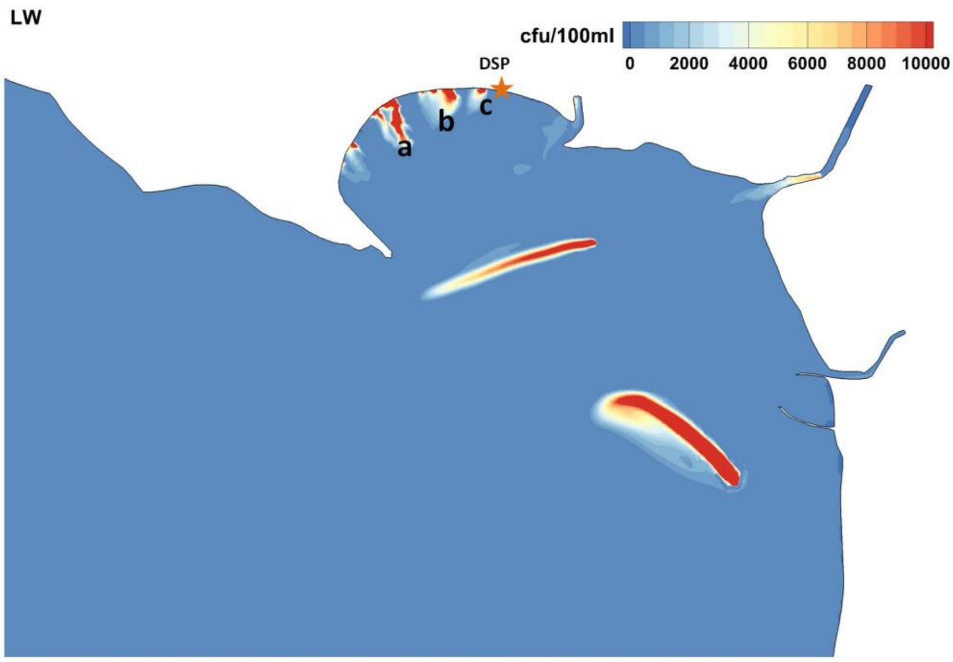

Figure 5.51: Contours of FIO concentrations in Swansea Bay at a time instant close to low water.

Figure 5.47 to Figure 5.51 show qualitatively the transport of pollutants discharged from various sources along the bay and from the offshore sewage effluents. The magnitude of FIO concentrations and extent of pollution over the entire bay can be appreciated from these figures. Overall, the three regions marked as ‘a’, ‘b’, and ‘c’ in Figure 5.51 are the most highly polluted areas close to the bay. Analysis of pollution sources along the bay (see Figure 5.6) reveal that the pollution at region ‘a’ is a direct consequence of pollutants discharged from two sources: a surface water outlet (at Norton Avenue), and a stream (Washing house Brook). Likewise, the pollution at region ‘b’ is a result of three sources: a surface water outlet (at Sketty Lane), and two streams (University Stream and Brynmill Stream). Similarly, the pollution at region ‘c’ is a result of the pollutants from a surface water outlet (Patti Pavillion). Out of three regions, region ‘c’ appears to be a major concern to Swansea Bay because its proximity to the DSP affects the rating of the beaches nearby.

In addition to the spatial distribution of FIO concentrations in the bay, Figure 5.47 to Figure 5.51 shows the variability of FIO concentrations over time. The pollution sources influence negatively the water quality in the bay during mid-flood (HW – 3 hrs), mid-ebb (HW + 3 hrs), and low tides (LW). A noticeable feature in all the figures is the variation of FIO concentration at the offshore effluent sites. The change in direction of plume with the tide and the dispersion of pollutants can be clearly observed from the figures. In order to quantitatively evaluate the accuracy of model-predicted FIO concentrations, comparison of simulation results with field measurements is performed as described in the following section.

5.5.2 FIO validation

The data for validation of model-predicted FIO concentrations was obtained through field measurements carried out in Swansea Bay by Aberystwyth University. The field operation consisted of collection of hourly water samples at shoreline sites and three offshore sites: Site1, 2, and 3 shown in Figure 5.6. The sampling was performed for a period of approximately 13 hours continuously on 15th November, 2012. Numerical simulations were carried out for the period between the 9th and 16th November 2012 so that a comparison with field measurements on 15th November could be performed. The model-predicted FIO concentrations data was extracted for the three sites at the field sampling times enabling direct comparison.

The calibration runs were performed by employing various decay rates (T_{90}) and diffusion coefficient values. Initially, simulations are performed with varying decay rates but with a constant diffusion coefficient value (HORCON) of 0.2. Table 5.8 presents a selection of the calibration runs performed and the T_{90} values of FIO decay used in those simulations with other respective details for comparison. The "15 constant" simulation indicated in the table corresponds to a model run with constant day and night T_{90} value of 15 hours. The "60n 15d 12hrs" simulation corresponds to a model run with T_{90} value of 15 hours during the day (over a 12hour period: 6AM-6PM) and T_{90} value of 60 hours during the night (6PM to 6AM). Similarly, the "50n 5d 12hrs" simulation corresponds to a model run with T_{90} value of 5 hours during the day (over a 12hour period: 6AM-6PM) and T_{90} value of 50 hours during the night (6PM to 6AM). The "40n 5d 8hrs" simulation corresponds to a model run with T_{90} value of 5 hours during the day (over an 8hour period: 8AM-4PM) and T_{90} value of 40 hours during the night (4PM to 8AM). The "40n 5d 12hrs" simulation corresponds to a model run with T_{90} value of 5 hours during the day (over a 12hour period: 6AM-6PM) and T_{90} value of 40 hours during the night (6PM to 6AM).

Table 5.8: List of decay rate calibration runs and corresponding T_{90} values

Simulation id	Day	Night	Day (T_{90})	Night (T_{90})
15 constant	-	-	15hrs	15hrs
60n 15d12hrs	6AM-6PM	6PM-6AM	15hrs	60hrs
50n 5d 12hrs	6AM-6PM	6PM-6AM	5hrs	50hrs
40n 5d 8hrs	8AM-4PM	4PM-8AM	5hrs	40hrs
40n 5d 12hrs	6AM-6PM	6PM-6AM	5hrs	40hrs

Comparison of the model predictions with field measurements for each simulation in Table 5.8 is illustrated in FiguresFigure 5.52 toFigure 5.54. As expected, it can be clearly seen from the figures that there is a significant variability of FIO concentration with various T_{90} values used in the model. Depending on the time of the day, the magnitudes can change by a factor of up to 10 times. However, as evident in FiguresFigure 5.52 toFigure 5.54, the trend of variation of FIO concentration with time is very similar in all the simulations.

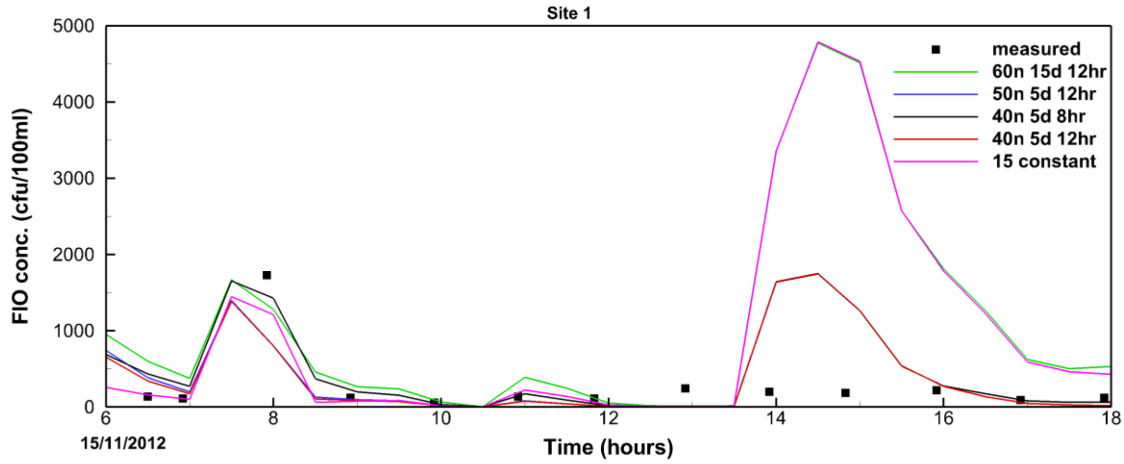

Figure 5.52: Simulated vs. measured comparisons of FIO concentration showing model sensitivity to T_{90} values at Site 1.

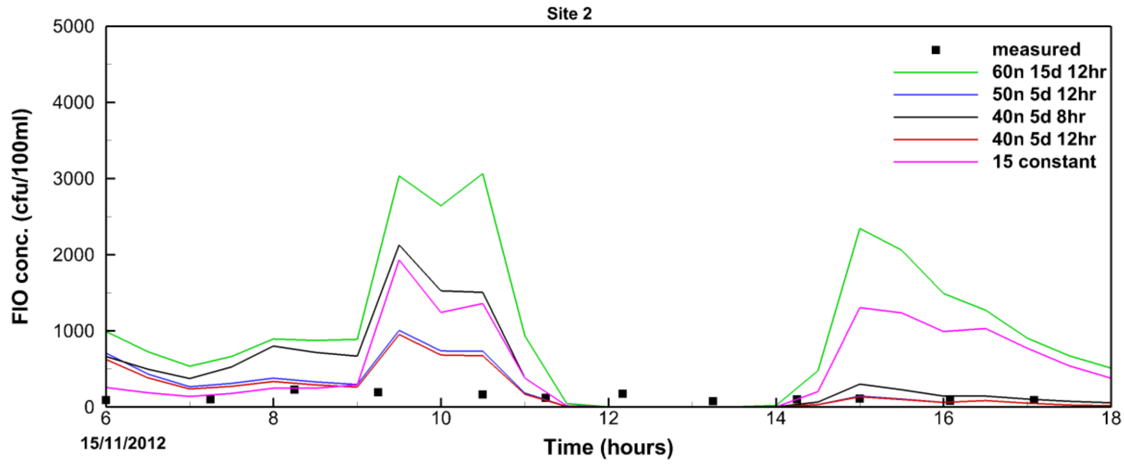

Figure 5.53: Simulated vs. measured comparisons of FIO concentration showing model sensitivity to T_{90} values at Site 2.

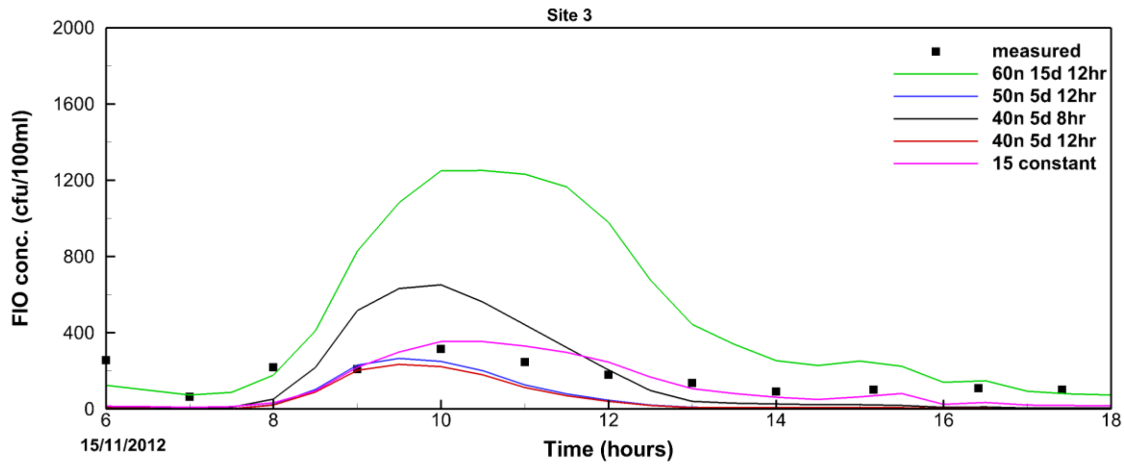

Figure 5.54: Simulated vs. measured comparisons of FIO concentration showing model sensitivity to T_{90} values at Site 3.

Based on the comparisons with measurements, “40n 5d 12hrs” simulation results seem to agree relatively well with the measurements and therefore further calibration runs are performed using various diffusion coefficient values. In particular, simulations using HORCON values of 0.1, 0.4 and 0.8 are performed in addition to the “40n 5d 12hrs” simulation which has a HORCON value of 0.2. The model results from these simulations are illustrated in FiguresFigure 5.55 to Figure 5.57

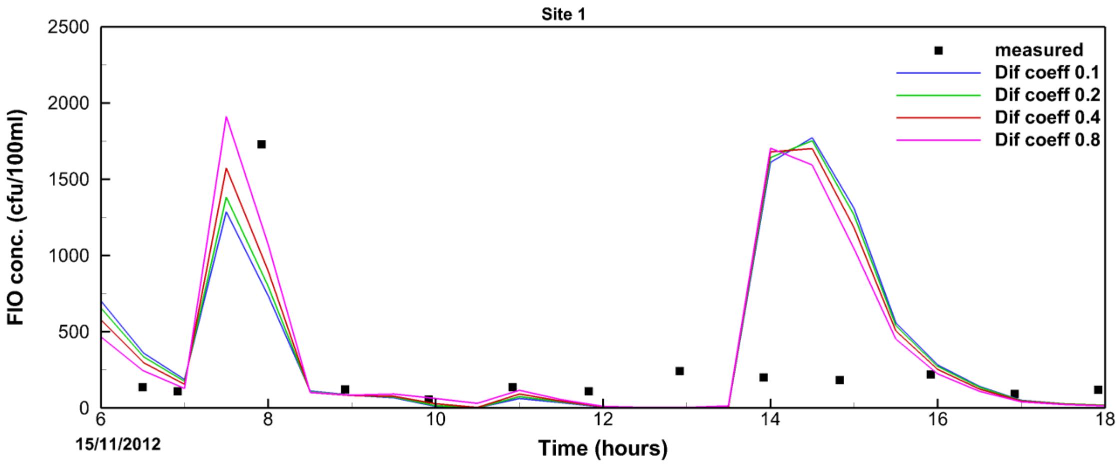

Figure 5.55: Simulated vs. measured comparisons of FIO concentration showing model sensitivity to T_{90} values at Site 1.

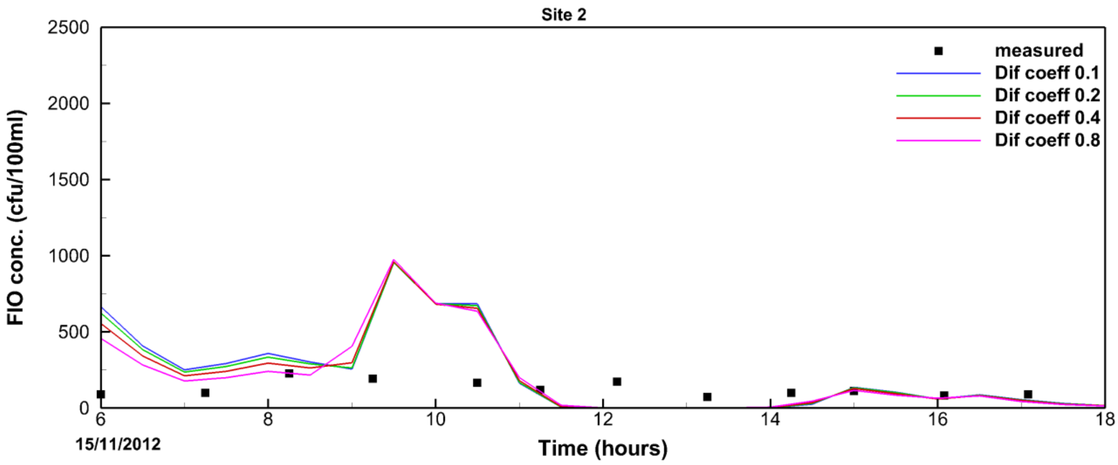

Figure 5.56: Simulated vs. measured comparisons of FIO concentration showing model sensitivity to T_{90} values at Site 2.

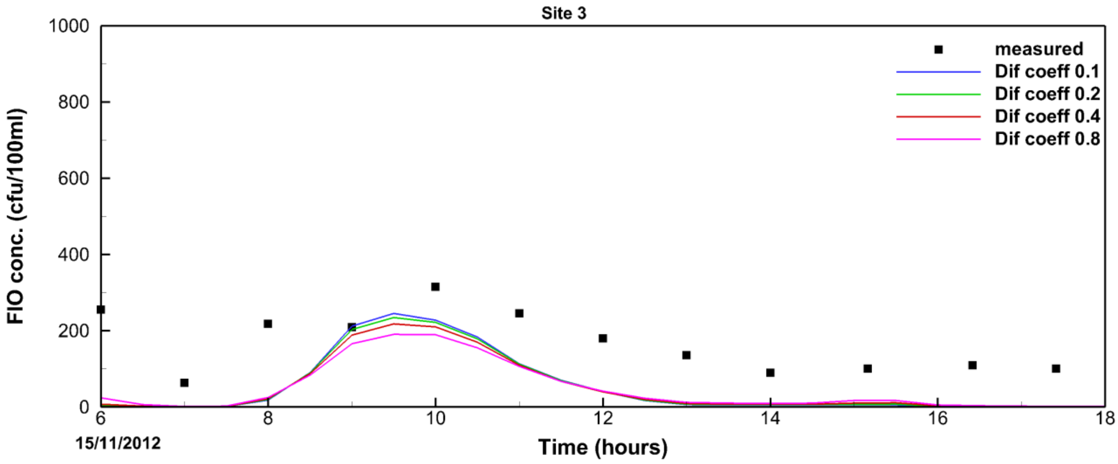

Figure 5.57: Simulated vs. measured comparisons of FIO concentration showing model sensitivity to T_{90} values at Site 3.

It can be clearly seen from the figures that the variability of FIO concentration with various diffusion coefficient values used in the model is much lower than that observed with various T_{90} values. The FIO concentration variability is highest for Site 1 and much lower for Sites 2 and 3. It can be observed that increase in diffusion coefficient does not necessarily influence the FIO concentration values at a time or at a location. For example, at Site 1, the peak in FIO concentration observed at approximately 8hrs increases with increasing diffusion coefficient values; however, the peak observed at approximately 14hrs do not vary with varying diffusion coefficient values. For Site 3, the FIO concentration values seem to decrease with increasing diffusion coefficient values.

Figure 5.58 shows the comparison of model predicted FIO concentrations using the selected simulation (40n 5d 122 hrs, HORCON value of 0.4) against field measurements at Site 1.

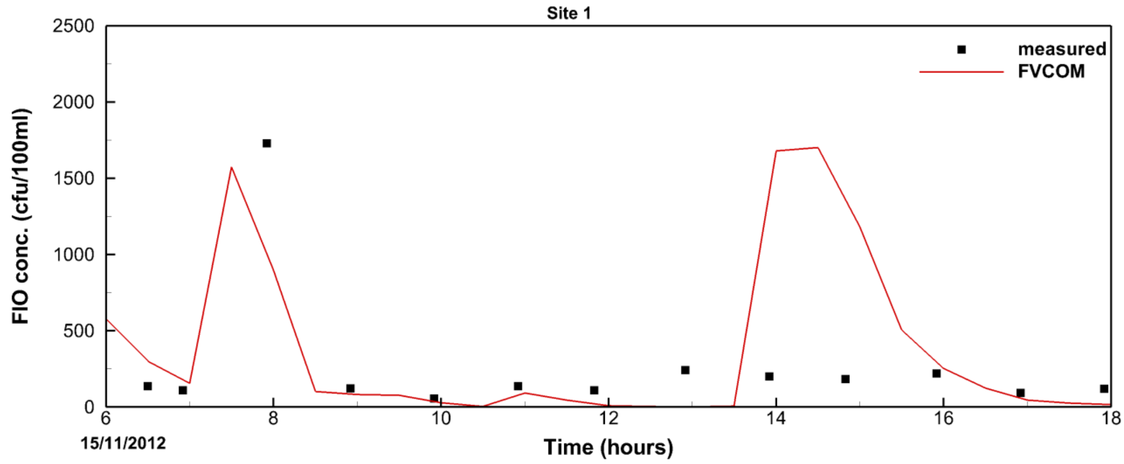

Figure 5.58: Simulated vs. measured FIO concentrations at Site 1.

It can be observed from the figure that the model results agree reasonably well with the measurements during the morning of 15/11/2012 until noon. In particular, the peak in FIO concentration at approximately 8hrs observed in the field is well predicted by the model. While the measured concentration values remain relatively constant following the peak, the model results predict another peak in FIO concentration values at approximately 14hrs. Overall, the calculated RMSE value between model-predicted and measured FIO concentrations at Site 1 is 518cfu/100ml. In order to investigate the reasons behind the observed “double peaks” in the model and the discrepancies between simulated vs. measured FIO concentration values, spatial distribution of FIO concentration values are visualised at approximately 8hrs (which corresponds to 0.5hrs after HW on the day) and 14hrs (which corresponds to 1hr after LW on the day) in Figure 5.59 and Figure 5.60 respectively. Also plotted in the figures are locations of Sites 1, 2 and 3 were comparisons are performed against field measurements.

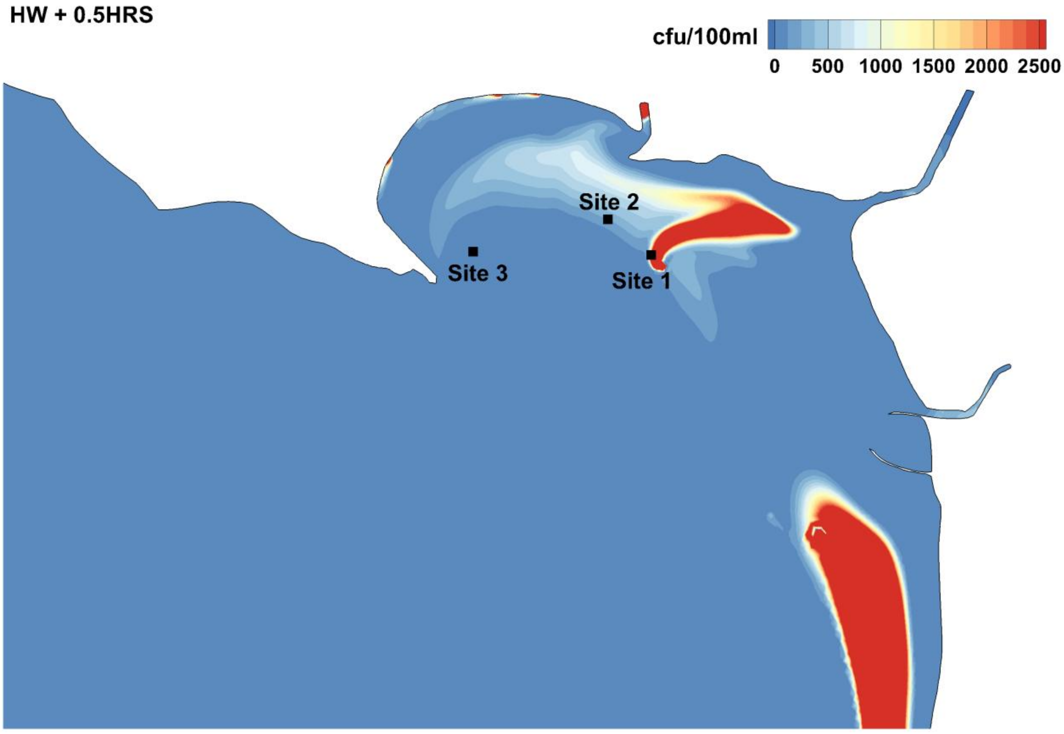

Figure 5.59: Contours of FIO concentration at approximately half an hour after high water at Swansea Bay

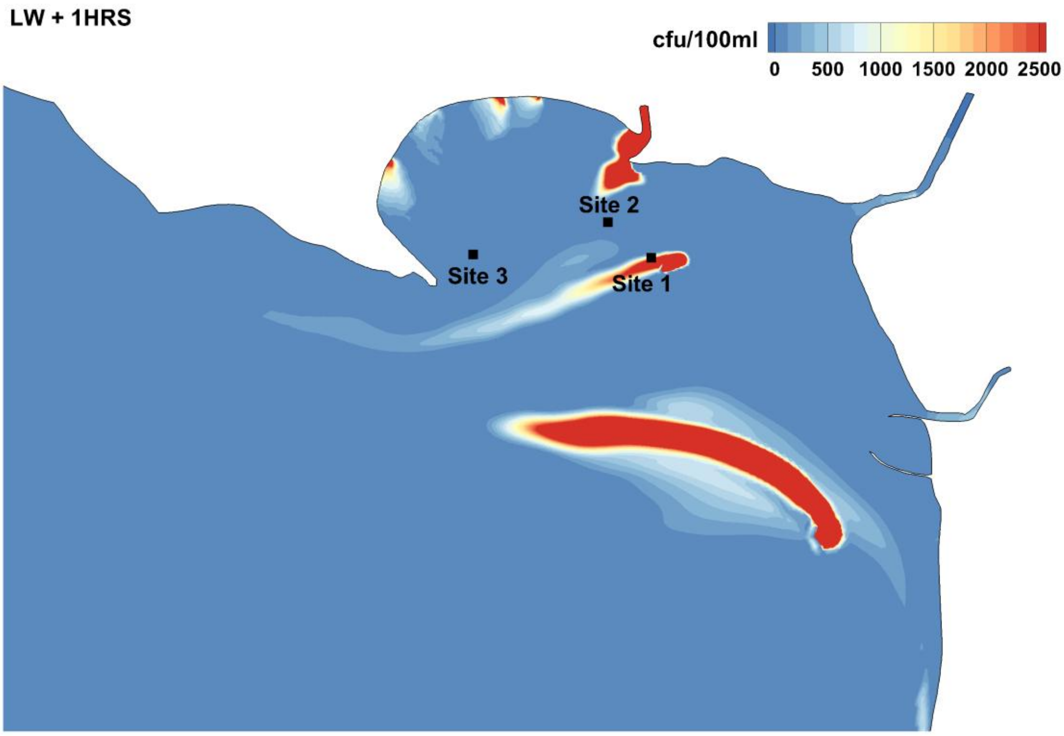

Figure 5.60: Contours of FIO concentration at approximately one hour after low water at Swansea Bay

It can be clearly observed from the figures that due to the near proximity of Site 1 to the Swansea offshore sewage effluent release point, the FIO concentrations at this location could be dependent on various factors like the time of tide, direction of currents, dispersion processes and magnitude and direction of effluent discharges. Figure 5.59 indicates that peak in concentration observed at approximately 8hrs is because of the change in the direction of the plume occurring as a result of change in the tide direction from flood to ebb shortly after HW. The peak seams to occur exactly at a time instant when the direction of plume is predominantly towards Site 1. Similar observations can be made in Figure 5.60, the peak in concentration observed at approximately 14hrs is because of the change in the direction of the plume occurring as a result of change in the tide direction from ebb to flood shortly after LW. However, this second peak is not visible in the field measurements suggesting that the model incorrectly predicts the direction of currents and consequently the direction of the plume at that particular time of the day. It is believed that wind, which is not currently represented in the model, would have significantly influenced current direction in the field at that particular time of the day causing the plume to divert away from Site 1. However, due to the availability of measurements only for one particular day, it cannot be fully established whether wind is the major factor that caused the discrepancies in simulated vs. measured FIO concentration values.

Figure 5.61 shows the comparison of model predicted FIO concentrations against field measurements at Site 2.

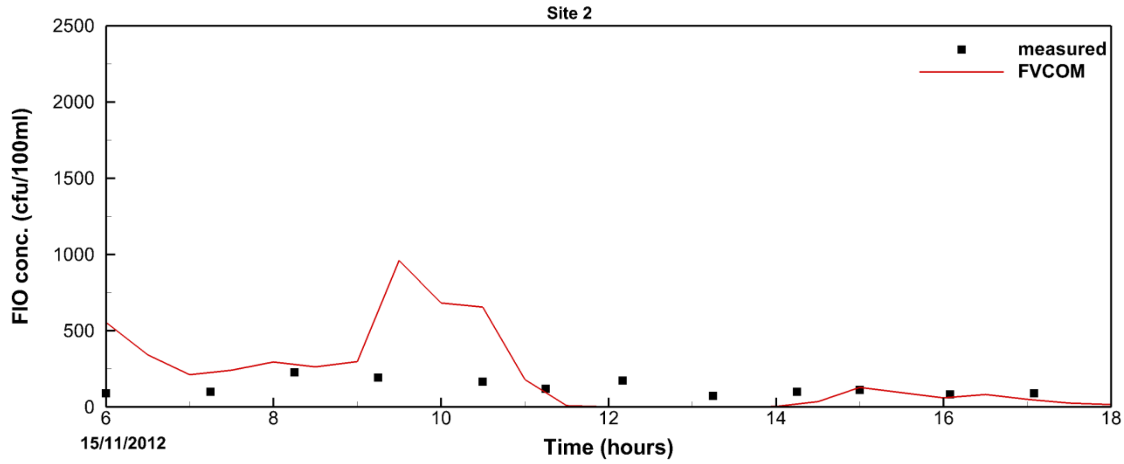

Figure 5.61: Simulated vs. measured FIO concentrations at Site 2.

It can be observed from the figure that the model significantly over-predicts the FIO concentrations at Site 2 in comparison to field measurements during the morning of 15/11/2012. In particular, a peak in FIO concentration is noticeable at approximately 10hrs in the model results but not in the field measurements. The FIO concentrations are under-predicted following the peak but recover well towards the end after 15hrs. Overall, the calculated RMSE value between model-predicted and measured FIO concentrations at Site 2 is 240cfu/100ml. In order to investigate the reasons behind the observed peak in the model predictions at 10hrs and the discrepancies between simulated vs. measured FIO concentration values, spatial distribution of FIO concentration values are visualised at approximately 10hrs (which corresponds to 2.5hrs after HW on the day) in Figure 5.62.

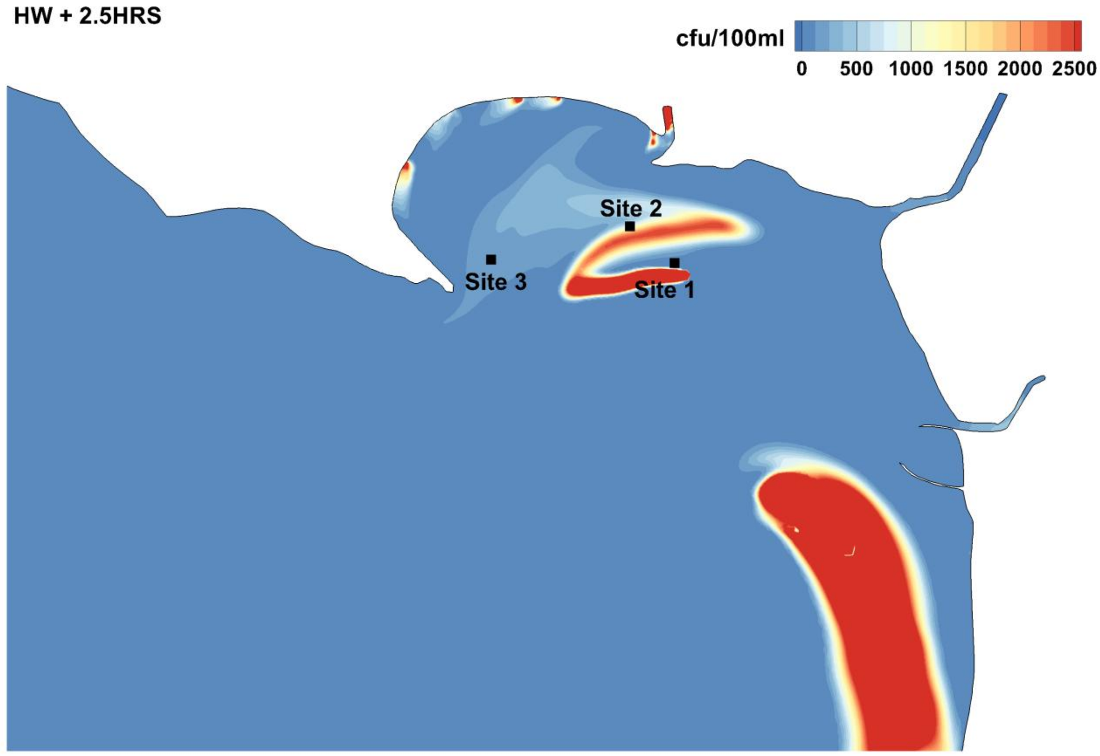

Figure 5.62: Contours of FIO concentration at approximately two and half hours after high water at Swansea Bay

It can be observed from the figure that approximately 2.5 hours after HW the direction of offshore sewage effluent plume is partially along the outgoing tide direction. The peak in FIO concentrations observed in the model predictions seem to be due to the presence of the plume's wake as the plume changes its direction from east to west following HW. The lack of such a peak in FIO concentrations in the field measurements suggests that either the model incorrectly predicts the wake characteristics of the plume or wind would have significantly influenced current direction in the field at that particular time of the day causing the plume to move away from Site 2.

Figure 5.63 shows the comparison of model predicted FIO concentrations against field measurements at Site 3.

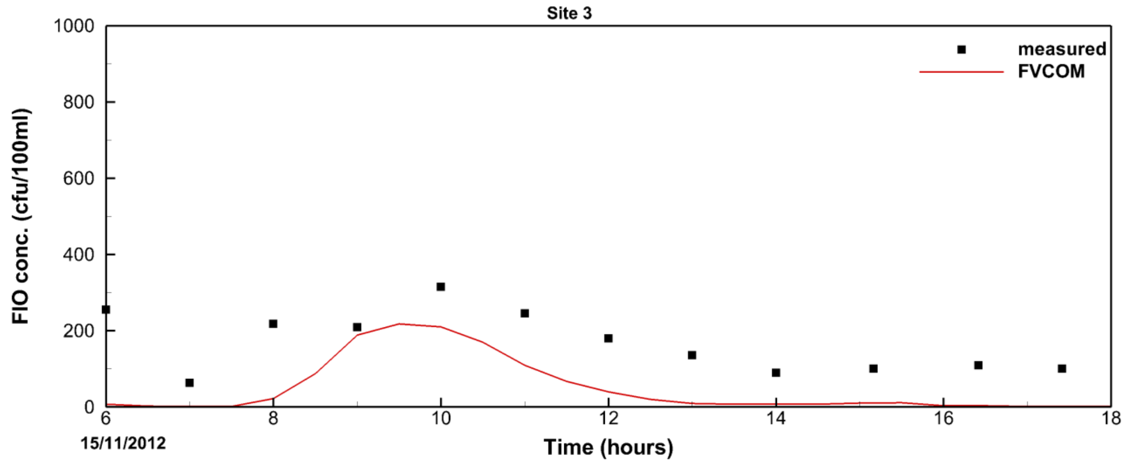

Figure 5.63: Simulated vs. measured FIO concentrations at Site 3.

The calculated RMSE value between model-predicted and measured FIO concentrations at Site 3 is 114cfu/100ml. The discrepancies between predicted and observed FIO concentrations can be associated with the bacteria decay rates used for model calculations. Previous studies (e.g. Kashefipour *et al.* 2002) have suggested that many factors like solar radiation, water temperature, salinity etc. influence the decay rate during a day. In this study, different decay rates have been used for day and night times to take into account the influence of solar radiation on bacterial decay. This assumption is appropriate for model calculations over a large time-period, but within day changes to bacteria decay rates cannot be represented well. It is believed that the observed differences in predicted vs. measured FIO concentrations at Site 3 is due to such variation during the day in the field that are not represented in the model. In addition, the discrepancies can also be associated with sediment-bacteria interaction processes that are not included in the model. Bacteria adsorbed onto sediments can influence FIO concentrations in the water column during deposition / re-suspension processes. Such processes could be expected at Site 3 due to its proximity to Mumbles Head, a location where flow separation significantly influences sediment distribution characteristics as shown in the study of Ferentinos and Collins (1979).

5.5.3 Spatial-temporal variability of FIO

According to the EU's revised Bathing Water Directive, bathing water sites are required to collect water samples every week during the bathing season for compliance monitoring. The samples are to be collected at a designated sampling point where most bathers are expected or where the greatest risk of pollution is expected. For Swansea Bay, approximately 20 samples are collected at the DSP (location shown in Figure 5.1) in the 20 week bathing season and evaluation of water quality is performed against the EU's microbiological standards. Recently, intensive sampling at the DSP was performed as a part of the Smart Coasts project; as described in Section 5.2.2, approximately 20 samples per day were collected 3 times a week over a 5 month period. The number of samples collected per day is equivalent to those collected in the entire bathing season for Swansea Bay. This data can be utilised to understand the small-scale temporal variability of FIO concentrations which the compliance monitoring programmes fail to capture. However, numerical simulations are performed in this study for a comprehensive evaluation of FIO spatial-temporal variability at Swansea Bay as data can be extracted from the model at several locations near the DSP and at a chosen temporal resolution. Specifically, the numerical simulations are conducted for 80 days between 12/07/11 and 29/09/11 and model data is extracted every day at a 30 min interval for the entire Swansea Bay region. However, for the purpose of understanding the spatial-temporal variability and for investigating the inadequacy of compliance sampling data, numerical model data at selected locations near the DSP is analysed. Figure 5.64 shows the location of the DSP and transects 1 to 5 along which model data is extracted.

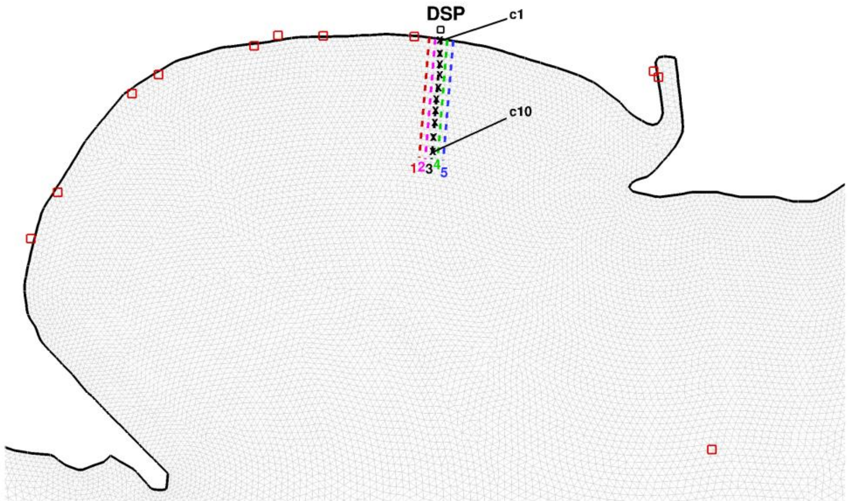

Figure 5.64: Location of the five transects near DSP along which model data is extracted for investigation of spatial-temporal variability of FIO concentrations.

The reason behind selecting transects 1-5 is as follows. Due to the high tidal ranges experienced at Swansea Bay, large regions of Swansea Bay including the DSP are exposed/dry during the low tide and submerged/wet during the high tide. Therefore, water sampling precisely at the DSP is not always possible and measurements are carried out along a cross-shore transect because rBWD mandates that samples are to be collected at locations where there is a minimum water depth of 1m. Transect 3 (T3) is chosen in the present study to roughly represent the direction along which sampling was performed. In view of comparison with field measurements, data from the model is extracted along T3 at ten locations, 'c1' to 'c10', which are 100m apart. Similarly, model data is extracted along transects T1, T2 (west of the DSP) and transects T4, T5 (east of the DSP) to examine the spatial variability of FIO concentrations. The distance between transects is chosen to be approximately 50m.

Figure 5.65 shows the comparison of model-predicted vs. measured FIO concentration values at the DSP. The model data plotted in the figure is an overlap of FIO concentrations at 10 locations ('c1' to 'c10') along T3 for the entire simulation period excluding the 2 days of ramping period, i.e., 78 days at half-hourly time intervals. The measured data plotted in Figure 5.65 is a temporal geometric mean of FIO concentration values measured in all the samples collected in a day. As field sampling was performed only 3 times during a week, approximately 35 days of measurement data within the 78-day simulation period is available and plotted in Figure 5.65.

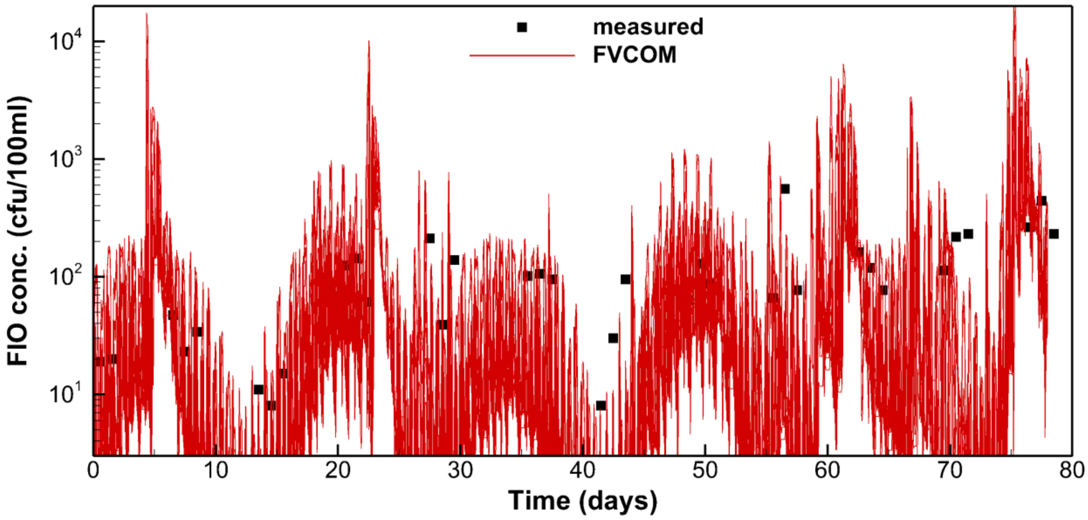

Figure 5.65: Red lines correspond to simulated FIO concentration values obtained from all points along Transect 3; Black dots correspond to measured temporal geometric mean of FIO concentrations at the DSP.

It can be observed from Figure 5.65 that the model-predicted FIO concentration values vary spatially between 'c1' to 'c10' along the transect T3 and temporally during a day. It appears that for most days the measured temporal geometric mean values fall within the range of model-predicted FIO concentrations. The overall model-predicted FIO concentration variation with respect to time appears to follow a sinusoidal pattern with crests and troughs occurring approximately every 15 days. While this variation is visible in the measured data for most days (e.g. between days 0 to 25, days 35, 50 and 65), intermittent peaks in FIO concentrations not very well captured by the model can be observed for certain days (e.g. days 28, 42, 58 and 72). The sinusoidal variation in FIO concentrations can be attributed to the spring and neap tides that occur approximately every 15 days. This can be appreciated in Figure 5.66 where water levels are plotted for the entire simulation period at a selected location in the bay (location 'c10' on transect T3 indicated in Figure 5.60).

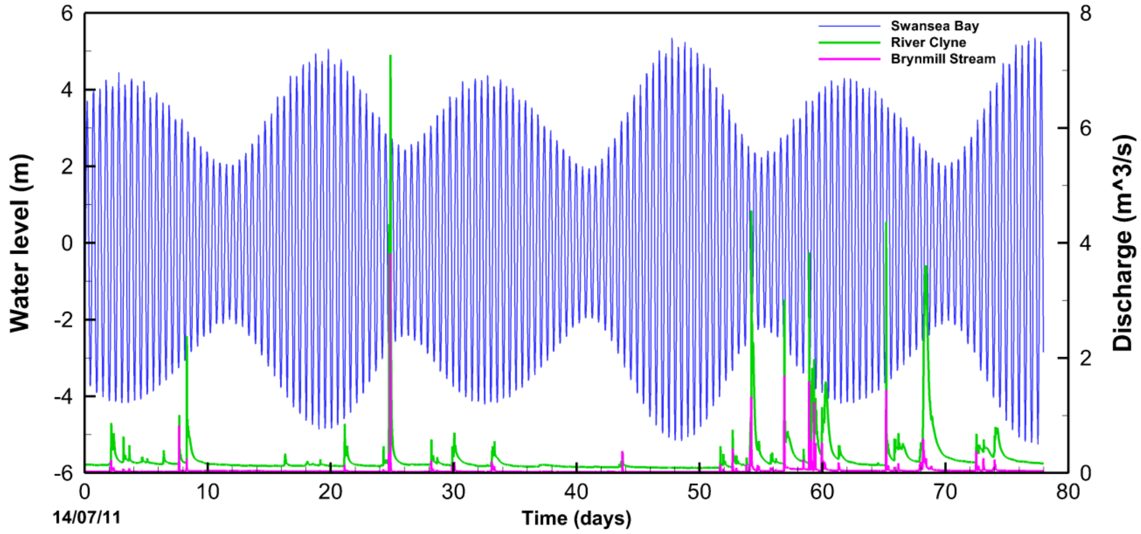

Figure 5.66: Time series of water levels, discharge values in River Clyne and Brynmill Stream at Swansea Bay for the simulation period.

Also plotted in Figure 5.66 are measured flow discharges from River Clyne and Brynmill Stream which flow nearby the DSP. Rainfall events indicated by the peaks in flow discharges in Figure 5.66 seem to have contributed towards the intermittent peaks in measured FIO concentrations in Figure 5.65. A comparison of both figures indicates that the intermittent peaks in measured FIO concentrations seem to occur around the same time as the rainfall events. The intermittent peaks in FIO concentrations are not very well predicted by the model possibly because of the non-physical representation of streams as point sources in the model. Moreover, insufficient grid resolution can also introduce numerical diffusion thereby reducing the pollutant levels at locations away from the sources, such as at the DSP.

Figure 5.67 presents the temporal geometric mean (GM) values of FIO concentrations along the transect T3 as obtained from the model. Also plotted in the figure are GM values obtained from measurements. It is to be noted that for the measurements, temporal GM values were calculated based on FIO concentrations of samples extracted at a selected location which varies along transect T3 depending on the time of tide and depth of water. However, for the model, temporal GM values are calculated using the FIO concentration values for each location along transect T3 separately (shown as thinner lines in different colours on the background in Figure 5.67) and then arithmetic average of the GM values obtained from all the 10 locations is performed (shown as thicker red line in Figure 5.67).

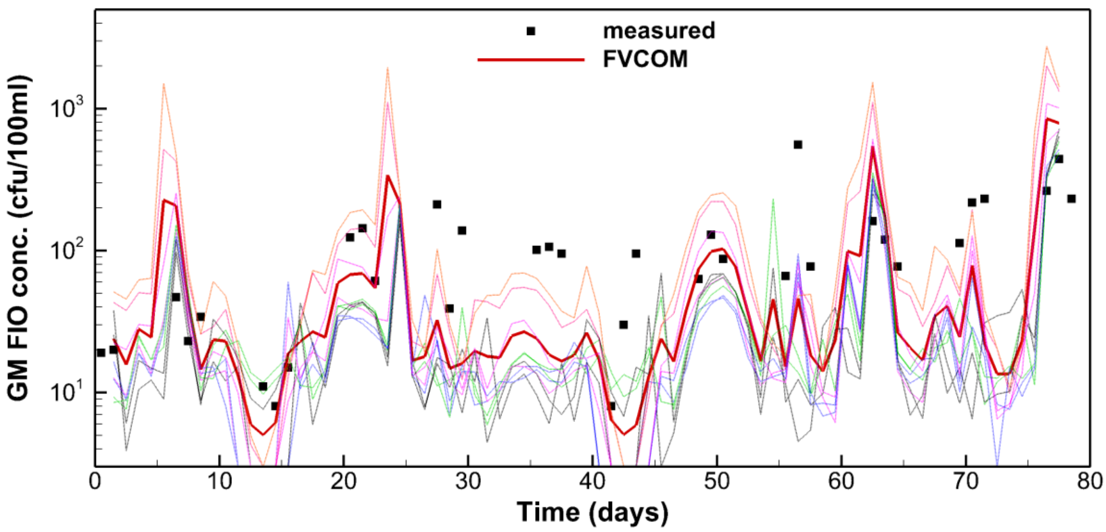

Figure 5.67: Lighter lines correspond to simulated temporal geometric mean of FIO concentration values obtained from all points along Transect 3; Red line corresponds to arithmetic average of all the lighter lines; Black dots correspond to measured temporal geometric mean of FIO concentrations at the DSP.

The spatial variability of FIO concentrations along the transect T3 is clearly visible in Figure 5.67. Depending on the location ('c1' to 'c10') along T3, the model-predicted GM of FIO concentrations vary by a factor of up to 5. Such variability could influence the rating of water quality at the Swansea Bay bathing water site because samples collected at 100-150m distance apart could either comply or fail to comply with the water quality standards. In view of further investigating the cross-shore (along T3) spatial variability, time-series of FIO concentration values at 4 locations are extracted for two selected days. Figure 5.68 and Figure 5.69 correspond to model-data extracted on 19/07/11 and 02/09/11 respectively at four locations 'c1', 'c3', 'c5', and 'c7'.

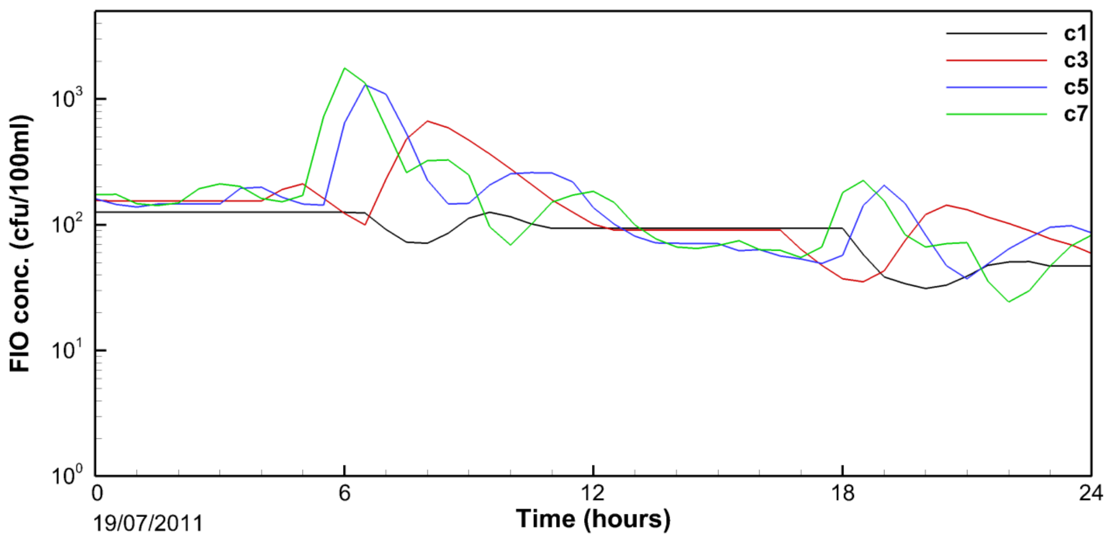

Figure 5.68: Simulated FIO concentration values at four locations on transect 3 corresponding to 19/07/11.

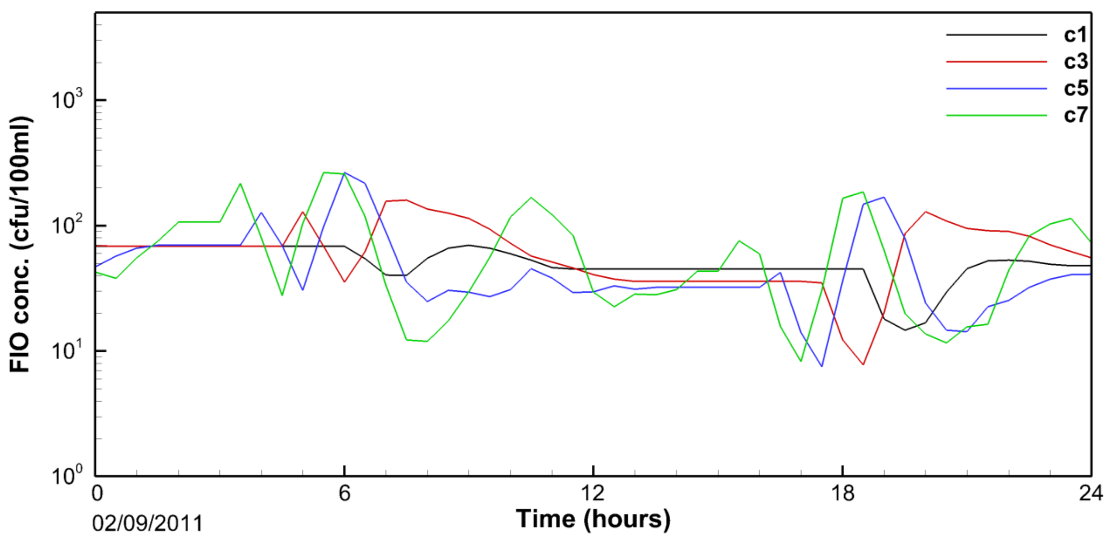

Figure 5.69: Simulated FIO concentration values at four locations on transect 3 corresponding to 02/09/11.

The variability of FIO concentrations with respect to time and space can be observed from the figures. Firstly, it can be noticed that concentration values are similar for certain periods of time but vary over the remaining period. This is because as tides rise and fall, each of these locations are either exposed or submerged resulting in fixed values (due to absence of transport processes) or time-varying values of FIO concentration respectively. Since the bathymetry is different at all the 4 locations, the time durations for which each of the locations are either exposed or submerged varies. For example, in Figure 5.68, concentration values at location 'c1' are approximately constant during 12AM to 6AM and 12PM to 6PM when the cumulative water depth (mean water depth (-1.5m) + instantaneous water level) falls below zero and the location 'c1' is exposed. However, at location 'c3' which is located 200m away, the concentration values are constant (i.e. cumulative depth falls below zero) for a smaller time period during 12AM to 4AM and 1PM to 5PM because mean water depth at 'c3' is 2m and differs to 'c1' by 3.5m.

Such variability of FIO concentration values with time and location can have significant implications to the rating of water quality at Swansea Bay bathing water site. For example, if a sample for compliance monitoring is collected at location 'c3' at 6AM, the FIO concentration value on 19/07/11 (Figure 5.68) would approximately be 130cfu/100ml. However, at 8AM the value would approximately be 650cfu/100ml, i.e., five times higher than the sample collected at 6AM. Similarly, if a sample is collected at location 'c5' at 6:30AM the FIO concentration value would approximately be 1250cfu/100ml, whereas, at 8:30AM the value would approximately be 150cfu/100ml, i.e., more than nine times lower than the 6:30AM sample. Similar observations can be made from FIO concentration values at these locations on 02/09/11 (Figure 5.69). The temporal variability of FIO concentration values can vary up to 10 times. The variability seems to be the highest at locations farthest from the shore.

Overall, it can be seen from Figure 5.68 and Figure 5.69 that there is a strong temporal variability of FIO concentrations within a day at Swansea Bay bathing water site. Therefore, it is important for compliance monitoring programmes to consider this variability as weekly single sample measurements are obviously inadequate and could lead to incorrect assessment of water quality at bathing water sites. Moreover, the cross-shore (along transect) spatial variability observed in this study indicates that the time of tide and cumulative water depth are important factors which can influence the FIO concentration values.

In view of further investigating the spatial variability of FIO concentrations at the Swansea Bay DSP, model-predicted FIO concentrations at four locations (‘c1’, ‘c3’, ‘c5’, and ‘c7’) along all the five transects (T1 to T5) are compared. Figure 5.70 and Figure 5.71 show the comparisons for 19/07/11 and 02/09/11 respectively.

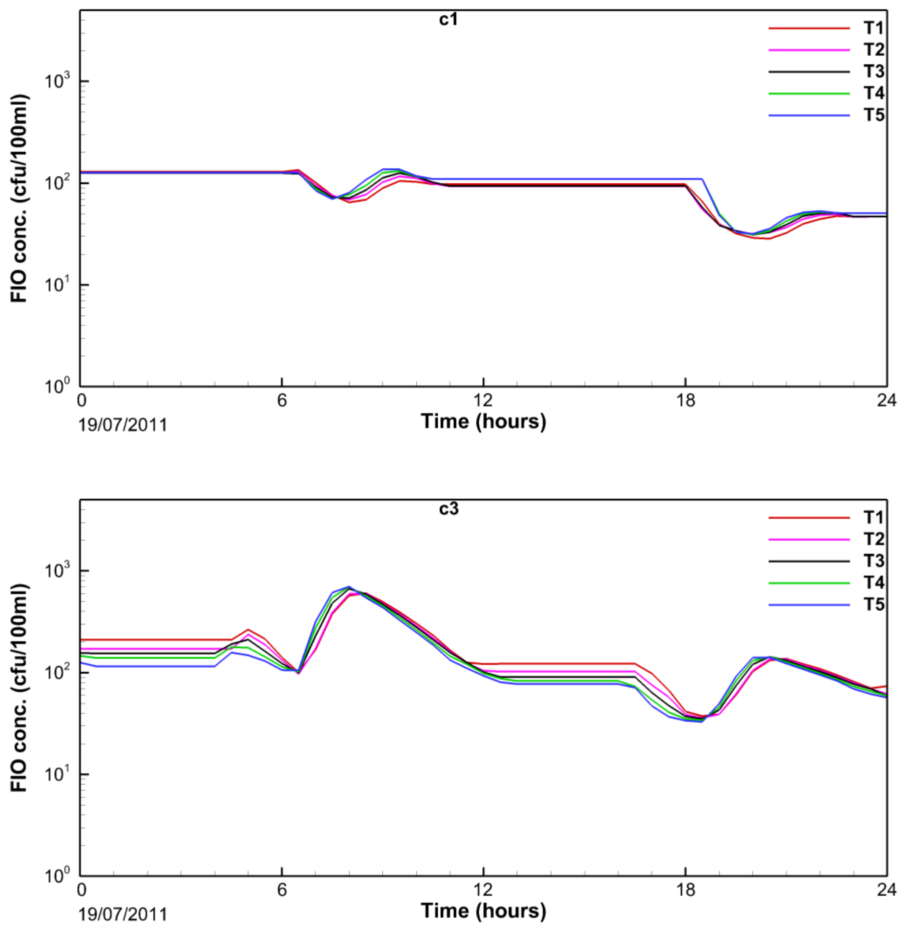

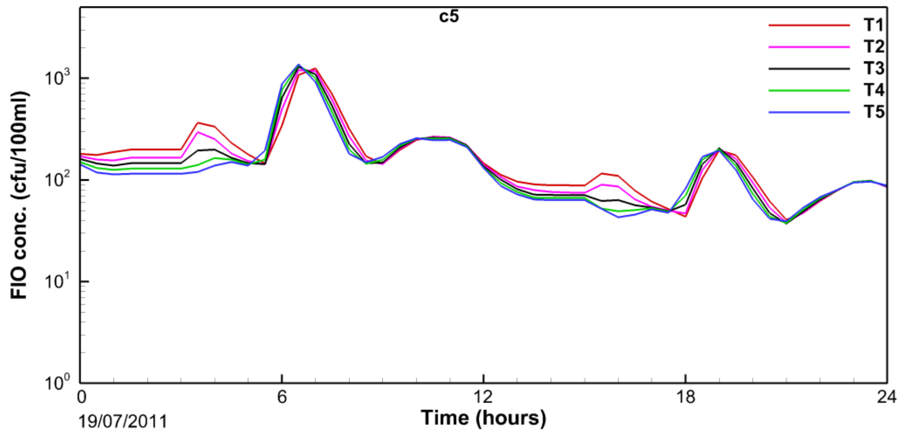

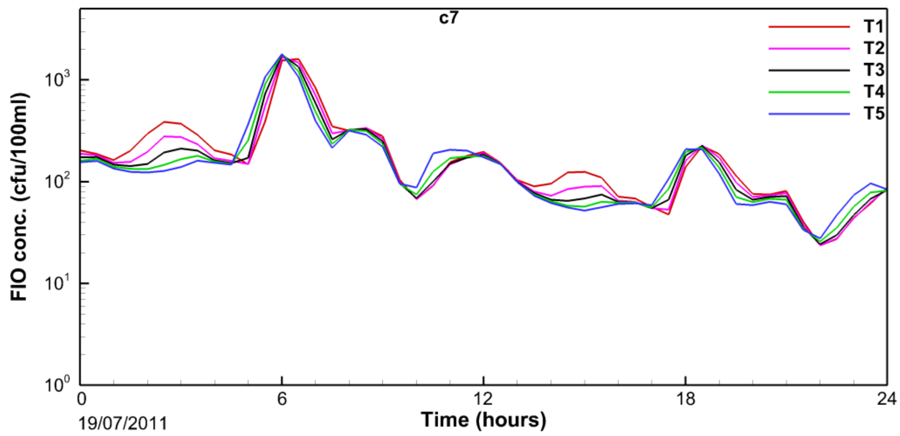

Figure 5.70: Simulated FIO concentrations at four locations (c1, c3, c5, c7) along all transects (T1 to T5) corresponding to 19/07/2011.

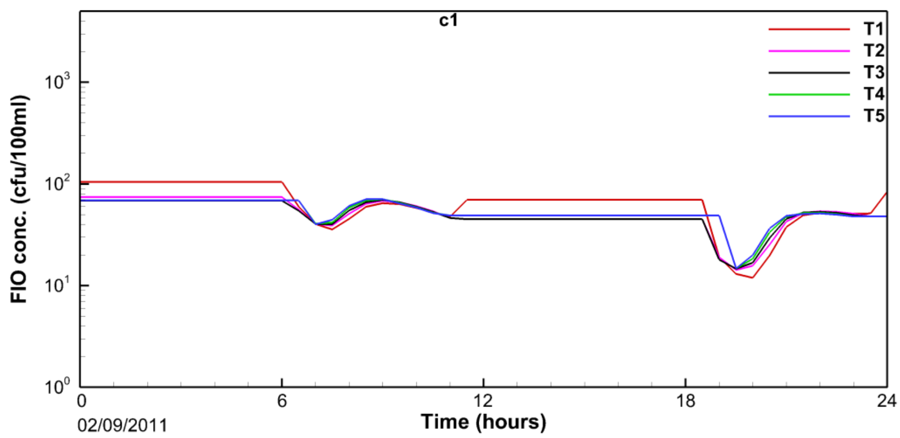

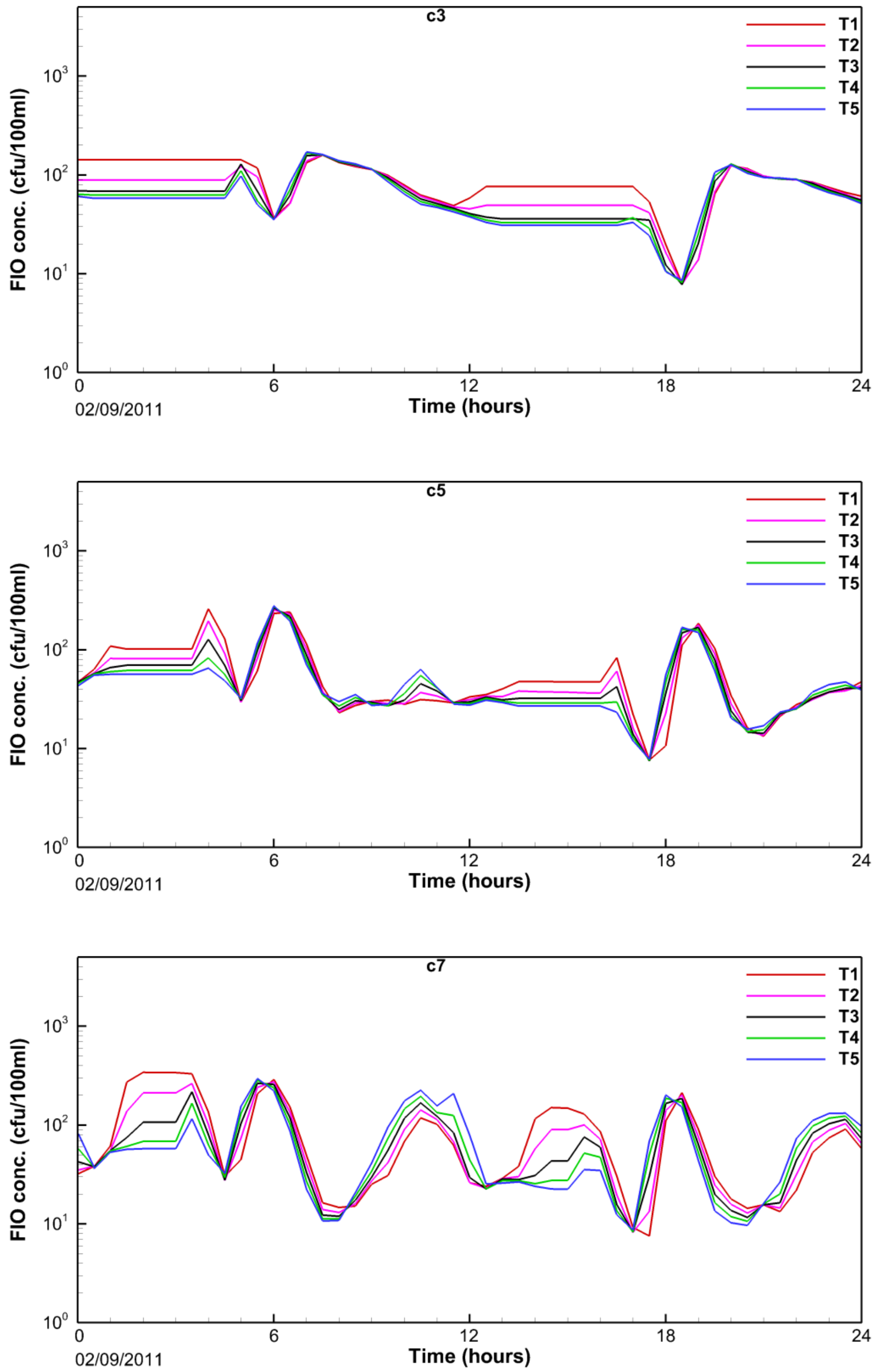

Figure 5.71: Simulated FIO concentrations at four locations (c1, c3, c5, c7) along all transects (T1 to T5) corresponding to 02/09/2011.

It can be observed from Figure 5.70 and Figure 5.71 that at location ‘c1’ the FIO concentration values are similar for all the five transects, suggesting that the along-shore spatial variability of FIO concentration is negligible at this location. Moreover, with location ‘c1’ being the closest to the DSP, it suggests that the samples collected at DSP for compliance monitoring would correctly represent the pollution levels in the surrounding areas. However, this is true only when location ‘c1’ is submerged and has a minimum water depth of 1m for sample collection as mandated in rBWD. This is because during low tide when location ‘c1’ is exposed or have insufficient water depth, the samples collected at further off-shore locations like ‘c3’ and ‘c5’ exhibit significant along-shore spatial variability of FIO concentrations. For example, at location ‘c5’ in Figure 5.70 the FIO concentration values for a sample collected on transect T1 at 6AM would measure 350cfu/100ml, whereas, on T5 the value would approximately be 900cfu/100ml, i.e., close to three times higher. Similarly, at location ‘c5’ in Figure 5.71 the FIO concentration values for a sample collected on transect T1 at 4AM would measure 240cfu/100ml, whereas, on T5 the value would approximately be 60cfu/100ml, i.e., four times lower. At location ‘c7’ the cross-shore variability of FIO concentrations is even higher as evident from Figure 5.70 and Figure 5.71. For example, at location ‘c7’ in both figures the FIO concentration is the highest for transect T5 and lowest for T1 at 10:30AM, whereas, few hours later at approximately 3PM, the FIO concentration is highest for transect T1 and lowest for T5.

Overall, Figure 5.70 and Figure 5.71 have shown that there is significant along-shore variability of bacteria concentrations at the Swansea Bay DSP. The observations support previous findings that the time of tide and cumulative water depth are important factors which can influence the FIO concentration values. During a high tide when locations ‘c1’ and ‘c3’ are submerged, DSP appears to be a good representative location for sample collection as there is no along-shore variability of FIO concentrations. However, during a low tide when sample collection is performed at locations farther away from the DSP, there is significant along-shore variability with FIO concentrations differing by a factor between 2 and 5 depending on the location. Therefore, it is recommended that extreme caution is needed during sample collection, especially at low tide, for an accurate rating of Swansea Bay bathing water site. In addition, it is recommended that additional samples if possible should be collected along-shore so that a more reasonable average value can be calculated.

5.6 Summary

In this study, an assessment of bathing water quality at Swansea Bay, UK has been performed using the 3D Finite Volume Coastal Ocean Model. For the prediction of tidal flow hydrodynamics at Swansea Bay, the computational domain of the model included regions of the Bristol Channel and the Severn Estuary. In addition, modifications to the coastline geometry at Swansea Bay have been performed to include the rivers Tawe, Neath, and Afan which are some of the major sources of pollution in the bay. The numerical simulations revealed that flow patterns at Swansea Bay significantly differed during incoming and outgoing tides. During the incoming tide, flow separation occurred at Mumbles Head, a headland located towards the southwest end of the bay, resulting in production of re-circulating eddy-like flow patterns. However, no such features were observed during the outgoing tide as currents receded uniformly across the bay.

For a quantitative evaluation of model-predicted tidal flow hydrodynamics, data from field measurements consisting of water levels and currents at five locations in the bay were utilised. It was observed that model-predicted water levels, depth-averaged current magnitude and directions, were in reasonable agreement with field measurements. The modelled current profiles in the vertical direction seem to follow a logarithmic profile which is in accordance with the field measurements. However, close to the water surface the model under-predicts the current speeds in comparison with measurements, which is most likely due to the effects of wind which were not included in the model. In addition to the water levels and current comparisons, evaluation of model-predicted flow patterns was performed using drogue-based field measurements. It was observed that the comparison of simulated vs. observed drogue tracks were satisfactory as the model predicted the flow patterns quite accurately at some locations but poorly at others. The comparison of drogues released at Mumbles Head, revealed the importance of accurate coastline geometry representation in the model. It was observed through additional simulations that shape and size of Mumbles headland significantly influenced the flow re-circulation patterns and consequently the drogue movements.

For the assessment of bathing water quality at Swansea Bay, numerical simulations of fate and transport of bacteria (E. coli) discharged from various pollution sources were performed in this study. The model-predicted contours of bacteria concentrations plotted at different stages of a tidal cycle revealed the magnitude and extent of pollution over the entire bay. In addition to the regions near the offshore sewage outfall, three regions close to the bay were observed to feature significantly high levels of bacteria concentrations. In particular, the model results indicated that pollutant discharges from the surface water outlet at Patti Pavillion could be a major concern to Swansea Bay because of its proximity to the designated sampling point – a location where most bathers are expected in a bathing season. For the purpose of validation, a comparison of model-predicted bacteria concentrations was performed against field measurements obtained at three off-shore locations. It was observed that model results agreed satisfactorily with the measurements. Several calibration simulations revealed that magnitude of bacteria concentrations varied significantly (1-10 times) with the bacteria decay rate (T_{90} values) used in the model. However, the variation of bacteria concentration with time, i.e., the trend was found to be very similar in all the simulations. The variability of bacteria concentrations with respect to the diffusion coefficient values used in the model was found to be minimal.

For the purpose of understanding the spatial-temporal variability of bacteria concentrations, analysis of model data at selected locations near the DSP was performed. In particular, data was extracted at ten locations each along five transects and investigation of the temporal, along-shore and cross-shore spatial variability was conducted. The model results showed that depending on the location along the transect, the temporal geometric mean (GM) of bacteria concentrations varied by a factor of up to five. This finding suggests that the cross-shore variability could influence the rating of Swansea Bay bathing water site because samples collected at 100-200m distance apart could either comply or fail to comply with the water quality standards. Similar to previous studies based on intensive sampling and field surveys, the model results showed significant within-day temporal variability (up to 10 times) at the DSP suggesting that weekly samples collected as a part of compliance monitoring programs could be biased and lead to incorrect rating of bathing water sites. Investigation of bacteria concentrations at locations close to the DSP on the five transects indicated that there is no along-shore spatial variability and that the samples collected at DSP for compliance monitoring would correctly represent the pollution levels in the surrounding areas. However, at locations further off-shore on the transects significant along-shore spatial variability (up to 5 times) was observed suggesting that time of tide and cumulative water depth are important factors influencing the bacteria concentration variability.

Chapter 6

Summary and Conclusions

In this thesis, a hydro-environmental model was utilised to further demonstrate the applicability of computer models to predict flows in coastal waters. In particular, numerical model simulations were performed for two selected sites: the Ogeechee Estuary, located in the State of Georgia, on the south east coast of the United States; and Swansea Bay, located on the south Wales coast of the United Kingdom. The model simulations for the first site, the Ogeechee Estuary, were performed to assess hydro-kinetic energy potential in the estuary and to identify potential sites for power extraction near Rose Dhu Island, a small island in the estuary. The model simulations for the second site, Swansea Bay, were performed to assess faecal coliform levels at the Swansea Bay bathing water site and help sustain the local touristic economy through prevention of beach closures due to non-compliance with regulatory standards.

Although similar studies have been conducted previously, this work is unique in several aspects and also addresses some of the shortcomings of the previous studies. The assessment of energy potential at Rose Dhu Island performed in this thesis serves as a good case study for small scale communities intending to exploit surrounding tidal streams for hydro-kinetic energy. Whilst several studies have been conducted on estuaries along the coast of Georgia, to the author's knowledge, this research study is the first to provide a detailed analysis of tidal flow hydrodynamics in the Ogeechee Estuary. Results from the model simulations revealed that better representation of branching smaller creeks located inshore enhanced the magnitude of tidal currents by approximately 30% near Rose Dhu Island. This highlights the importance of accurate bathymetric interpolation on to the model grid as blockage of narrow channels can occur due to inaccurate interpolation resulting in under-prediction of volume fluxes. The tidal power assessment calculations for Rose Dhu Island showed that the total available kinetic power in the channel ranged from 500 kW during neap tides and up to 2000 kW during spring tides. With a peak power extraction of around 1kW during neap tides and 4kW during spring tides at a location close to the island, it can be expected that power extraction would have little impact on the hydrodynamics of the ecosystem as this is a very small fraction of the total kinetic power (0.2%). Overall, based on the assessment carried out in this study it can be concluded that tidal stream energy is a viable option for renewable energy for the Girl Scouts on Rose Dhu Island.

The investigation of model sensitivity to parameters related to bottom friction and intertidal storage carried out in this study highlighted their influence on tidal asymmetry. In accordance with previous findings, increase in channel friction made the flow less ebb-dominant in the estuary. Increasing the intertidal storage by lowering marsh elevation decreased the ebb-dominance and volume flux asymmetry typically associated with intertidal storage. Therefore the elevation of the marshes rather than the total storage volume has a bigger effect on tidal distortion. Increasing the marsh friction to mimic the resistance offered by marsh vegetation reduced the influence of intertidal storage on tidal distortion; rather than dampening wave propagation, enhanced friction impeded the lateral flooding of marshes causing reduced ebb dominance. These findings related to the influence of bottom friction and intertidal storage on tidal asymmetry can be used by researchers or practitioners to further parameterise tidal distortion in wetlands or to better calibrate numerical models of similar estuarine environments as knowing the sensitivity to various parameters will save time and computational cost.

In regards to the hydro-environmental modelling of flow and transport processes at Swansea Bay performed in this thesis, this is the first study to conduct a detailed assessment of flow hydrodynamics and faecal coliform pollution levels at Swansea Bay bathing water site. The hydrodynamic model simulations revealed that flow patterns at Swansea Bay significantly differed during incoming and outgoing tides. During the incoming tide, flow separation occurred at Mumbles Head resulting in production of re-circulating eddy-like flow patterns. However, no such features were observed during the outgoing tide as currents receded uniformly across the bay. Comparison of simulated vs. measured drogues released at Mumbles Head, revealed the importance of accurate coastline geometry representation in the model. It was observed that shape and size of Mumbles headland significantly influenced the flow re-circulation patterns and consequently the movement of drogues. Overall, based on the observed discrepancies between model results and field measurements of current magnitudes it can be concluded that wind plays a significant role in the hydrodynamics at Swansea Bay and must be included in future modelling studies at this location.

The faecal coliform modelling performed in this study helped identify the major pollution sources that can influence the rating of Swansea Bay bathing water site. The findings can be utilised by the local authorities to develop strategies for systematic reduction of pollution and prevention of beach closures due to non-compliance. Although several faecal coliform modelling studies similar to this study have been conducted previously, to the author's knowledge, this is the first research study to extend the analysis of modelling results to investigate the inadequacy of sampling protocols of compliance monitoring programs. The analysis of model results at the Swansea Bay DSP revealed that there is no significant spatial variability of FIO concentrations at locations close to the shore suggesting that the DSP is a good representative location. However, strong temporal variability (up to 10 times) was observed at the DSP suggesting that weekly samples collected as a part of compliance monitoring programs could be biased and lead to incorrect rating of the bathing water site. The findings from this study related to the spatial-temporal variability of pollutant concentrations at the designated sampling point can be used to assist future sampling strategies and can help prevent incorrect rating of the Swansea Bay bathing water site. For example, when measurements are performed during low tide, samples may be collected at several locations and a spatial average can be performed to minimise the along-shore variability which was found to be very significant at locations away from the DSP.

6.1 Recommendations for future work

1) Although the assessment of hydro-kinetic energy at Rose Dhu Island has provided an estimate of available energy, it is recommended that additional simulations be performed to determine how flow characteristics change in the presence of a turbine and whether the available energy changes significantly at the island.
2) As the present study has identified and characterised tidal asymmetry in the Ogeechee Estuary, this study may be extended to investigate the implications of tidal asymmetry on available hydro-kinetic energy, sediment transport processes, and estuarine flushing times.
3) As field measurements and numerical model data of flow characteristics are available near Rose Dhu Island, the information may be utilised towards a detailed computational fluid dynamics (CFD) study of flow around turbines to test how they perform under such realistic flow conditions.
4) It is recommended that a modelling study be conducted utilising detailed bathymetry data and better coastline representation particularly near Mumbles Head for a better understanding of flow hydrodynamics. It is also recommended that any future modelling studies at Swansea Bay should include the effects of wind.

5) As the present study considers only point sources of pollution, it is recommended that a catchment model be linked to the coastal model to account for all sources of pollution that affect the bathing water quality in Swansea Bay.
6) Finally, similar to existing statistical model based water quality prediction systems, studies focusing on linking hydro-environmental models to real-time information systems may be conducted to provide communities water quality predictions in real-time.

References

Amorim, E., Ramos, S., & Bordalo, A. A. (2014). “Relevance of temporal and spatial variability for monitoring the microbiological water quality in an urban bathing area”, *Ocean & Coastal Management*, 91, 41-49.

Associate British Ports Marine Environment Research (2013). “Swansea Bay Tidal Lagoon Coastal Processes: Model Setup, Calibration and Validation”, *Report*, R.2108TN, http://www.tidallagoonswanseabay.com/environmental-reports.aspx (last accessed 07/06/2014).

Bedri, Z., Bruen, M., Dowley, A., & Masterson, B. (2011). “A three-dimensional hydro-environmental model of Dublin Bay”, *Environmental Modeling & Assessment*, 16(4), 369-384.

Blanton, J. O., Lin, G., & Elston, S. A. (2002). “Tidal current asymmetry in shallow estuaries and tidal creeks”, *Continental Shelf Research*, 22(11), 1731-1743.

Blumberg, A. F., & Mellor, G. L. (1987). “A description of a three-dimensional coastal ocean circulation model”, *Coastal and estuarine sciences*, 4, 1-16.

Blumberg, A. F. (1994). “A Primer for ECOM-si”, *Technical Report*, HydroQual Inc., Mahwah, New Jersey, 88pp.

Blunden, L. S., & Bahaj, A. S. (2006). “Initial evaluation of tidal stream energy resources at Portland Bill, UK”, *Renewable Energy*, 31(2), 121-132.

Boehm, A. B. (2007). “Enterococci concentrations in diverse coastal environments exhibit extreme variability”, *Environmental science & technology*, 41(24), 8227-8232.

Boon, J. D., & Byrne, R. J. (1981). “On basin hypsometry and the morphodynamic response of coastal inlet systems”, *Marine Geology*. 40, 27–48.

Bougeard, M., Le Saux, J. C., Perenne, N., Baffaut, C., Robin, M., & Pommepuy, M. (2011). “Modeling of Escherichia coli Fluxes on a Catchment and the Impact on Coastal Water and Shellfish Quality1”, *Journal of the American Water Resource Association*, 47(2), 350-366.

Bryden, I. G., Grinsted, T., & Melville, G.T. (2004). "Assessing the potential of a simple tidal channel to deliver useful energy", *Applied Ocean Research*. 26(5), 198-204.

Bryden, I., & Melville, G. T. (2004). “Choosing and evaluating sites for tidal current development”, *Proceedings of the Institution of Mechanical Engineers, Part A: Journal of Power and Energy*, 218(8), 567-577.

Carballo, R., Iglesias, G., & Castro, A. (2009). “Numerical model evaluation of tidal stream energy resources in the Ría de Muros (NW Spain)”, *Renewable Energy*, 34(6), 1517-1524.

Charlier, R. H. (2003). “A sleeper awakes: tidal current power”, *Renewable and Sustainable Energy Reviews*, 7(6), 515-529.

Chen, C., Liu, H., & Beardsley, R. C. (2003). “An unstructured grid, finite-volume, three-dimensional, primitive equations ocean model: application to coastal ocean and estuaries”, *Journal of Atmospheric & Oceanic Technology*, 20(1).

Chick, H., (1910). “The process of disinfection by chemical agencies and hot water”, *Journal of Hygiene*, 10, 237-286.

Dame, R., Alber, M., Allen, D., Mallin, M., Montague, C., Lewitus, A., Chalmers, A., Gardner, R., Gilman, C., & Kjerfve, B., (2000), “Estuaries of the south Atlantic coast of North America: their geographical signatures”, *Estuaries,* 23(6), 793-819.

Defne, Z., Haas, K. A., & Fritz, H. M. (2011a). “GIS based multi-criteria assessment of tidal stream power potential: A case study for Georgia, USA”, *Renewable and Sustainable Energy Reviews*, 15(5), 2310-2321.

Defne, Z., Haas, K. A., & Fritz, H. M. (2011b). “Numerical modeling of tidal currents and the effects of power extraction on estuarine hydrodynamics along the Georgia coast, USA”, *Renewable Energy*, 36(12), 3461-3471.

Draper, S., Adcock, T. A., Borthwick, A. G., & Houlsby, G. T. (2014). “Estimate of the tidal stream power resource of the Pentland Firth”, *Renewable Energy*, 63, 650-657.

Dronkers, J. (1986). “Tidal asymmetry and estuarine morphology”, *Netherlands Journal of Sea Research*, 20(2), 117-131.

DTI (2004). “Atlas of UK marine renewable energy resources”, *Technical report*, ABP Marine Environmental Research.

EPRI (2006). “Methodology for Estimating Tidal Current Energy Resources and Power Production by Tidal In-Stream Energy (TISEC) Devices”, *Technical Report*, EPRI-TP-001-NA-Rev-3

Energy Technology Support Unit (ETSU), 1993. “Tidal stream energy review”, *Technical report ETSU-T-05/00155/REP*, DTI Report, Harwell Laboratory.

European Commission (EC), 1996. “The exploitation of tidal and marine currents, wave energy, project results”, *Technical report EUR 16683 EN*, Commission of the European Communities,Directorate - General for Science, Research and Development.

Falconer, R. A., & Chen, Y. (1991). “Improved representation of flooding and drying and wind stress effects in a two-dimensional tidal numerical model”, *Proc. Inst. Civil. Eng. Part 2 Res Theory*, 91, 659-678.

Falconer, R. A., & Lin, B. (1997). “Three-dimensional modelling of water quality in the Humber Estuary”, *Water Research*, 31(5), 1092-1102.

Ferentinos, G., & Collins, M. (1979). “Tidally induced secondary circulations and their associated sedimentation processes”, *Journal of the Oceanographical Society of Japan*, 35(2), 65-74.

Friedrichs, C. T., & Aubrey, D. G. (1988). “Non-linear tidal distortion in shallow well-mixed estuaries: a synthesis”, *Estuarine, Coastal and Shelf Science*. 27, 521–545.

FWR (1993). “A Framework for marine and estuarine model specification in the UK”, *Report*, No FR0374, Foundation for Water Research.

Garrett, C., & Cummins, P. (2005). “The power potential of tidal currents in channels”, *Proceedings of the Royal Society A: Mathematical, Physical and Engineering Science*, 461(2060), 2563-2572.

Ge, Z., Whitman, R. L., Nevers, M. B., Phanikumar, M. S., & Byappanahalli, M. N. (2012). “Nearshore hydrodynamics as loading and forcing factors for Escherichia coli contamination at an embayed beach”, *Limnology and Oceanography*, 57(1), 362.

Grabbe, M., Lalander, E., Lundin, S., & Leijon, M. (2009). “A review of the tidal current energy resource in Norway”, *Renewable and Sustainable Energy Reviews*, 13(8), 1898-1909.

Haas, K. A. (2011). “Assessment of energy production potential from tidal streams in the United States”, *DOE/GO/1817-8*. Georgia Tech Research Corporation.

Haidvogel, D. B., Arango, H. G., Hedstrom, K., Beckmann, A., Malanotte-Rizzoli, P., & Shchepetkin, A. F. (2000a). “Model evaluation experiments in the North Atlantic Basin: simulations in nonlinear terrain-following coordinates”, *Dynamics of Atmospheres and Oceans*, 32(3), 239-281.

Haidvogel, D. B., Blanton, J., Kindle, J. C., & Lynch, D. R. (2000b). “Coastal ocean modeling: processes and real-time systems”, *Coastal Ocean Modelling Special Issue*, 13(1), 35-46.

Hamrick, J. M. (1992). ‘‘A three-dimensional environmental fluid dynamics computer code: Theoretical and computational aspects.’’ Special Paper 317, The College of William and Mary, Virginia Institute of Marine Science, Williamsburg, Va.

Harris, E. L., Falconer, R. A., & Lin, B. (2004). “Modelling hydroenvironmental and health risk assessment parameters along the South Wales Coast”, *Journal of environmental management*, 73(1), 61-70.

Hartnett, M., Nash, S., & Olbert, I. (2012). “An integrated approach to trophic assessment of coastal waters incorporating measurement, modelling and water quality classification”, *Estuarine, Coastal and Shelf Science*, 112, 126-138.

Huang, H., Chen, C., Blanton, J. O., & Andrade, F. A. (2008). “A numerical study of tidal asymmetry in Okatee Creek, South Carolina”, *Estuarine, Coastal and Shelf Science*, 78(1), 190-202.

Kashefipour, S. M., Lin, B., Harris, E., & Falconer, R. A. (2002). “Hydro-environmental modelling for bathing water compliance of an estuarine basin”, *Water Research*, 36(7), 1854-1868.

Kashefipour, S. M., Lin, B., & Falconer, R. A. (2006). “Modelling the fate of faecal indicators in a coastal basin”, *Water research*, 40(7), 1413-1425.

Kay, D., Jones, F., Wyer, M. D., Fleisher, J. M., Salmon, R. L., Godfree, A. F., Zelenauch-Jacquotte, A., & Shore, R. (1994). "Predicting likelihood of gastroenteritis from sea bathing: results from randomised exposure:, *The Lancet*, 344(8927), 905-909.

Kwasi, O. D., Keith, J., & Nigel, P. (1999). "The effect of the time of sampling on the compliance of bathing water in NW England with the EU Directive on bathing water quality", *Journal of Coastal Conservation*, 5(1), 51-58.

Lapetina, A., & Sheng, Y. P. (2014). Three-Dimensional Modeling of Storm Surge and Inundation Including the Effects of Coastal Vegetation. Estuaries and Coasts, 37(4), 1028-1040.

Lin, B., & Falconer, R. A. (1997). "Three-dimensional layer-integrated modelling of estuarine flows with flooding and drying", *Estuarine, coastal and shelf science*, 44(6), 737-751.

Loder, N. M., Irish, J. L., Cialone, M. A., & Wamsley, T. V. (2009). "Sensitivity of hurricane surge to morphological parameters of coastal wetlands", *Estuarine, Coastal and Shelf Science*, 84(4), 625-636.

Luettich Jr, R. A., Westerink, J. J., & Scheffner, N. W. (1992). "ADCIRC: An Advanced Three-Dimensional Circulation Model for Shelves, Coasts, and Estuaries. Theory and Methodology of ADCIRC-2DDI and ADCIRC-3DL (No. CERC-TR-DRP-92-6)", *Report 1*, Coastal Engineering Research Center, Vicksburg, MS.

Mellor, G. L., & Yamada, T. (1982). "Development of a turbulence closure model for geophysical fluid problems", *Reviews of Geophysics*, 20(4), 851-875.

Mukai, A. Y., Westerink, J. J., & Luettich, R. A. (2002). "Guidelines for using Eastcoast 2001 database of tidal constituents within Western north Atlantic Ocean, Gulf of Mexico and Caribbean sea (No. ERDC/CHL-CHETN-IV-40)". Engineer Research and Development Center, Coastal and Hydraulics lab, Vicksburg, MS.

Neil, S. P., Hashemi, M. R., & Lewis, M. J. (2014). "The role of asymmetry in characterizing the tidal energy resource of Orkney", *Renewable Energy*, 68, 337-350.

Nepf, H. M., & Vivoni, E. R. (2000). "Flow structure in depth-limited, vegetated flow", *Journal of Geophysical Research: Oceans (1978–2012),* 105(C12), 28547-28557.

Nevers, M. B., & Whitman, R. L. (2010). "Policies and practices of beach monitoring in the Great Lakes, USA: a critical review", *Journal of Environmental Monitoring*, 12(3), 581-590.

Parker, B. B. (1991). "Tidal Hydrodynamics", *ed. John Wiley & Sons.*

Pawlowicz, R., Beardsley, B., & Lentz, S. (2002). "Classical tidal harmonic analysis including error estimates in MATLAB using T_TIDE", *Computers & Geosciences*, 28(8), 929-937.

Polagye, B., Malte, P., Kawasel, M., & Durran, D. (2008). "Effect of large-scale kinetic power extraction on time-dependent estuaries", *Proceedings of the Institution of Mechanical Engineers Part A-Journal of Power and Energy*. 222(A5), 471-484.

Sheng, Y. P., Lapetina, A., & Ma, G. (2012). “The reduction of storm surge by vegetation canopies: Three-dimensional simulations”, *Geophysical Research Letters*, 39(20).

Smagorinsky, J. (1963). “General circulation experiments with the primitive equations: I. The basic experiment”, *Monthly weather review*, 91(3), 99-164.

Speer, P. E., & Aubrey, D. G. (1985). “A study of non-linear tidal propagation in shallow inlet/estuarine systems Part II: Theory”, *Estuarine, Coastal and Shelf Science*, 21(2), 207-224.

Sutherland, G., Foreman, M., & Garrett, C. (2007). “Tidal current energy assessment for Johnstone Strait, Vancouver Island”, *Proceedings of the Institution of Mechanical Engineers, Part A: Journal of Power and Energy*, 221(2), 147-157.

Wade, T. J., Pai, N., Eisenberg, J. N., & Colford Jr, J. M. (2003). “Do US Environmental Protection Agency water quality guidelines for recreational waters prevent gastrointestinal illness? A systematic review and meta-analysis”, *Environmental Health Perspectives*, 111(8), 1102.

Wamsley, T. V., Cialone, M. A., Smith, J. M., Atkinson, J. H., & Rosati, J. D. (2010). “The potential of wetlands in reducing storm surge”, *Ocean Engineering*, 37(1), 59-68.

Whitman, R. L., & Nevers, M. B. (2004). “Escherichia coli sampling reliability at a frequently closed Chicago beach: monitoring and management implications”, *Environmental science & technology*, 38(16), 4241-4246.

Xia, J., Falconer, R. A., & Lin, B. (2010). “Numerical model assessment of tidal stream energy resources in the Severn Estuary, UK”, *Proceedings of the Institution of Mechanical Engineers, Part A: Journal of Power and Energy*, 224(7), 969-983.

Zhang, K., Liu, H., Li, Y., Xu, H., Shen, J., Rhome, J., & Smith III, T. J. (2012). “The role of mangroves in attenuating storm surges”, *Estuarine, Coastal and Shelf Science*, 102, 11-23.